Site U1385[1]

Expedition 339 Scientists[2]

Chapter contents

[1]Expedition 339 Scientists, 2013. Site U1385. *In* Stow, D.A.V., Hernández-Molina, F.J., Alvarez Zarikian, C.A., and the Expedition 339 Scientists, *Proc. IODP,* 339: Tokyo (Integrated Ocean Drilling Program Management International, Inc.). doi:10.2204/iodp.proc.339.103.2013
[2]Expedition 339 Scientists' addresses.

Background and objectives

Future advances in our understanding of the Earth's climate system will rely on our ability to link high-resolution sedimentary archives from the oceans, ice cores, and terrestrial sequences and to interpret these records in the context of novel Earth system modeling approaches. Few places exist in the world where sufficiently detailed and unambiguous marine-ice-terrestrial linkages are possible. One challenge for the Integrated Ocean Drilling Program (IODP), and the broader drilling community in general, is to identify and recover marine, ice, and terrestrial sequences from appropriate locations and, with adequate temporal resolution, to study processes of the integrated climate system. Site U1385 on the West Iberian margin (Figs. F1, F2) represents such a location and provides a rare opportunity for recovering key sequences needed to link marine-ice-terrestrial archives.

The impetus for drilling this site comes from Nick Shackleton's pioneering work on Core MD95-2042 from the Iberian margin, which has played a pivotal role in our understanding of millennial-scale climate variability over the last glacial cycle. Shackleton et al. (2000) demonstrated that the oxygen isotopic record of the planktonic foraminifer *Globigerina bulloides* in Core MD95-2042 could be correlated precisely to $\delta^{18}O$ variation (i.e., temperature) in the Greenland Ice Core during the last glacial (Fig. F3). Transitions marking the onset and end of interstadials were abrupt, resembling a "square-wave" form, which suggests that the Polar Front migrated rapidly, leading to sudden changes in North Atlantic surface waters. By comparison, the $\delta^{18}O$ benthic curve resembled the temperature record from Antarctica, both in shape (the "triangular" form of Antarctic Isotope Maxima) and phasing relative to Greenland and North Atlantic surface temperature records. This Antarctic affinity largely reflects changes in local deepwater $\delta^{18}O_{dw}$, which may be due to changes in deepwater sourcing and/or source signature (Skinner et al., 2007). The strength of the Portuguese margin sediment record is the ability to correlate millennial-scale climate events from the marine environment to polar ice cores in both hemispheres. Moreover, the narrow continental shelf and proximity of the Tagus River result in rapid delivery of terrestrial material to the deep-sea environment off Portugal, thereby providing a record of vegetation changes and permitting correlation of marine and ice-core records to European terrestrial sequences (e.g., Shackleton et al., 2000, 2004; Sánchez Goñi et al.,

doi:10.2204/iodp.proc.339.103.2013

1999, 2002; Tzedakis et al., 2004, 2009; Roucoux et al., 2006; Margari et al., 2010). Few other, if any, places exist in the world ocean where such detailed and unambiguous marine-ice-terrestrial linkages are possible. For this reason, the Iberian margin has become a focal point for studies of climate variability over the last several glacial cycles. Extending this remarkable sediment archive further back in time is the primary goal of Site U1385.

Numerous CALYPSO piston cores have been retrieved and studied from the Iberian margin, and piecemeal sections extend as far back as marine isotope Stage (MIS) 15. From experience on cruises of the *Marion Dufresne* (MD03 and MD08), deeper penetration is limited using conventional piston coring systems because of the highly cohesive nannofossil oozes of MIS 9, 11, and 13. Thus, the drilling capability of the R/V *JOIDES Resolution* was needed for obtaining these continuous sections and extending the Iberian margin record to study the evolution of millennial-scale climate variability across successive glacial cycles and its role in glacial–interglacial climate transitions.

Site U1385 (37°34.285′N, 10°7.562′W) coincides with the position of Core MD01-2444, which has been studied extensively as part of the Pole-Ocean-Pole project (e.g., Fig. **F1**) (Skinner and Shackleton, 2006; Vautravers and Shackleton, 2006; Martrat et al., 2007; Margari et al., 2010). The water depth (2578 meters below sea level [mbsl]) places the site under the influence of Northeast Atlantic Deep Water today; however, it was influenced to a much greater degree by southern sourced waters during glacial periods (Curry and Oppo, 2005).

The overall objective of Site U1385 was to recover a late Pleistocene sediment record that will greatly improve the precision with which marine sediment records of climate change can be correlated to and compared with ice-core and terrestrial records. Specific objectives to be accomplished by postcruise research include

- Documenting the nature of millennial-scale climate variability for older glacial cycles of the Quaternary, including changes in surface and deepwater circulation during the "100 k.y. world," Mid-Pleistocene Transition (MPT), and "41 k.y. world";
- Deriving a marine sediment proxy record for the Greenland Ice Core beyond the oldest ice (~125 ka) to examine the amplitude and pacing of Dansgaard/Oeschger-type variability during previous ice ages;
- Determining interhemispheric phase relationships (leads/lags) by comparing the timing of proxy variables that monitor surface (Greenland) and deepwater (Antarctic) components of the climate system, thereby overcoming problems of age determination on millennial and submillennial timescales;
- Studying how changes in orbital forcing and glacial boundary conditions affect the character of suborbital-scale climate variability and, in turn, how millennial-scale variability interacts with orbital geometry to produce the observed glacial–interglacial patterns of climate change;
- Reconstructing the climate transitions into and out of glacial periods at high temporal resolution;
- Reconstructing the history of changing local dominance of northern-sourced versus southern-sourced deep water on orbital and suborbital timescales during the Quaternary;
- Investigating climate variability during past interglacial periods in comparison to the Holocene;
- Linking terrestrial, marine, and ice-core records by analyzing pollen and terrestrial biomarkers that are delivered to the deep-sea environment by rivers; and
- Developing an orbitally tuned timescale and contributing to the development of a global stratigraphy having sufficient resolution to study abrupt climatic events and their phase relationships.

Operations

Port call

Expedition 339 began with the first line ashore at 0830 h, 16 November 2011, to Berth 12 in Ponta Delgada harbor on the island of Saõ Miguel, Azores (Portugal). The IODP technical crew change occurred as scheduled on 17 November, although a group of IODP personnel arrived on 18 November because of weather-related travel problems. The scientific complement joined the vessel on 18 November. Education and public relation activities were carried out on Friday and Saturday, 18 and 19 November, and included tours of the *JOIDES Resolution* for 175 students and 15 teachers from 4 local high schools (Escola Secundária Antero de Quental-Ponta Delgada, Escola Secundária das Laranjeiras-Ponta Delgada, Escola Secundária de Lagoa-Lagoa, and Escola Secundária da Ribeira Grande-Ribeira Grande), 12 students and professors from the Universidade dos Açores, 25 students and researchers from the Centro de Vulcanologia e Avaliação de Riscos Geológicos, 20 local visitors, 9 local government representatives, the Portuguese European Consortium for Ocean Research Drilling delegate, and 6 local journalists (press).

In addition to routine resupply of consumables and offloading of returning freight, the ship was loaded with ~600 MT of marine gasoil, 60 ST of sepiolite, and 20 ST of barite drilling mud. Just prior to concluding the port call in Ponta Delgada, the home port of registry for the *JOIDES Resolution* was changed from Monrovia, Liberia, to Limassol, Cyprus. The port call concluded when the last line was released at 0800 h, 22 November.

Site U1385

We arrived at Site U1385 (proposed Site SHACK-04A) at 0400 h Universal Time Coordinated, 25 November 2011, after a 68 h, 741 nmi journey from Ponta Delgada. Five holes were cored at this site using the advanced piston corer (APC) and nonmagnetic core barrels (Table T1). Four holes were cored to ~150 meters below seafloor (mbsf) and one to just 9.5 mbsf (1 core). A total of 67 cores were required to obtain 621.8 m of sediment (103.2% recovery). The advanced piston corer temperature tool (APCT-3) was deployed 12 times.

Hole U1385A

The initial pipe trip included routine measuring and "rabbiting" that occurs on the first deployment of the drill string. Following a 3 h survey of the seabed using the underwater camera system, during which no obstructions were observed, Hole U1385A was spudded with the APC at 2300 h, 25 November. Recovery of the first core established the seafloor depth at 2598 meters below rig floor (mbrf) (2587 mbsl). Piston coring with nonmagnetic core barrels advanced to a total depth of 151.1 mbsf (17 cores), which was the depth objective of the site. Total recovery in Hole U1385A was 155.9 m (103%). Cores 339-U1385A-4H through 17H were oriented with the FlexIt tool. The APCT-3 was deployed to take temperature measurements at 30 (Core 4H), 58.5 (Core 7H), 87 (Core 10H), and 115.5 (Core 13H) mbsf. The APC experienced partial strokes on Cores 14H and 17H. The last core had advanced only 7.7 m when the formation became firm and abruptly stopped the APC. The drill crew experienced difficultly extracting the sinker bars from the drill string prior to pulling out of the hole, requiring 4.5 h of IODP rig time to remove a deformed section of coring line before operations could resume. This involved the removal of 100 m of coring line, reheading the line, and redressing the oil saver.

Hole U1385B

Following a vessel offset of 20 m east of Hole U1385A, operations in Hole U1385B began at 0030 h, 27 November. The water depth calculated from the recovery of the first core was 2598 mbrf (2587 mbsl). Piston coring using nonmagnetic core barrels continued to a total depth of 147.9 mbsf (16 cores). Total recovery in Hole U1385B was 150.7 m (103%). APCT-3 measurements were made at 34.6 (Core 4H), 63.1 (Core 7H), 91.6 (Core 10H), and 120.1 (Core 13H) mbsf.

Hole U1385C

After a vessel offset of 20 m south of Hole U1385B, Hole U1385C was spudded at 1830 h, 27 November. Because the core barrel was retrieved full of sediment (9.87 m), a mudline depth could not be determined, and another hole was required to obtain a good mudline core. Total recovery in Hole U1385C was 9.9 m (104%).

Hole U1385D

Following a vessel offset of 20 m south, Hole U1385D was spudded at 2045 h, 27 November. The first core established a seafloor depth at 2595 mbsf (2584 mbsl). Piston coring advanced without incident to a final depth of 146.4 mbsf (16 cores) with an average recovery of 105.2%. Cores were oriented starting with Core 4H. The APCT-3 was deployed at 35.4 (Core 4H), 60.9 (Core 7H), 89.4 (Core 10H), and 117.9 (Core 13H) mbsf. Cores 15H and 16H were partial strokes and advanced by recovery. All cores were obtained with nonmagnetic core barrels. The bit cleared the seafloor at 1255 h, 28 November.

Hole U1385E

After a vessel offset of 20 m west of Hole U1385D, piston coring in the last hole at Site U1385 began at 1520 h, 28 November, using nonmagnetic core barrels. Seventeen cores were taken to the total depth of 148.7 mbsf by 0730 h, 29 November. We recovered 151.3 m of sediment (102%). Cores were oriented starting with Core 5H. The last three cores (Cores 15H through 17H) were partial strokes and advanced by recovery. Two cores were intentionally repositioned (Core 8H and 10H) to maintain a stratigraphic depth offset relative to the previous holes on this site. All cores were obtained with nonmagnetic core barrels. This hole concluded coring operations at this site.

The drill string was recovered and the bit cleared the seafloor at 0850 h, 29 November. Once the drilling equipment was secured and the beacon recovered, the vessel departed for the next site at 1515 h. Total time on site was 4.5 days.

Lithostratigraphy

The shipboard lithostratigraphic program at Site U1385 involved detailed visual logging of all archive

sections for grain size, sediment color, sedimentary structures, and bioturbation intensity to describe the facies and facies associations. Sediments from Hole U1385A were sampled extensively for smear slides for petrographic analysis during visual core description. Relatively few smear slides were made from Holes U1385B–U1385E, and those were from lithologies and features of particular interest or different from Hole U1385A. Sixteen samples were selected from Holes U1385A and U1385B for X-ray diffraction (XRD) analyses of powdered bulk samples in order to gain a general indication of bulk mineralogy.

Shipboard geochemical analyses of total carbonate contents from these cores range from 23 to 39 wt% in Hole U1385B (Fig. **F4;** Table **T2**) with carbonate values as high as 46 wt% reported from Hole U1385A. As is typical when comparing smear slide–based compositional estimates with direct geochemical measurements, these geochemical results indicate somewhat lower carbonate contents than were estimated from examining smear slides. Smear slide data typically overestimate the biogenic fraction compared with the fine-grained terrigenous fraction (i.e., detrital clay and silt), and for Site U1385 we found the smear slide estimates of carbonate content to be overestimated by a factor of 2. As a result, the geochemical results have been used to recalibrate our smear slide–based estimates of sediment carbonate content, and the lithologies determined for these sediments have been revised to reflect their decreased carbonate contents. The lithologic names used in this report and on the accompanying summary diagrams, except for the summary of component abundances based on smear slides (Fig. **F5**), have therefore been adjusted according to the conversion scheme shown in Table **T3.** It is important to note, however, that the individual core summaries and the database entries for Site U1385 still contain the lithologic names applied during shipboard visual core description (i.e., those based on the original smear slide estimates of carbonate content).

The sediments at Site U1385 are defined as a single lithologic unit. Unit I is composed of a Holocene–Pleistocene sequence dominated by bioturbated nannofossil muds and nannofossil clays (both "marls" sensu Stow, 2005), which vary in the relative proportion of biogenic carbonate material (Fig. **F6;** Table **T4**). This variation in composition is evident in the visual color estimation, from lighter (more carbonate) to darker (less carbonate), which typically defines a marked color cyclicity. Relatively more terrigenous-dominated sediments are present in the upper quarter of Unit I, but their occurrence does not warrant the definition of any additional lithologic units or subunits.

The character of sediment physical properties, including natural gamma radiation (NGR), magnetic susceptibility, and density, as well as sediment color spectra data, also record the distribution of this color/composition cyclicity (see **"Physical properties"**). Characteristics of the sedimentary sequence cored at Site U1385, together with some of these additional properties, are summarized in Figure **F7.**

Unit I description

Intervals: 339-U1385A-1H-1, 0 cm, through 17H-CC, 26 cm; 339-U1385B-1H-1, 0 cm, though 16H-6, 110 cm; 339-U1385C-1H-1, 0 cm, through 1H-CC, 70 cm; 339-U1385D-1H-1, 0 cm, through 16H-CC, 34 cm; 339-U1385E-1H-1, 0 cm, through 17H-CC, 28 cm

Depths: Hole U1385A = 0–151.63 mbsf (bottom of hole [BOH]), Hole U1385B = 0–146.30 mbsf (BOH), Hole U1385C = 0–9.92 mbsf (BOH), Hole U1385D = 0–147.02 mbsf (BOH), Hole U1385E = 0–147.26 mbsf (BOH)

Age: Holocene to Pleistocene

Lithologies and bedding

The major lithologies in Unit I are very uniform, falling entirely within the nannofossil mud and nannofossil clay classifications (Fig. **F6;** Table **T4**). The muds have a slightly greater proportion of silt-sized fraction than the clays. Significant differences exist, however, in carbonate content within this group (23–39 wt%), which yields distinctive color cyclicity. We therefore informally refer to dark and light nannofossil muds and clays in order to emphasize this distinction.

Minor lithologies include those that are more biogenic rich, muddy nannofossil ooze and nannofossil silt, and those that are more terrigenous rich, mud with biogenic grains, sandy silt with nannofossils, and mud with nannofossils. The more terrigenous rich lithologies are only recognized in the upper 25% of lithologic Unit I (specifically in smear slides from Cores 339-U1385A-3H and 4H; Fig. **F5;** Table **T4**).

Bedding is very indistinct and nonexistent in parts. The major lithologies are interstratified at the meter scale (typically 1–2 m) of dark- and light-colored sediment, whereas minor lithologies are interstratified at scales ranging from ~1 cm to ~1 m. The contacts between all lithologies are bioturbated and gradational.

Structure and texture

No primary sedimentary structures were observed. Bioturbation is the most obvious secondary sedimentary structure and is present throughout Unit I.

The most common indicators are diffuse centimeter-scale mottling and millimeter-scale pyritic burrow fills. Black iron sulfide mottling is also common. Discrete burrows, including *Zoophycos, Chondrites,* and *Planolites,* and macroscopic pyritized burrows (Fig. F8) are also common. The bioturbation index ranges from slight to moderate.

Small-scale subvertical microfaults (Fig. F9) and contorted beds are present at several depth intervals that are relatively consistent in two or more holes, recording syn- or postdepositional instability of the sediment column. The distribution of these features is summarized in Table T5, including features at ~39–44 meters composite depth (mcd) in Holes U1385B and U1385D, at ~66–74 mcd in Holes U1385B and U1385D, and at ~105–110 mcd in Holes U1385A, U1385B, and U1385E. One additional zone containing features that may be contorted strata is at ~34 mcd in Holes U1385A, U1385B, and U1385D. The sediment grain size is fine throughout, mostly clay and silty clay (mud). Although subtle textural variation is observed, from more clay rich to more silt rich, it is not yet clear how this varies with respect to composition, color, or other changes.

Composition

The principal components of all lithologies are biogenic and terrigenous. The biogenic fraction is dominated by nannofossils with rare to common foraminifers and rare pteropods, ostracods, diatoms, and sponge spicules. Terrigenous components are dominated by a clay and fine silt–sized fraction, which is indeterminate in smear slides, and by detrital carbonate of indeterminate nature. There are also minor amounts of quartz, mica, volcanic glass, dolomite (both detrital and authigenic), and an opaque mineral fraction. It was recognized later in Expedition 339 that it was difficult to distinguish between volcanic glass and biotite in smear slides, so some of the material identified in this site as volcanic glass may in fact be biotite.

The abundances of terrigenous components, as estimated from smear slides (Fig. F5), are 0%– 86% siliciclastics (including quartz, feldspars, accessory minerals, and clay minerals), 0%–35% detrital carbonate, and 0%–11% volcanic glass or biotite. No discrete ash layers and no dropstones were observed. The abundances of biogenic components are 7%–91% biogenic carbonate (primarily nannofossils) and 0%–6% biogenic silica (primarily diatom and sponge fragments). Because the geochemically measured total carbonate content only ranges from 23 to 39 wt% in these cores (see Fig. F4; Table T2), the smear slide values given should be treated as relative rather than absolute. Pyrite (usually associated with burrows) is present throughout the cored interval, constituting the most abundant and widespread authigenic sediment component observed. Pyrite, or more likely a precursor black iron sulfide, is present as millimeter-scale disseminated burrow fills and as discrete millimeter- to centimeter-scale burrow fills and nodules (Fig. F8). Authigenic dolomite, recognized as characteristically well-defined rhombic crystals, is present at low abundances in a limited number of smear slides.

Macrofossils are very poorly represented at Site U1385. A single whole specimen of cold-water coral was found in interval 339-U1385B-4H-2, 80–82 cm (Fig. F10). Other macrofossils include shell fragments, including bivalves and gastropods.

Color

The principal colors of lithologies, as noted during visual description of the upper part of Unit I, range from light gray (N 7/ and 5Y 7/1) to gray (5Y 6/1) for the more biogenic rich, light nannofossil muds and clays. Lithologies that are more terrigenous rich, the dark nannofossil muds and clays, typically range from gray (5Y 5/1) to greenish gray (10Y 5/1). In the lower half of Unit I, all lithologies tend toward darker colors, including greenish gray (10Y 5/1, 5GY 5/1, and 5G 5/1) and dark greenish gray (10Y 4/1 and 5GY 4/1), so the light-to-dark color cyclicity is more muted.

Bulk mineralogy

XRD analyses were performed on 16 powdered bulk samples from Holes U1385A and U1385B to gain a general indication of the bulk mineralogy and to identify any trends with age or with depth in the sediment. The resulting scans are shown in Figure F11, and the mineral intensities are listed in Table T6. In general, the mineralogy is quite uniform downhole, although there are some variations in relative peak intensities, especially illite, that may indicate changes in mineral content. The primary minerals identified include quartz, calcite, dolomite, K-feldspar, plagioclase, and the clay minerals chlorite, illite, and kaolinite. Quartz and calcite are the dominant peaks, with quartz generally the larger. In two samples (from 41 and 52 mbsf), however, the calcite peak is nearly twice as large as the quartz peak. The dolomite peak at ~29.45°2θ is a relatively large peak, although this is probably due to its high crystallinity rather than to its relative abundance. The two feldspar peaks are present throughout the cored sediments and indicate that these minerals make up a minor component of the mineral grains. The clays chlorite, illite, and kaolinite are present in all samples, and the presence of kaolinite was confirmed by

heating. The chlorite peak is somewhat smaller than the kaolinite and illite peaks.

Whereas the diffraction patterns are remarkably uniform, there appears to be some variation in the patterns from different samples in the region from about 5° to 8°2θ (Fig. F12), where the baseline intensity appears to change from sample to sample, although the peaks at 6.25° and 8.78°2θ remain fairly constant. The changing baseline intensity levels in this interval may indicate the presence of poorly crystalline mixed-layer clay minerals in the sediment. An attempt was made to quantify the amount of this poorly crystalline material by measuring the intensity of the pattern at an angle of 7°2θ, with the assumption that the higher background levels indicate a larger percentage of this clay material in the sediments. Figure F13 shows that this intensity generally increases with depth in the sediment. In order to explore the clay mineral composition in more detail, each pressed-powder sample was glycolated and rescanned. For each sample, the diffraction intensity at 7.65°2θ after glycolation was less than the diffraction intensity at that position without glycolation and there was often a broad peak at about 5°2θ, indicating that the glycolation of expandable (smectitic) interlayers had caused peak shifts to lower 2θ values (Fig. F14). The magnitude of the intensity decrease at 7.65°2θ following glycolation was also used to indicate the relative abundance of smectitic and/or interlayered clays downcore at this site (Fig. F15). Although sample-to-sample variability is high, the general trend shows that the intensity decrease increases downcore, which supports the interpretation of higher abundances of smectites and/or smectite-bearing mixed-layer clays at depth.

Discussion

The entire section cored at Site U1385 is very typical of a hemipelagic continental margin succession deposited under normal marine conditions with a fully oxygenated water column. Sedimentation rates (average = 10 cm/k.y.), as reported in "Biostratigraphy," are quite normal for such an environment. The dominant lithologies are calcareous muds and clays (also known as marls), with variation in biogenic content clearly evident as color variation from lighter (more calcareous) to darker (more terrigenous). These lithologic variations are expressed clearly in the NGR, magnetic susceptibility, and density records (see "Physical properties"), as well as in the automated color spectral data. In particular, changes in reflectance (L*) appear to correlate well with changes in the relative abundance of detrital and biogenic sediment components.

Following the accepted definition of hemipelagite as fine-grained sediment with the silt-size component >40% of the terrigenous fraction and typically with a mixed biogenic-terrigenous composition (Stow and Tabrez, 1998), we would confirm the succession at Site U1385 as hemipelagic. It was deposited slowly and continuously by a combination of vertical (pelagic) settling and slow lateral advection across the continental margin. The sediment shows only very slight postdepositional disturbance caused by slope instability, as evidenced by localized minor faulting and slumping, commensurate with its deposition on a broad knoll between relatively large channels. The sediment also shows continuous bioturbation throughout, which will have caused a certain degree of vertical mixing. Common *Zoophycos* ichnofossils attest to potential sediment mixing of >10–20 cm vertically.

Other observations to highlight with regard to the planned postexpedition study of this site as a marine reference section for Quaternary climate variation would be

- The relative importance of detrital carbonate throughout Unit I. What is its potential source? What are the implications for transport via wind or streams and currents?
- The apparent increase in detrital component at ~100–300 ka (age estimate based on sedimentation rate of ~10 cm/k.y. and depths of Cores 339-U1385A-3H and 4H). What might be the paleoclimatic significance?

Biostratigraphy

A continuous record of calcareous nannofossil ooze (see "Lithostratigraphy") was recovered at Site U1385, spanning from the early Pleistocene to the Holocene (Table T7). Samples from all core catchers of Holes U1385A–U1385D and the five lowermost core catchers of Hole U1385E were prepared for analysis. Sample 339-U1385C-1H-CC was not analyzed.

Nannofossils and planktonic foraminifers were very abundant and relatively well preserved in all samples (Tables T8, T9). For planktonic foraminifers, evidence of some fragmentation was recognized in most of the samples. Benthic foraminifers were also relatively abundant and diverse in the samples (Table T10), although their percentage with respect to planktonic foraminifers is usually <5%. By contrast, ostracods were rare in most of the samples. Their percentage with respect to planktonic foraminifers is <1%. Pteropods were not observed in any of the samples from this site but were observed in mudline

samples collected from each hole (top of Core 1H). Pollen and spores are generally abundant and moderately well preserved. Concentrations ranging between 1,800 and 12,000 grains/cm^3 are similar to those reported previously from the Western Iberian margin (Sánchez Goñi et al., 1999, 2009). Microcharcoal particles occur abundantly.

The chronologic framework for Site U1385 is based on the identification of a series of calcareous nannofossil and planktonic foraminifer events as well as one benthic foraminifer datum (Table T7). The distribution of calcareous nannofossil events suggests a continuous Pleistocene record at Site U1385. The calibrated biohorizons allow us to estimate a nearly uniform sedimentation rate of ~10 cm/k.y. (Fig. F16).

Calcareous nannofossils

All core catcher samples from Holes U1385A, U1385B, and U1385D were examined for calcareous nannofossil biostratigraphy. Additionally, selected samples from Hole U1385A were analyzed in order to constrain biohorizons, paying attention only to marker species. Calcareous nannofossil assemblages are abundant and diverse, and preservation is good, with weak dissolution in some samples. Small placolith species (<3 µm) dominate most of the assemblages. Inorganic input and reworking of pre-Pleistocene (mainly Neogene) species vary from few to common throughout all samples (Table T8).

In total, seven Pleistocene nannofossil datums defined and/or calibrated by Raffi et al. (2006 and references therein) and Flores et al. (2010) were identified in all Site U1385 holes (Table T7).

The change in abundance of the large *Emiliania huxleyi* (>4 µm) that characterizes Termination 1 in mid- to low-latitude water masses in the Atlantic Ocean has been recognized as a useful event by Flores et al. (2010). This change in abundance was recorded between Samples 339-U1385A-2H-1, 90 cm, and 2H-2, 7 cm (2.40–3.07 mbsf); between the top of the hole and Sample 339-U1385B-1H-CC (0–6.99 mbsf); and between the top of the hole and Sample 339-U1385D-1H-CC (top of the hole to 6.99 mbsf), making it possible to distinguish the onset of the Holocene in all three holes.

The first occurrence (FO) of *E. huxleyi* (0.26 Ma), which marks the base of Zone NN21, is ubiquitously present between Samples 339-U1385A-4H-4, 90 cm, and 4H-5, 5 cm (25.90–26.55 mbsf); between 339-U1385B-3H-CC and 4H-CC (25.44–35.12); and between 339-U1385D-3H-CC and 4H-CC (26.28–36.04 mbsf).

The last occurrence (LO) of *Pseudoemiliania lacunosa* (0.46 Ma), considered a globally synchronous event that defines the top of Zone NN19, occurs between Samples 339-U1385A-6H-CC and 7H-1, 40 cm (49.40–49.48 mbsf); 339-U1385B-6H-CC and 7H-CC (53.85–63-65 mbsf); and 339-U1385D-6H-CC and 7H-CC (51.92–61.42 mbsf).

A biohorizon considered useful in Pleistocene sediments is the LO of *Reticulofenestra asanoi* (0.90 Ma). This event was identified between Samples 339-U1385A-11H-6, 90 cm, and 11H-7, 5 cm (95.40–96.05 mbsf); 339-U1385B-10H-CC and 11H-CC (92.07–101.74 mbsf); and 339-U1385D-10H-CC and 11H-CC (89.87–99.29 mbsf). The FO of *R. asanoi* (1.07 Ma), another significant event for the Pleistocene, was identified between Samples 339-U1385A-13H-7, 50 cm; and 13H-CC (115.70–116.32); 339-U1385B-12H-CC and 13H-CC (110.19–120.57 mbsf); and 339-U1385D-13H-CC and 14H-CC (118.76–127.80). To define these biohorizons, specimens of *R. asanoi* ≥6 µm in size were considered.

The LO of large *Gephyrocapsa* spp. (>5.5 µm; 1.24 Ma) was recorded between Samples 339-U1385A-15H-4, 8 cm, and 15H-4, 105 cm (128.99–129.96 mbsf); 339-U1385B-13H-CC and 14H-CC (120.57–129.90 mbsf); and 339-U1385D-14H-CC and 15H-CC (127.80–137.09 mbsf).

The LO of *Helicosphaera sellii* (1.25 Ma) is considered a diachronous event (Raffi et al., 1993; Wei, 1993). Its occurrence at this site is consistent with the ages provided by Raffi et al. (2006) for the Mediterranean Sea. At Site U1385, the event is placed between Samples 339-U1385A-15H-5, 90 cm, and 15H-6, 5 cm (131.31–131.96 mbsf); 339-U1385B-13H-CC and 14H-CC (120.57–129.90 mbsf); and 339-U1385D-14H-CC and 15H-CC (127.80–137.09 mbsf).

Planktonic foraminifers

Both the 150 and 63 µm residues are clearly dominated by planktonic foraminifers, with very small proportions of fine-grained detrital grains in some samples, such as Sample 339-U1385B-1H-CC. The planktonic foraminifer assemblages observed at Site U1385 are typical of temperate waters from the North Atlantic with temporal increases in abundance of subtropical or polar to subpolar species (Table T9). *Neogloboquadrina pachyderma* (dextral), *Globorotalia inflata,* and *Globigerina bulloides* are the dominant species in most of the samples, although *N. pachyderma* (sinistral) during glacial times and *Globigerinoides ruber* during interglacials are also temporarily abundant. *Orbulina universa* and *Globigerinella siphonifera* are present in nearly all core catcher samples. Deep-dwelling species *Globorotalia truncatulinoides* and *Globorotalia scitula* are also present in most core catcher samples, with both species preferentially coiling dextral. *Globorotalia crassaformis,*

when present, coils in either direction. *Globorotalia hirsuta* occurs only sporadically.

Two planktonic foraminifer bioevents were identified at Site U1385, the top and bottom of the paracme of *N. pachyderma* (sinistral) (Table **T7**). The top of the paracme is astronomically dated at 1.21 Ma and tuned to insolation Cycle i117 in the Mediterranean (Lourens et al., 1996a, 1996b) and has been reported in the northeast Atlantic (Raymo et al., 1989; Lourens et al., 1998; Sierro et al., 2009) near the bottom of the Cobb Mountain paleomagnetic subchron during MIS 36 (Sierro et al., 2009). This event was located in all holes between Samples 13H-CC and 14H-CC (116.12–124.67 mbsf in Hole U1385A, 120.57–129.90 mbsf in Hole U1385B, 118.76–127.80 mbsf in Hole U1385D, and 111.43–119.13 mbsf in Hole U1385E), although its location in Hole U1385D is ambiguous because of the rare presence of this species in Sample 339-U1385D-13H-CC.

The bottom paracme of *N. pachyderma* (sinistral) was only recorded in Holes U1385D and U1385E, where the species is relatively abundant after an interval of very rare occurrence above this level. Consequently, this bioevent must be placed between Samples 339-U1385D-15H-CC and 16H-CC (137.09–147.00 mbsf) and between 339-U1385E-16H-CC and 17H-CC (138.59–147.20 mbsf). The bioevent is astronomically dated in the Mediterranean at 1.37 Ma within insolation Cycle i131 (Lourens et al., 1996a). *N. pachyderma* (sinistral), which is abundant during glacial periods older than 1.37 Ma, almost disappears in the glacial stages of MIS 42, 40, and 38, as has been reported from the Vrica-Crotone composite section in Italy (Lourens et al., 1996b) and Deep Sea Drilling Project Site 607/ IODP Site U1313 from the same location in the North Atlantic (Raymo et al. 1989; Sierro et al., 2009). This event was also observed at Ocean Drilling Program Site 967 and Hole 969D (Lourens et al., 1998). However, the low sampling resolution and the frequent changes in abundance of this species linked to glacial–interglacial fluctuations prevented identification of a more accurate position of these two events.

Because the bottom paracme of *N. pachyderma* (sinistral) is located at the bottom of Holes U1385D and U1385E, it was concluded that Site U1385 extends from the Holocene to 1.37 Ma.

In Samples 339-U1385A-16H-CC and 17H-CC (143.80–151.63 mbsf), 339-U1385B-15H-CC and 16H-CC (137.76–146.30 mbsf), 339-U1385D-15H-CC and 16H-CC (137.09–147.00 mbsf), and 339-U1385E-16H-CC and 17H-CC (138.59–147.20 mbsf), large, heavily encrusted specimens of *Neogloboquadrina atlantica* (dextral) are present (Table **T9**). An incursion of this species during the early Pleistocene was reported for the North Atlantic at IODP Site U1313 (Channell, Kanamatsu, Sato, Stein, Alvarez Zarikian, Malone, and the Expedition 303/306 Scientists, 2006). At that site, the top of the incursion was dated at ~1.4 Ma, based on a low-resolution biostratigraphy study. With a more accurate chronology, this event may be useful for Atlantic and Mediterranean correlations.

Benthic foraminifers

All core catcher samples from Hole U1385A were studied for the abundance of benthic foraminifers (Table **T10**). Additionally, selected core catcher samples from Holes U1385B and U1385D were evaluated for the "*Stilostomella* extinction" event. The revealed benthic assemblages are well preserved, with only a few specimens broken in each sample.

Assemblages from the lower portion of Hole U1385A are characterized by high abundances of stilostomellids, in particular *Siphonodosaria lepidula* and *Myllostomella fijiensis*. Together with the occurrences of *Dentalina* spp., *Epistominella exigua, Fursenkoina complanata, Sphaeroidina bulloides,* and *Uvigerina peregrina,* the assemblages suggest high flux of organic carbon to the seafloor and a poorly oxygenated environment (Kaiho, 1999; Kawagata et al., 2005; Murray, 2006).

Stilostomellids markedly decrease in abundance from Sample 339-U1385A-12H-CC to 10H-CC, until they finally disappear between Samples 10H-CC and 9H-CC (77.83–82.12 mbsf), marking the *Stilostomella* extinction (0.70–0.58 Ma) (Hayward, 2002; Kawagata et al., 2005). The datum is identified at similar depth intervals in Holes U1385B (72.68–82.12 mbsf) and U1385D (80.37–89.87 mbsf) and agrees well with the age between 0.90 and 0.46 Ma, as suggested by nannoplankton assemblages for the respective samples (Table **T7;** Fig. **F16**). Higher abundances of *Cibicidoides* spp. and *Pyrgo* spp. indicate higher bottom water oxygenation (Kaiho, 1999; Murray, 2006).

Subsequent assemblages from Samples 339-U1385A-9H-CC to 6H-CC constantly show high abundances of *E. exigua* and *Cassidulina laevigata/teretis*. Together with the regular occurrences of epifaunal (*Cibicidoides* spp.) and deep infaunal (*Melonis* spp., *Globobulimina affinis,* and *Globocassidulina subglobosa*) taxa, these assemblages indicate increased seasonality with pulses of high organic carbon flux and fluctuating bottom water oxygenation (Schnitker, 1984; Gooday, 1993; Kaiho, 1999; Gupta and Thomas, 2003; Bartoli et al., 2005).

In the uppermost portion of Hole U1385A (0–39.97 mbsf), the composition of the foraminiferal assemblages differs strongly between samples. In general,

the assemblages show increased abundances of buliminid and bolivinid species with highly varying background fauna. Samples 339-U1385A-5H-CC to 3H-CC are mainly composed of hyaline species, whereas abundant occurrences of *Rhizammina* spp. (Sample 2H-CC) and spiroloculinid foraminifers (Sample 1H-CC) are documented for the top of the section. These assemblages indicate high organic carbon flux and poorly oxygenated bottom water (Kaiho, 1999; Murray, 2006).

In conclusion, the succession of benthic foraminiferal assemblages documents a deep-sea environment affected by considerable changes in surface water productivity, organic carbon flux, and ventilation of bottom water. The observed variability in benthic associations most likely reflects the impact of the Mid-Pleistocene Transition (MPT) on North Atlantic circulation patterns in general (Kawagata et al., 2005), as well as changes in regional upwelling intensity during glacial and interglacial periods.

Ostracods

Ostracods were studied from all core catcher samples in Holes U1385A and U1385B (Table **T11**), in which they occur in low numbers (from barren to 20 valves per sample) when compared to other North Atlantic sites at similar water depths (Cronin et al., 1999; Didié et al., 2000; Alvarez Zarikian et al., 2009). Preservation ranges from excellent to poor, and highest abundances (>10 valves per sample) are observed in the upper 45 m of the sedimentary record at Site U1385 (Samples 339-U1385B-1H-CC, 3H-CC, 4H-CC, and 5H-CC; 339-U1385A-11H-CC; and 339-U1385B-10H-CC, 14H-CC, and 16H-CC). Barren samples were observed between ~80 and 115 mbsf in Holes U1385A and U1385B, an interval dated to ~0.6–1.1 Ma or equivalent to the MPT (Fig. **F16**). More than 21 species belonging to 16 genera were identified overall. Samples with the highest abundance are dominated by *Krithe* spp. In the Atlantic Ocean, the deep-sea taxon *Krithe* is dominant in North Atlantic Deep Water (NADW) (Cronin et al., 1999; Didié and Bauch, 2000; Dingle and Lord, 1990; Yasuhara et al., 2009a, 2009b). Therefore, the high relative abundance of *Krithe* at Site U1385 can be attributed to the influence of NADW. Other taxa found at Site U1385 include *Henryhowella asperrima* and *Cytheropteron* spp., followed by *Argilloecia acuminata, Australoecia posteroacuta, Poseidonamicus major, Cytherella robusta,* and *Echinocythereis echinata,* all taxa with worldwide distribution and common in deep-sea Cenozoic sediments. *Henryhowella* has been recorded with highest relative abundances during interglacials at other North Atlantic sites (Cronin et al., 1999; Didié and Bauch, 2000; Alvarez Zarikian et al., 2009). *Poseidonamicus* is a characteristic genus of lower NADW (Dingle and Lord, 1990) and occurs in very low abundance in Samples 339-U1385A-3H-CC and 339-U1385B-3H-CC. *Cytheropteron* is typically associated with deglacial periods in North Atlantic deep-sea sediments (Cronin et al., 1999; Alvarez Zarikian et al., 2009), but its low overall abundance and sparse sampling intervals do not allow for any paleoceanographic interpretations at this time.

Palynology

Nine unevenly distributed samples were analyzed from Hole U1385A (Table **T12**). Preservation ranges from moderate to good except for the lowest level (Sample 339-U1385A-16H-CC), which shows strong alteration of palynomorphs and, in particular, corroded Conifers. *Pinus* is abundant, with concentrations >2000 grains/cm^3 in almost all samples, excluding Samples 339-U1385A-3H-CC and 6H-CC (Fig. **F17**). Pollen assemblages are mainly composed of *Pinus* and trees and shrubs characterizing the Mediterranean forest (deciduous and evergreen *Quercus, Olea,* and *Phillyrea*), Ericaceae, grasslands (*Taraxacum*-type and Poaceae), and semidesert plants (*Artemisia, Chenopodiaceae, Ephedra dystachia,* and *Ephedra fragilis*). These assemblages are those typically found in southwestern Iberia over the last 425 k.y. (Sánchez Goñi et al., 1999, 2008, 2009; Tzedakis et al., 2009; Margari et al., 2010). Several experimental studies on the relationships between pollen content in marine sediments and vegetation of the adjacent continent (e.g., Heusser, 1985; Turon, 1984) and, in particular, experiments performed along the Iberian margin (Naughton et al., 2007) have shown that pollen assemblages from the Iberian margin reliably resemble the integrated (regional/subcontinental) vegetation occupying the adjacent landmass. Three samples (339-U1385A-6H-CC, 10H-CC, and 13H-CC) clearly reveal the dominance of open vegetation, semidesert, and grasslands in this region. From the uppermost sample (339-U1385A-1H-CC), the occurrence of a Mediterranean forest in southwestern Iberia was inferred that was assigned to the Holocene on the basis of previous studies (Lézine and Denèfle, 1997). The remaining samples are a mixture of both open vegetation and forest environments. Also, Sample 339-U1385A-11H-CC is characterized by high numbers of *Stelladinium* cf. *reidii,* a species of dinocyst living in warm waters (L. Londeix, pers. comm., 2011).

Paleomagnetism

Paleomagnetic investigation of the 67 cores collected at Site U1385 included the measurement of magnetic

susceptibility of whole-round and archive-half split-core sections and the natural remanent magnetization (NRM) of archive-half split-core sections. NRM was measured before and after alternating field (AF) demagnetization with peak fields of 10 and 20 mT for archive-half sections from Holes U1385A, U1385B, and U1385C. For archive-half sections from Holes U1385D and U1385E, NRM was measured before and after AF demagnetization with 20 mT peak field. Data from the FlexIt tool were used to orient cores from all holes except Hole U1385C, from which only one core was retrieved. FlexIt tool data were collected starting with Core 4H in Holes U1385A, U1385B, and U1385D and with Core 5H in Hole U1385E (Table **T13**). Stepwise AF demagnetization on 16 selected discrete samples from Hole U1385A was performed at successive peak fields of 0, 5, 10, 15, 20, 25, 30, 35, 40, 45, 50, 55, 60, 70, and 80 mT to verify the reliability of the split-core measurements. The depth levels from which the measured discrete samples were taken in Hole U1385A are indicated by triangles in the first panel of Figure **F18.** We processed data extracted from the Laboratory Information Management System (LIMS) database by removing all measurements collected from disturbed and void intervals, which are listed in Table **T14** (see **"Stratigraphic correlation"**), and all measurements that were made within 10 cm of the section ends, which are slightly biased by measurement edge effects. The processed NRM inclination, declination, and intensity data after 20 mT peak field AF demagnetization are listed in Tables **T15, T16, T17, T18,** and **T19.**

Natural remanent magnetization and magnetic susceptibility

The intensity of NRM after 20 mT peak field AF demagnetization in all five holes is similar in magnitude, ranging from ~10^{-5} to ~10^{-2} A/m (Fig. **F19**). For core sections from the uppermost ~50 mbsf, NRM intensity is on the order of ~10^{-2} A/m. Between ~50 mbsf and the bottom of the holes, NRM intensity decreases to ~10^{-3} to ~10^{-5} A/m. The general agreement of the trend between the NRM intensity and magnetic susceptibility suggests that the magnetic minerals that carry the NRM are the same that dominate the magnetic susceptibility.

In spite of the overall low intensities of NRM below ~50 mbsf, a relatively stable magnetic component was preserved in sediment from all five holes, which allows for the determination of magnetic polarity. A magnetic overprint with steep positive inclinations, which was probably acquired during drilling, was usually removed by up to 20 mT peak field AF demagnetization (Fig. **F19**). However, NRM directions show relatively large scatter below ~50 mbsf. This suggests that secondary magnetizations still remain and are probably a viscous remanent magnetization and/or chemical remanent magnetization caused by diagenetic growth or dissolution of magnetic minerals.

We calculated component NRM directions of the discrete samples from the data from the 25–50 mT demagnetization steps using principal component analysis (PCA; Kirschvink, 1980) and UPmag software (Xuan and Channell, 2009). Three discrete samples from the uppermost 90 mbsf yielded reasonably good component directions, with maximum angular deviation of <15°. Component inclinations of these discrete samples are generally consistent with the archive-half section measurements (yellow circles in the first panel of Fig. **F18**). The demagnetization behavior of two discrete samples that yielded good PCA results from above 50 mbsf and of two samples from below 50 mbsf with poor demagnetization behavior is illustrated in Figure **F19.** The two discrete samples from above 50 mbsf display a soft magnetic overprint that was removed at 15–20 mT AF demagnetization, demonstrating that this magnetic cleaning level is sufficient to eliminate the overprint.

Magnetic susceptibility measurements were made on whole cores from all five holes as part of the Whole-Round Multisensor Logger (WRMSL) analysis and on archive-half split-core sections using the Section Half Multisensor Logger (SHMSL) (see **"Physical properties"**). Magnetic susceptibility is consistent between the two instruments and, in general, mimics the NRM intensity. The WRMSL-acquired susceptibility was stored in the database in raw meter units. These were multiplied by a factor of 0.68 × 10^{-5} to convert to the dimensionless volume SI unit (Blum, 1997). A factor of (67/80) × 10^{-5} was multiplied by the SHMSL-acquired susceptibility stored in the database. Magnetic susceptibility varies between 10 × 10^{-5} and 50 × 10^{-5} SI (Fig. **F18**). Note that a constant of 25 × 10^{-5} SI was added to the SHMSL measurements (gray lines) to facilitate the comparison with the WRMSL measurements (black lines).

Magnetostratigraphy

Both magnetic declination and inclination were used when possible for the magnetostratigraphic interpretation at this site. The geomagnetic field at the latitude of Site U1385 (37.57°N) has an expected inclination of 56.98°, assuming a geocentric axial dipole field model, which is sufficiently steep to determine magnetic polarity in APC cores that lack horizontal orientation.

The Brunhes–Matuyama polarity transition occurs at ~93.8 mbsf in Hole U1385A (interval 339-U1385A-11H-5, ~80 cm), ~91.8 mbsf in Hole U1385B, ~97.3 mbsf in Hole U1385D, and ~92 mbsf in Hole U1385E (Fig. F18; Table T20). The polarity transition should occur over an interval of <1 m, assuming a sedimentation rate of ~100 m/m.y. and a polarity transition with <10 k.y. duration. However, the relatively large scatter of the NRM directions made it difficult to determine the exact position of the boundary. The top and bottom of the Jaramillo Subchron (C1r.1n) occur, respectively, at ~106.8 and ~117.7 mbsf in Hole U1385A (intervals 339-U1385A-13H-1, ~80 cm, and 14H-2, ~68 cm), ~101.2 and ~113.4 mbsf in Hole U1385B, ~107.3 and ~116.3 mbsf in Hole U1385D, and ~101.5 and ~111.2 mbsf in Hole U1385E (Fig. F18; Table T20). We interpret the short normal polarity interval at ~131–132.4 mbsf in Hole U1385A, ~129–132.1 mbsf in Hole U1385B, ~127.4–130.3 mbsf in Hole U1385D, and ~130.8–132.3 mbsf in Hole U1385E (Fig. F18; Table T20) as the Cobb Mountain Subchron (C1r.2n), although the large scatter of the NRM directions makes this interpretation somewhat tentative. In spite of relatively high sedimentation rates of ~100 m/m.y., we obtained no evidence for short-duration polarity flips and/or excursions, such as the Blake event, in the Brunhes Chron.

Physical properties

The shipboard physical properties program at Site U1385 included high-resolution nondestructive measurements of gamma ray attenuation (GRA) bulk density, magnetic susceptibility (loop sensor), *P*-wave velocity, and natural gamma radiation (NGR) on whole-round core sections. Thermal conductivity was obtained on Section 3 of each core in Hole U1385A. Discrete measurements of *P*-wave velocities were determined on section halves (one per section in Hole U1385D and Cores 339-U1385E-1H through 5H). Moisture and density (MAD) samples were measured once in every section as 10 cm^3 discrete samples. Color reflectance spectrometry and split-core point-logger magnetic susceptibility measurements were obtained for every section in each hole in 2 cm steps.

Whole-Round Multisensor Logger and Special Task Multisensor Logger measurements

GRA bulk density and magnetic susceptibility were measured on all core sections at Site U1385 at 2.5 cm intervals using the Special Task Multisensor Logger (STMSL) and, after allowing the cores to acclimate for 3 h, on the WRMSL (Fig. F20).

Gamma ray attenuation bulk density

Variations in GRA density may reflect variations in lithology, consolidation, cementation, and porosity. Measured GRA densities steadily increase in the upper 30–40 mbsf (Fig. F20), probably reflecting sediment compaction that decreases water content and porosity. However, GRA densities are relatively stable below 50 mbsf, parallel to the reduction in magnetic susceptibility values; thus, GRA densities also seem to reflect a long-term change in lithologic composition. Grain densities vary mostly between 2.7 and 2.8 g/cm^3 with no particular depth trend, although small-scale excursions are often mirrored in the GRA densities. GRA densities measured on the WRMSL are offset from those measured on the STMSL, with the former being greater by 0.04–0.08 g/cm^3. Instrument calibration, drift, and core expansion may account for the offset during analysis. MAD bulk densities are ~0.04 g/cm^3 lower than STMSL GRA densities in the upper 80 mbsf in Hole U1385A (Fig. F20), but MAD bulk densities approach GRA densities below this depth.

Magnetic susceptibility

The most notable aspect of all physical property records at Site U1385 is a gradual reduction of magnetic susceptibility values beginning at ~20 mbsf (Fig. F21). In the upper few meters, susceptibility values range from 20 × 10^{-5} to 40 × 10^{-5} SI, increase to a maximum of 40 × 10^{-5} to 50 × 10^{-5} SI with peaks up to 70 × 10^{-5} SI at ~20 mbsf, and decline downhole to an absolute low of 5–10 × 10^{-5} SI between 50 and 60 mbsf. Further downhole, susceptibilities recover but remain relatively steady at a low level between 5 × 10^{-5} to 15 × 10^{-5} SI. In addition to these general trends, magnetic susceptibility maintains a distinct high-amplitude variability until 50 mbsf and becomes comparatively low and less variable further downhole. This major change between 20 and 50 mbsf seems to correspond to either a general change in lithology or a diagenetic overprint, which is mirrored in low NGR counts (Fig. F22) and high L* values (see **"Natural gamma radiation"**). A likely factor for the main decrease of magnetic susceptibility is the reduction of fine-grained magnetite to iron sulfides in the sulfate reduction zone. This is also supported by the low anhysteretic remanent magnetization values (see **"Paleomagnetism"**). Despite this diagenetic overprint, magnetic susceptibility, NGR, and sediment reflectance property a* are positively correlated between ~40 and 90 mbsf, indicating that

a strong paleoenvironmental signal is retained in the magnetic susceptibility.

P-wave velocity

P-wave velocity was measured in all core sections at Site U1385 at 2.5 cm intervals on the WRMSL. Reasonable *P*-wave velocity measurements could only be retrieved for the upper ~70 mbsf on the WRMSL because of poor coupling between the liner and sediment in cores severely affected by core expansion (Fig. F20). *P*-wave velocity values closely follow GRA densities, with a steady increase from ~1490 m/s at the uppermost part of the holes to 1530 m/s at 15 mbsf to more variable data at the base of the holes (1550–1580 m/s). This relation, as well as the good match between *P*-wave velocities obtained by the WRMSL and on section halves (as long as signal quality permitted automatic processing), supports the reliability of the data. Problems arose below ~60 mbsf, where an increasing abundance of degassing cracks prevented good coupling between the core liner wall and sediment, deteriorating the acoustic signal of the WRMSL. Split-core *P*-wave velocity data were obtained further downhole to the base of Hole U1385D, where velocities vary around 1600 m/s with a maximum of 1650 m/s in the automatically processed data (Fig. F20). Caution must be taken in interpreting the manually picked data, in which greater subjectivity and poorer signal quality lead to higher scatter in the data. The method of manually picking data tends to overestimate velocities.

Natural gamma radiation

Measurements of NGR were made on all core sections, mostly at 20 cm spacing, and run on an integration time of 7 min per section (420 s per measurement). Cores 339-U1385B-1H to 3H and all cores in Hole U1385D were scanned at 10 cm resolution. Measured values range from 20 to 50 cps (Fig. F22).

Overall, NGR values increase with depth, but two different intervals can be distinguished. The first interval corresponds to the upper 50 mbsf, with values ranging from 25 to 45 cps. In the second interval, from 60 mbsf to the bottom of the hole, values range between 30 and 50 cps. In particular, the interval between 50 and 60 mbsf is characterized by a distinct decrease of NGR parallel to low magnetic susceptibility and high lightness (L*) values (Figs. F21, F22). Since L* is often coupled to carbonate content, dilution of potassium-bearing detrital material (clay) by higher carbonate contents might explain the low NGR and magnetic susceptibility signal.

NGR variations at Site U1385 exhibit regular cyclicity that becomes more prominent below 90 mbsf. High-frequency variations show a close correlation to GRA densities, likely reflecting the varying amounts of carbonate versus clay components. A positive correlation between NGR and magnetic susceptibility excursions becomes apparent below 40 mbsf. This correlation is not evident above this depth, hinting at a change in the factors influencing the sedimentary composition.

Moisture and density

Measurements of density, porosity, and grain density were undertaken on 59 samples from Hole U1385A. One sample was taken from every two sections at ~60 cm. Care was taken to avoid locations of obvious drilling disturbance. These samples were measured for wet mass and dry density to calculate bulk density and grain density.

The bulk densities from discrete samples are plotted in Figures F20 and F23 and show a data range of 1.55–1.91 g/cm^3. In the upper 60 mbsf of the hole, GRA densities and bulk densities of samples show certain offsets in which discrete samples are consistently lower than those measured on the WRMSL. Nevertheless, results from both techniques are in good agreement below 60 mbsf. This depth coincides with the sulfate–methane transition (SMT) zone at ~50–60 mbsf determined by pore water analysis. Because of the increasing amount of methane in the pore space, sediment expansion occurs below 60 mbsf, promoting the formation of cracks and voids. We interpret the disappearance of the offset between discrete sample and GRA densities below 60 mbsf as a consequence of gas expansion in the methanogenic zone. The degassing cracks cause underestimation of the GRA density values, causing them to have similar values to those obtained in discrete samples. This indicates that MAD bulk density measurements systematically underestimate the true density value. The reason for this systematic underestimation is not sufficiently resolved. Notably, only the dry volume of the sample was determined, not the wet bulk volume. Hence, the difference between the two density estimates might be related to the precipitation of salt crystals in the pore space during sample drying at 105°C, which would affect the determination of dry volumes by pycnometer and all further calculations (see **"Physical properties"** in the "Methods" chapter [Expedition 339 Scientists, 2013]).

Porosities range from 69% to 49% and generally decrease with depth, similar to moisture content, which is ~46% in the uppermost sections and decreases to ~27% at the base (Fig. F24). Bulk and dry densities exhibit increasing values with depth (Fig. F23). These trends primarily reflect compaction and dewatering of the sediment, which in the case of bulk density overprints the lithologic variations.

Grain density values range from ~2.7 to ~2.8 g/cm^3 downhole without a clear trend (Fig. F24). Grain densities are slightly higher than quartz density (2.65 g/cm^3) and probably reflect the varying degree of calcareous material in the sediment.

Thermal conductivity

Thermal conductivity was measured once per core using the full-space probe, usually in Section 3 near the middle of the section. Thermal conductivity in fine-grained sediments is, as a first approximation, a linear combination of the conductivities of the grains and the interstitial water and therefore depends upon porosity, water content, and lithology. Overall, thermal conductivity values range from 1.1 to 1.45 W/(m·K), without a clear increase with depth and poor correlation with moisture content.

Geochemistry

Volatile hydrocarbons

Headspace gas analysis was performed as a part of the standard protocol required for shipboard safety and pollution prevention monitoring. In total, 17 headspace samples from Hole U1385A (sampling resolution of one per core) were analyzed (Fig. F25; Table T21). Methane (C_1), ethane (C_2), and ethene ($C_{2=}$) were detected at this site. Methane is the only hydrocarbon present from the seafloor to 58.3 mbsf (Section 339-U1385A-7H-7) (Fig. F25). Ethane appears at 67.5 mbsf (Section 8H-7), and ethene begins to increase at 105.5 mbsf (Section 12H-7).

Methane varies between 3.7 and 6.7 ppmv in the uppermost five cores of Hole U1385A, increases to a maximum of 87,447 ppmv (Section 339-U1385A-11H-6), and then decreases to 56,190 ppmv at the base of the hole (150.11 mbsf).

Ethane ranges from 0.7 ppmv at 67.5 mbsf (Section 339-U1385A-8H-7) to 1.87 ppmv at 150.1 mbsf (Section 17H-5). The maximum ethane concentration is 2.4 ppmv at 94.5 mbsf (Section 11H-6).

Ethene ranges from 1 ppmv at 105.5 mbsf (Section 339-U1385A-12H-7) to 0.7 ppmv at 150.1 mbsf (Section 17H-5). The maximum concentration is 1.23 ppmv at 142 mbsf (Section 16H-6).

Sedimentary geochemistry

Sediment samples were collected for analysis of solid-phase geochemistry (inorganic and organic carbon) at a resolution of approximately one sample per core in Hole U1385B (Table T2). $CaCO_3$ content varies between 23 and 39 wt% (Fig. F4). Organic carbon is generally low (<1 wt%) (Fig. F26), except for one sample at 81.13 mbsf, which is 2.7 wt%.

Nitrogen (Fig. F26) varies between 0.04 and 0.09 wt%. Total nitrogen shows greatest variability in the upper 50 m of Hole U1385B.

The C/N ratio, used to distinguish the origin of organic matter (marine versus terrestrial) in the sediments (Emerson and Hedges, 1988; Meyers, 1997), indicates that the organic carbon is mainly of marine origin (C/N = 9–14.5) (Table T2; Fig. F26). One sample, at 81.13 mbsf, has a C/N ratio of 42.6, which indicates either greater terrestrial input or degradation of organic matter for this sample. Further analysis is required to determine the cause for this high ratio.

Interstitial water chemistry

Major cations and anions

Sulfate concentrations are near seawater values at the top of the section and decrease to zero at ~50 mbsf (Fig. F27A; Table T22). Alkalinity averages 9 meq/L from the top of the hole to 35 mbsf and progressively increases downhole (Fig. F27B; Table T22). Ammonium is 1000 µM at the surface and increases downhole, reaching 4800 µM near the base of the hole (Fig. F27C; Table T22). Diagenesis of organic matter at Site U1385 has led to the depletion of dissolved sulfate in interstitial water by the reaction of sulfate reduction:

$$53SO_4^{2-} + C_{106}H_{263}O_{110}N_{16}P \rightarrow 39CO_2 + 67HCO_3^- + 16NH_4^+ + 53HS^- + 39H_2O + HPO_4^{2-}.$$

In this process, sulfate is consumed and alkalinity (i.e., HCO_3^-, HS^-, and HPO_4^{2-}), ammonium, and phosphate are byproducts. The ratio of alkalinity increase to moles of sulfate reduced is ~2, but the increase in alkalinity in the sulfate reduction zone is only ~5 meq/L rather than the ~40 meq/L implied by the extent of sulfate reduction. This supports the hypothesis that authigenic precipitation of dolomite in the sulfate reduction zone is driving the 1:1 decrease in magnesium and calcium. In the presence of dolomite formation, each unit of decrease in both magnesium and calcium would be accompanied by a 2-unit decrease of interstitial water alkalinity. The observed loss of ~10 mM of magnesium and calcium in the sulfate reduction zone, if a result of dolomite formation, in part explains the smaller than expected but still significant alkalinity increase from sulfate reduction. The hydrogen sulfide ion produced by sulfate reduction can react with iron to form iron sulfide minerals (e.g., FeS and FeS_2), which are paramagnetic and have relatively low magnetic susceptibility. Sulfate reduction can also lead to the dissolution of magnetite and formation of minerals with

lower susceptibility. This process may explain the decrease in magnetic susceptibility below ~40 mbsf at Site U1385 (see **"Physical properties"**).

Once sulfate is depleted, methanogenesis becomes an important process in the sediment and methane begins to increase starting at ~50 mbsf, reaching a maximum concentration of >80,000 ppmv at ~95 mbsf (Fig. **F27D;** Table **T22**). In this process, organic matter is degraded and carbon dioxide, methane, ammonium, and phosphate are produced according to Redfield stoichiometry:

$$(CH_2O)_{106}(NH_3)_{16}(H_3PO_4) \rightarrow 53CO_2 + 53CH_4 + 16NH_3 + H_3PO_4^{2-}.$$

The SMT is very sharp at Site U1385 at ~50 mbsf, presumably because anaerobic methane oxidation in the presence of sulfate (i.e., $CH_4 + SO_4^{2-} \rightarrow HCO_3^- + HS^- + H_2O$) erases the signal of diffusive penetration of methane into the sulfate reduction zone above (Gieskes, 1983; Boetius et al., 2000).

Magnesium concentrations average ~45 mM in the uppermost 35 m of the core and then decrease to ~35 mM between 35 and 62 mbsf; thereafter, values average 32 mM to the base of the hole (Fig. **F28B;** Table **T22**). Calcium concentrations are 7.5 mM at the top of Hole U1385B, decrease to a minimum of 2.7 mM at 50 mbsf, and increase to 5.3 mM at the base of the hole (Fig. **F28A;** Table **T22**). The 1:1 decrease in calcium and magnesium in the zone of sulfate reduction suggests dolomite authigenesis, which was noted in smear slides and XRD analysis (see **"Lithostratigraphy"**). Potassium concentrations average 11.5 and 12 mM in the uppermost 25 mbsf and decrease downhole (Fig. **F28C;** Table **T22**). Below the sulfate reduction zone, the increase in calcium with a simultaneous decrease in magnesium and potassium may reflect the in situ alteration of volcanic detritus to form smectite (Perry et al., 1976). The possibility of this reaction is supported by the presence of dispersed volcanic glass noted in some sections (see **"Lithostratigraphy"**).

Minor elements

Barium, strontium, and lithium have similar patterns with near-constant values for the upper 50 mbsf, increasing rapidly between 50 and 82 mbsf, and gradually increasing below ~90 mbsf to the base of the hole (Fig. **F29A–F29C;** Table **T22**). Increases in concentrations of strontium may reflect dissolution of biogenic calcite (high in Sr) and secondary precipitation of inorganic calcite (low in Sr), although small contributions of strontium can also be derived from alteration of volcanic material (Gieskes, 1981). The similar patterns of barium and lithium suggest similar processes are controlling these elements. Boron shows an inverse pattern to barium, strontium, and lithium (Fig. **F29D;** Table **T22**). The most prominent feature of the silicon profile is the peak value at 100 mbsf (Fig. **F29E;** Table **T22**). Manganese concentrations decrease sharply from values of 18 µM at the surface to 12 µM at 43 mbsf. Iron shows a similar pattern, with values of 120 µM decreasing to 30 µM at 43.6 mbsf (Fig. **F30;** Table **T22**). Manganese and iron are near unchanging below 50 mbsf to the base of the hole.

Stable isotopes

Oxygen isotope values in interstitial water show considerable variability in the upper 30 mbsf, which is unexpected from a profile that should be dominated by diffusion (Fig. **F31A;** Table **T23**). An interval of generally higher $\delta^{18}O$ exists between 7.5 and 27 mbsf, reaching values as high as 0.41‰, which may reflect the increase in $\delta^{18}O$ of seawater during the last glacial period that has been attenuated by diffusion (McDuff, 1984; Schrag and DePaolo, 1993). The absence of a smooth $\delta^{18}O$ profile at Site U1385 suggests that either reactions are occurring in the sediment to maintain the sharp $\delta^{18}O$ gradients or that interstitial water samples have been contaminated by seawater circulated in the borehole during drilling operations. The contamination hypothesis is not supported by sulfate measurements (see **"Sampling contamination"**); however, the extent of contamination could be below our level of detection of sulfate. Another possibility is that the oscillations are higher-than-normal measurement noise of the Picarro water isotope analyzer, which was observed during the expedition. These possibilities are being investigated during postcruise analysis.

The δD value of 1‰ at the top of the hole reflects bottom water. Values of δD increase between 20 and 25 mbsf to 3.1‰ and fall between 25 and 44 mbsf before increasing to a maximum of 3.62‰ at 62.6 mbsf (Fig. **F31B;** Table **T23**). Following the δD maximum, values decrease downhole to 1.9‰ at 81.6 mbsf and remain more or less the same to the base of the hole. Lack of a strong correlation between $\delta^{18}O$ and δD suggests the two isotopologues of water are controlled by different processes (Fig. **F32**). The interval of high δD corresponds to a low in magnesium, which may partly indicate alteration of volcanic detritus to smectite. This process can increase the δD of interstitial water because the hydroxyl groups in clay minerals preferentially incorporate the light isotope of hydrogen relative to water. However, the interlayer waters of smectites are isotopically heavy

with respect to the water in which they form, which would decrease pore water δD. The relative isotopic fractionation of the structural hydrogen with respect to its formation water is greater than that of the interlayer water, but more information about the smectite structure is necessary to know which process is dominant in setting the pore water value in this case (Savin and Epstein, 1970; Suzuki and Epstein, 1976; Yeh, 1980; Lawrence and Gieskes, 1981; Liu and Epstein, 1984; Cerling et al., 1985).

Chloride is nonreactive in ocean sediment, and its concentration is dominantly controlled by diffusion and compaction-driven advection. However, uptake/release of water caused by formation/degradation of hydrated solids will increase/decrease the chloride concentration. The sharp gradients in the chloride profile at Site U1385 occurring simultaneously with changes in δD (Fig. **F31C**) suggest that the same process is controlling chloride and δD and that this process may be indeed the formation of smectite.

Sampling contamination

In order to evaluate whether the Rhizon samples were contaminated with drilling fluid, the sulfate concentration profile in the Rhizon samples from Hole U1385B was compared with that of the whole-round samples taken in Hole U1385A. Rapid sulfate reduction in the sediment makes sulfate concentration a good marker of drilling-fluid contamination; any contaminated Rhizon samples would have higher sulfate concentrations than the whole-round samples taken at the same depths. This would be particularly noticeable below the base of the sulfate reduction zone (~50 mbsf at Site U1389), after which sulfate concentration is 0 until the base of the hole. Also, in order to more precisely constrain the sulfate reduction zone, the sulfate concentration in the syringe samples taken from every section of Cores 339-U1385B-5H and 6H was measured. This enabled higher resolution comparison between Rhizon and squeeze samples in those cores.

All Rhizon samples analyzed for sulfate were taken from water following measurements with the Picarro water isotope analyzer. All samples were refrigerated at 4°C after isotope analysis, but the septa caps of the sample vials had been punctured by the Picarro sampling needle. To quantify the potential amount of evaporation that may affect our analysis, sulfate concentration was re-measured in some of the whole-round samples that had been analyzed for oxygen isotopes and stored in the same way. In Figure **F33**, the replicate whole-round measurements are identified as "Whole Rounds, post-isotope." If evaporation of the samples occurred, the replicates would be expected to all have higher sulfate concentrations than the original samples, but this is not the case. Instead, the whole-round sample sulfate concentrations that were re-measured after water isotope analysis are lower than the initial values. This indicates that the change was not due to sample evaporation; instead, the difference in the two measurements is likely due to different dilution methods used for sample preparation before analysis. The original whole-round measurements were automatically diluted by the ion chromatograph, whereas all of the later measurements were diluted using a Hamilton Microlab 500 autodiluter/dispenser prior to sample introduction to the ion chromatograph.

Where sulfate is present, samples diluted in the same way have indistinguishable sulfate concentration profiles within the error of the measurements and detection limits of the instrument. The lowest measured sulfate concentration in one of the Rhizon samples was 1.43 mM, which is half the concentration of our lowest measured calibration standard of ~2.7 mM. Below the end of the sulfate reduction zone, as measured in the squeezed samples, no detectable sulfate was present in any of the Rhizon samples.

The contamination from drilling fluid in the Rhizon samples is minimal, if present at all. Postcruise analysis will determine whether the downhole $\delta^{18}O$, δD, and chloride profiles are more sensitive to low levels (micromolar) of contamination below the level of detection of the ion chromatograph. This remains possible because the expected downhole changes in $\delta^{18}O$, δD, and chloride are on the order of 1%–3% of the present bottom water values, and the lowest sulfate measurement registered was ~6% of typical modern seawater sulfate concentration.

Downhole measurements

Heat flow

Twelve APCT-3 downhole temperature measurements were made in Holes U1385A, U1385B, and U1385D. Sediment temperatures ranged from 4.78°C at 34.6 mbsf to 8.02°C at 115.5 mbsf (Table **T24**), giving a geothermal gradient of 39.2°C/km (Fig. **F34**). The bottom water temperature was 3.4°C based on the average of the minimum temperature in the 12 APCT-3 temperature profiles. The thermal conductivity under in situ conditions was estimated from laboratory-determined thermal conductivity using the method of Hyndmann et al. (1974) (see **"Physical properties"** in the "Methods" chapter [Expedition 339 Scientists, 2013]). The calculated in situ values average 1.1% below the measured laboratory values. Thermal resistance was calculated by integrating the inverse of in situ thermal conductivity over depth

(Fig. F34). A heat flow of 47.5 mW/m^2 was obtained from the linear fit between temperature and thermal resistance (Pribnow et al., 2000). This value is in the lower half of the normal range for heat flow on the Portuguese margin (Grevemeyer et al., 2009).

Stratigraphic correlation

The mcd scale for Site U1385 was based solely on correlation of magnetic susceptibility between holes. Because susceptibility decreases significantly below ~60 mcd and because coring gaps increase below ~110 mcd, the correlation is not as robust in the lowermost part of the section (Fig. F35). Even so, enough distinct anomalies exist to permit some confidence that coeval features are being correlated between holes. The offsets and composite depths are listed in Table T25. A growth factor of 1.07–1.10 is calculated by linear regression for the different holes at Site U1385, indicating a 7%–10% increase in mcd values relative to mbsf values (Fig. F36).

The five holes cored at Site U1385 provided ample sediment for constructing an ultracomplete spliced stratigraphic section containing no notable gaps or disturbed intervals. We refer to this splice as the "primary splice" (Fig. F37; Table T26). Two nearly complete secondary splices were also constructed, one using intervals from Holes U1385A and U1385B (the "AB splice") and the other using intervals from Holes U1385D and U1385E (the "DE splice") (Tables T27, T28; Fig. F37). Hole U1385C is not included in any of the splices because it is a single core from the uppermost part of the section, which is well sampled by the other holes. Where possible, we avoided including intervals in the splices that were disturbed significantly by drilling, voids, and interstitial water samples (Table T14). In addition, all magnetic susceptibility data were cleaned for the top of each section and measurement outliers (Table T29). No corrections were made for the small normal faults observed within several sections of Site U1385.

The goal of creating the primary splice was to ensure that a complete section of the most representative intervals was identified. Using this splice, nondestructive data sets collected along the cores, such as physical and magnetic properties, can be spliced into complete composite records. The two nearly complete secondary splices were constructed to maximize the material available for sampling while adhering to the IODP sampling policy, which seeks to preserve representative material from a site for future studies. Both secondary splices are complete enough that it will only be necessary to sample within the single primary splice in a few relatively narrow intervals.

Finally, a linear regression through the core tops of all holes at Site U1385 was applied to compress the expanded meters composite depth scale to the meters below seafloor scale (Fig. F38). This recalculated mbsf depth scale (mbsf*) facilitates a direct comparison of the spliced records with data plotted on the original mbsf scale. The linear regression was forced through the origin (i.e., at zero mcd and mbsf*) and gives an average compression factor of 0.9093254414.

References

Alvarez Zarikian, C.A., Stepanova, A.Y., and Gruetzner, J., 2007. Glacial-interglacial variations in Ostracod assemblage composition at IODP Site U1314 in the North Atlantic. *Eos., Trans. Am. Geophys. Union,* 88(52)(Suppl.):PP41C-0688. (Abstract) **http://www.agu.org/meetings/fm07/waisfm07.html**

Bartoli, G., Sarnthein, M., Weinelt, M., Erlenkeuser, H., Garbe-Schönberg, D., and Lea, D.W., 2005. Final closure of Panama and the onset of Northern Hemisphere glaciation. *Earth Planet. Sci. Lett.,* 237(1–2):33–44. **doi:10.1016/j.epsl.2005.06.020**

Blum, P., 1997. Physical properties handbook: a guide to the shipboard measurement of physical properties of deep-sea cores. *ODP Tech. Note,* 26. **doi:10.2973/odp.tn.26.1997**

Boetius, A., Ravenschlag, K., Schubert, C.J., Rickert, D., Widdel, F., Gieseke, A., Amann, R., Jørgensen, B.B., Witte, U., and Pfannkuche, O., 2000. A marine microbial consortium apparently mediating anaerobic oxidation of methane. *Nature (London, U. K.),* 407(6804):623–626. **doi:10.1038/35036572**

Cerling, T.E., Brown, F.H., and Bowman, J.R., 1985. Low-temperature alteration of volcanic glass: hydration, Na, K, ^{18}O and Ar mobility. *Chem. Geol.,* 52(3–4):281–293. **doi:10.1016/0168-9622(85)90040-5**

Channell, J.E.T., Kanamatsu, T., Sato, T., Stein, R., Alvarez Zarikian, C.A., Malone, M.J., and the Expedition 303/306 Scientists, 2006. *Proc. IODP,* 303/306: College Station, TX (Integrated Ocean Drilling Program Management International, Inc.). **doi:10.2204/iodp.proc.303306.2006**

Cronin, T.M., DeMartino, D.M., Dwyer, G.S., and Rodriguez-Lazaro, J., 1999. Deep-sea ostracode species diversity: response to late Quaternary climate change. *Mar. Micropaleontol.,* 37(3–4): 231–249. **doi:10.1016/S0377-8398(99)00026-2**

Curry, W.B., and Oppo, D.W., 2005. Glacial water mass geometry and the distribution of $\delta^{13}C$ of ΣCO_2 in the western Atlantic Ocean. *Paleoceanography,* 20:PA1017. **doi:10.1029/2004PA001021**

Didié, C., and Bauch, H.A., 2000. Species composition and glacial–interglacial variations in the ostracode fauna of the northeast Atlantic during the past 200,000 years. *Mar. Micropaleontol.,* 40(1–2):105–129. **doi:10.1016/S0377-8398(00)00034-7**

Dingle, R.V., and Lord, A.R., 1990. Benthic ostracods and deep water-masses in the Atlantic Ocean. *Palaeogeogr., Palaeoclimatol., Palaeoecol.,* 80(3–4):213–235. **doi:10.1016/0031-0182(90)90133-R**

Emerson, S., and Hedges, J.I., 1988. Processes controlling the organic carbon content of open ocean sediments. *Paleoceanography,* 3(5):621–634. **doi:10.1029/PA003i005p00621**

Expedition 339 Scientists, 2013. Methods. *In* Stow, D.A.V., Hernández-Molina, F.J., Alvarez Zarikian, C.A., and the Expedition 339 Scientists, *Proc. IODP,* 339: Tokyo (Integrated Ocean Drilling Program Management International, Inc.). **doi:10.2204/iodp.proc.339.102.2013**

Flores, J.-A., Colmenero-Hidalgo, E., Mejía-Molina, A.E., Baumann, K.-H., Hendericks, J., Larsson, K., Prabhu, C.N., Sierro, F.J., and Rodrigues, T., 2010. Distribution of large *Emiliania huxleyi* in the central and northeast Atlantic as a tracer of surface ocean dynamics during the last 25,000 years. *Mar. Micropaleontol.,* 76(3–4):53–66. **doi:10.1016/j.marmicro.2010.05.001**

Gieskes, J.M., 1981. Deep-sea drilling interstitial water studies: implications for chemical alteration of the oceanic crust, Layers I and II. *In* Warme, J.E., Douglas, R.G., and Winterer, E.L. (Eds.), *The Deep Sea Drilling Project: A Decade of Progress*. Spec. Publ.—Soc. Econ. Paleontol. Mineral., 32:149–167.

Gieskes, J.M., 1983. The chemistry of interstitial waters of deep sea sediments: interpretation of deep sea drilling data. *In* Riley, J.P., and Chester, R. (Eds.), *Chemical Oceanography* (Vol. 8): London (Academic), 221–269.

Gooday, A.J., 1993. Deep-sea benthic foraminiferal species which exploit phytodetritus: characteristic features and controls on distribution. *Mar. Micropaleontol.,* 22(3):187–205. **doi:10.1016/0377-8398(93)90043-W**

Grevemeyer, I., Kaul, N., and Kopf, A., 2009. Heat flow anomalies in the Gulf of Cadiz and off Cape San Vincente, Portugal. *Mar. Pet. Geol.,* 26(6):795–804. **doi:10.1016/j.marpetgeo.2008.08.006**

Gupta, A.K., and Thomas, E., 2003. Initiation of Northern Hemisphere glaciation and strengthening of the northeast Indian monsoon: Ocean Drilling Program Site 758, eastern equatorial Indian Ocean. *Geology,* 31(1):47–50. **doi:10.1130/0091-7613(2003)031<0047:IONHGA>2.0.CO;2**

Hayward, B.W., 2002. Late Pliocene to middle Pleistocene extinctions of deep-sea benthic foraminifera ("*Stilostomella* extinction") in the southwest Pacific. *J. Foraminiferal Res.,* 32(3):274–307. **doi:10.2113/32.3.274**

Heusser, L.E., 1985. Quaternary palynology of marine sediments in the northeast Pacific, northwest Atlantic, and Gulf of Mexico. *In* Bryant, V.M., Jr., and Holloway, R.G. (Eds.), *Pollen Records of Late Quaternary North American Sediments:* Dallas, Texas (AASP Found.), 385–403.

Hyndman, R.D., Erickson, A.J., and Von Herzen, R.P., 1974. Geothermal measurements on DSDP Leg 26. *In* Davies, T.A., Luyendyk, B.P., et al., *Init. Repts. DSDP,* 26: Washington, DC (U.S. Govt. Printing Office), 451–463. **doi:10.2973/dsdp.proc.26.113.1974**

Kaiho, K., 1999. Effect of organic carbon flux and dissolved oxygen on the benthic foraminiferal oxygen index (BFOI). *Mar. Micropaleontol.,* 37(1):67–76. **doi:10.1016/S0377-8398(99)00008-0**

Kawagata, S., Hayward, B.W., Grenfell, H.R., and Sabaa, A., 2005. Mid-Pleistocene extinction of deep-sea foraminifera in the North Atlantic Gateway (ODP Sites 980 and 982). *Palaeogeogr., Palaeoclimatol., Palaeoecol.,* 221(3–4):267–291. **doi:10.1016/j.palaeo.2005.03.001**

Kirschvink, J.L., 1980. The least-squares line and plane and the analysis of palaeomagnetic data. *Geophys. J. R. Astron. Soc.,* 62(3):699–718. **doi:10.1111/j.1365-246X.1980.tb02601.x**

Lawrence, J.R., and Gieskes, J.M., 1981. Constraints on water transport and alteration in the oceanic crust from the isotopic composition of pore water. *J. Geophys. Res., [Solid Earth],* 86(B9):7924–7934. **doi:10.1029/JB086iB09p07924**

Lézine, A.-M., and Denèfle, M., 1997. Enhanced anticyclonic circulation in the eastern North Atlantic during cold intervals of the last deglaciation inferred from deep-sea pollen records. *Geology,* 25(2):119–122. **doi:10.1130/0091-7613(1997)025<0119:EACITE>2.3.CO;2**

Liu, K.-K., and Epstein, S., 1984. The hydrogen isotope fractionation between kaolinite and water. *Isot. Geochem.,* 46(4):335–350. **doi:10.1016/0009-2541(84)90176-1**

Lourens, L.J., Antonarakou, A., Hilgen, F.J., Van Hoof, A.A.M., Vergnaud-Grazzini, C., and Zachariasse, W.J., 1996a. Evaluation of the Plio-Pleistocene astronomical timescale. *Paleoceanography,* 11(4):391–414. **doi:10.1029/96PA01125**

Lourens, L.J., Hilgen, F.J., and Raffi, I., 1998. Base of large *Gephyrocapsa* and astronomical calibration of early Pleistocene sapropels in Site 967 and Hole 969D: solving the chronology of the Vrica section (Calabria, Italy). *In* Robertson, A.H.F., Emeis, K.-C., Richter, C., and Camerlenghi, A. (Eds.), *Proc. ODP, Sci. Results,* 160: College Station, TX (Ocean Drilling Program), 191–197. **doi:10.2973/odp.proc.sr.160.017.1998**

Lourens, L.J., Hilgen, F.J., Raffi, I., and Vergnaud-Grazzini, C., 1996b. Early Pleistocene chronology of the Vrica section (Calabria, Italy). *Paleoceanography,* 11(6):797–812. **doi:10.1029/96PA02691**

Margari, V., Skinner, L.C., Tzedakis, P.C., Ganopolski, A., Vautravers, M., and Shackleton, N.J., 2010. The nature of millennial-scale climate variability during the past two glacial periods. *Nat. Geosci.,* 3(2):127–131. **doi:10.1038/ngeo740**

Martrat, B., Grimalt, J.O., Shackleton, N.J., de Abreu, L., Hutterli, M.A., and Stocker, T.F., 2007. Four climate cycles of recurring deep and surface water destabilizations on the Iberian margin. *Science,* 317(5837):502–507. **doi:10.1126/science.1139994**

McDuff, R.E., 1984. The chemistry of interstitial waters from the upper ocean crust, Site 395, Deep Sea Drilling Project Leg 78B. *In* Hyndman, R.D., Salisbury, M.H., et al., *Init. Repts. DSDP,* 78B: Washington, DC (U.S. Govt. Printing Office), 795–799. **doi:10.2973/dsdp.proc.78b.114.1984**

Meyers, P.A., 1997. Organic geochemical proxies of paleoceanographic, paleolimnologic, and paleoclimatic processes. *Org. Geochem.,* 27(5–6):213–250. **doi:10.1016/S0146-6380(97)00049-1**

Murray, J.W., 2006. *Ecology and Applications of Benthic Foraminifera*: Cambridge (Cambridge Univ. Press).

Naughton, F., Sánchez Goñi, M.F., Desprat, S., Turon, J.-L., Duprat, J., Malaizé, B., Joli, C., Cortijo, E., Drago, T., and Freitas, M.C., 2007. Present-day and past (last 25,000 years) marine pollen signal off western Iberia. *Mar. Micropaleontol.*, 62(2):91–114. **doi:10.1016/j.marmicro.2006.07.006**

Perry, E.A., Jr., Gieskes, J.M., and Lawrence, J.R., 1976. Mg, Ca and O^{18}/O^{16} exchange in the sediment-pore water system, Hole 149, DSDP. *Geochim. Cosmochim. Acta,* 40(4):413–423. **doi:10.1016/0016-7037(76)90006-5**

Pribnow, D., Kinoshita, M., and Stein, C., 2000. *Thermal Data Collection and Heat Flow Recalculations for Ocean Drilling Program Legs 101–180:* Hanover, Germany (Inst. Joint Geosci. Res., Inst. Geowiss. Gemeinschaftsauf. [GGA]). **http://www-odp.tamu.edu/publications/heatflow/ODPReprt.pdf**

Raffi, I., Backman, J., Fornaciari, E., Pälike, H., Rio, D., Lourens, L., and Hilgen, F., 2006. A review of calcareous nannofossil astrobiochronology encompassing the past 25 million years. *Quat. Sci. Rev.,* 25(23–24):3113–3137. **doi:10.1016/j.quascirev.2006.07.007**

Raffi, I., Backman, J., Rio, D., and Shackleton, N.J., 1993. Plio–Pleistocene nannofossil biostratigraphy and calibration to oxygen isotope stratigraphies from Deep Sea Drilling Project Site 607 and Ocean Drilling Program Site 677. *Paleoceanography,* 8(3):387–408. **doi:10.1029/93PA00755**

Raymo, M.E., Ruddiman, W.F., Backman, J., Clement, B.M., and Martinson, D.G., 1989. Late Pliocene variation in Northern Hemisphere ice sheets and North Atlantic deep water circulation. *Paleoceanography,* 4(4):413–446. **doi:10.1029/PA004i004p00413**

Roucoux, K.H., Tzedakis, P.C., de Abreu, L., and Shackleton, N.J., 2006. Climate and vegetation changes 180,000 to 345,000 years ago recorded in a deep-sea core off Portugal. *Earth Planet. Sci. Lett.,* 249(3–4):307–325. **doi:10.1016/j.epsl.2006.07.005**

Sánchez Goñi, M.F., Cacho, I., Turon, J.-L., Guiot, J., Sierro, F.J., Peypouquet, J.-P., Grimalt, J.O., and Shackleton, N.J., 2002. Synchroneity between marine and terrestrial responses to millennial scale climatic variability during the last glacial period in the Mediterranean region. *Clim. Dyn.,* 19(1):95–105. **doi:10.1007/s00382-001-0212-x**

Sánchez Goñi, M.F., Eynaud, F., Turon, J.L., and Shackleton, N.J., 1999. High-resolution palynological record off the Iberian margin: direct land-sea correlation for the last interglacial complex. *Earth Planet. Sci. Lett.,* 171(1):123–137. **doi:10.1016/S0012-821X(99)00141-7**

Sánchez Goñi, M.F., Landais, A., Cacho, I., Duprat, J., and Rossignol, L., 2009. Contrasting intrainterstadial climatic evolution between high and middle North Atlantic latitudes: a close-up of Greenland Interstadials 8 and 12. *Geochem., Geophys., Geosyst.,* 10(4):Q04U04. **doi:10.1029/2008GC002369**

Sánchez Goñi, M.F., Landais, A., Fletcher, W.J., Naughton, F., Desprat, S., and Duprat, J., 2008. Contrasting impacts of Dansgaard-Oeschger events over a western European latitudinal transect modulated by orbital parameters. *Quat. Sci. Rev.,* 27(11–12):1136–1151. **doi:10.1016/j.quascirev.2008.03.003**

Savin, S.M., and Epstein, S., 1970. The oxygen and hydrogen isotope geochemistry of clay minerals. *Geochim. Cosmochim. Acta,* 34(1):25–42. **doi:10.1016/0016-7037(70)90149-3**

Schnitker, D., 1984. High resolution records of benthic foraminifers in the late Neogene of the northeastern Atlantic. *In* Roberts, D.G., Schnitker, D., et al., *Init. Repts. DSDP,* 81: Washington, DC (U.S. Govt. Printing Office), 611–622. **doi:10.2973/dsdp.proc.81.117.1984**

Schrag, D.P., and DePaolo, D.J., 1993. Determination of $\delta^{18}O$ of seawater in the deep ocean during the Last Glacial Maximum. *Paleoceanography,* 8(1):1–6. **doi:10.1029/92PA02796**

Shackleton, N.J., Hall, M.A., and Vincent, E., 2000. Phase relationships between millennial-scale events 64,000–24,000 years ago. *Paleoceanography,* 15(6):565–569. **doi:10.1029/2000PA000513**

Shackleton, N.J., Fairbanks, R.G., Chiu, T., and Parrenin, F., 2004. Absolute calibration of the Greenland time scale: implications for Antarctic time scales and for $\Delta^{14}C$. *Quat. Sci. Rev.,* 23(14–15):1513–1522. **doi:10.1016/j.quascirev.2004.03.006**

Shackleton, N.J., Sánchez-Goñi, M.F., Pailler, D., and Lancelot, Y., 2003. Marine isotope Substage 5e and the Eemian interglacial. *Global Planet. Change,* 36(3):151–155. **doi:10.1016/S0921-8181(02)00181-9**

Sierro, F.J., Hernandez-Almeida, I., Alonso-Garcia, M., and Flores, J.A., 2009. Data report: Pliocene–Pleistocene planktonic foraminifer bioevents at IODP Site U1313. *In* Channell, J.E.T., Kanamatsu, T., Sato, T., Stein, R., Alvarez Zarikian, C.A., Malone, M.J., and the Expedition 303/306 Scientists, *Proc. IODP,* 303/306: College Station, TX (Integrated Ocean Drilling Program Management International, Inc.). **doi:10.2204/iodp.proc.303306.205.2009**

Skinner, L.C., Elderfield, H., and Hall, M., 2007. Phasing of millennial climate events and northeast Atlantic deep-water temperature change since 50 ka BP. *In* Schmittner, A., Chiang, J.C.H., and Hemming, S.R. (Eds.), *Ocean Circulation: Mechanisms and Impacts—Past and Future Changes of Meridional Overturning*. Geophys. Monogr., 173:197–208. **doi:10.1029/173GM14**

Skinner, L.C., and Shackleton, N.J., 2006. Deconstructing Terminations I and II: revisiting the glacioeustatic paradigm based on deep-water temperature estimates. *Quat. Sci. Rev.*, 25(23–24):3312–3321. **doi:10.1016/j.quascirev.2006.07.005**

Stow, D.A.V., 2005. *Sedimentary Rocks in the Field: A Colour Guide:* London (Manson Publ.).

Stow, D.A.V., and Tabrez, A.R., 1998. Hemipelagites: processes, facies and model. *Geol. Soc. Spec. Publ.,* 129(1):317–337. **doi:10.1144/GSL.SP.1998.129.01.19**

Suzuki, T., and Epstein, S., 1976. Hydrogen isotope fractionation between OH-bearing minerals and water. *Geo-*

chim. Cosmochim. Acta, 40(10):1229–1240. **doi:10.1016/0016-7037(76)90158-7**

Turon, J.L., 1984. Le phytoplancton dans l'environnement actuel de l'Atlantique nord oriental. Evolution climatique et hydrologique depuis le dernier maximum glaciaire. *Mem. Inst. Geol. Bassin Aquitaine,* 17.

Tzedakis, P.C., Pälike, H., Roucoux, K.H., and de Abreu, L., 2009. Atmospheric methane, southern European vegetation and low–mid latitude links on orbital and millennial timescales. *Earth Planet. Sci. Lett.,* 277(3–4):307–317. **doi:10.1016/j.epsl.2008.10.027**

Tzedakis, P.C., Roucoux, K.H., de Abreu, L., and Shackleton, N.J., 2004. The duration of forest stages in southern Europe and interglacial climate variability. *Science,* 306(5705):2231–2235. **doi:10.1126/science.1102398**

Vautravers, M.J., and Shackleton, N.J., 2006. Centennial-scale surface hydrology off Portugal during marine isotope Stage 3: insights from planktonic foraminiferal fauna variability. *Paleoceanography,* 21(3):PA3004. **doi:10.1029/2005PA001144**

Wei, W., 1993. Calibration of upper Pliocene–lower Pleistocene nannofossil events with oxygen isotope stratigraphy. *Paleoceanography,* 8(1):85–99. **doi:10.1029/92PA02504**

Xuan, C., and Channell, J.E.T., 2009. UPmag: MATLAB software for viewing and processing U channel or other pass-through paleomagnetic data. *Geochem., Geophys., Geosyst.,* 10(10):Q10Y07. **doi:10.1029/2009GC002584**

Yasuhara, M., Cronin, T.M., Hunt, G., and Hodell, D.A., 2009a. Deep-sea ostracods from the south Atlantic sector of the Southern Ocean during the last 370,000 years. *J. Paleontol.,* 83(6):914–930. **doi:10.1666/08-149.1**

Yasuhara, M., Okahashi, H., and Cronin, T.M., 2009b. Taxonomy of Quaternary deep-sea ostracods from the western North Atlantic Ocean. *Palaeontology,* 52(4):879–931. **doi:10.1111/j.1475-4983.2009.00888.x**

Yeh, H.-W., 1980. D/H ratios and late-stage dehydration of shales during burial. *Geochim. Cosmochim. Acta,* 44(2):341–352. **doi:10.1016/0016-7037(80)90142-8**

Publication: 17 June 2013
MS 339-103

Figure F1. Maps of (**A**) West Iberian margin showing (**B**) detailed bathymetry and locations of *Marion Dufresne* (MD) piston cores and Site U1385 (37°34.285′N, 10°7.562′W) relative to seismic lines in the drilling area.

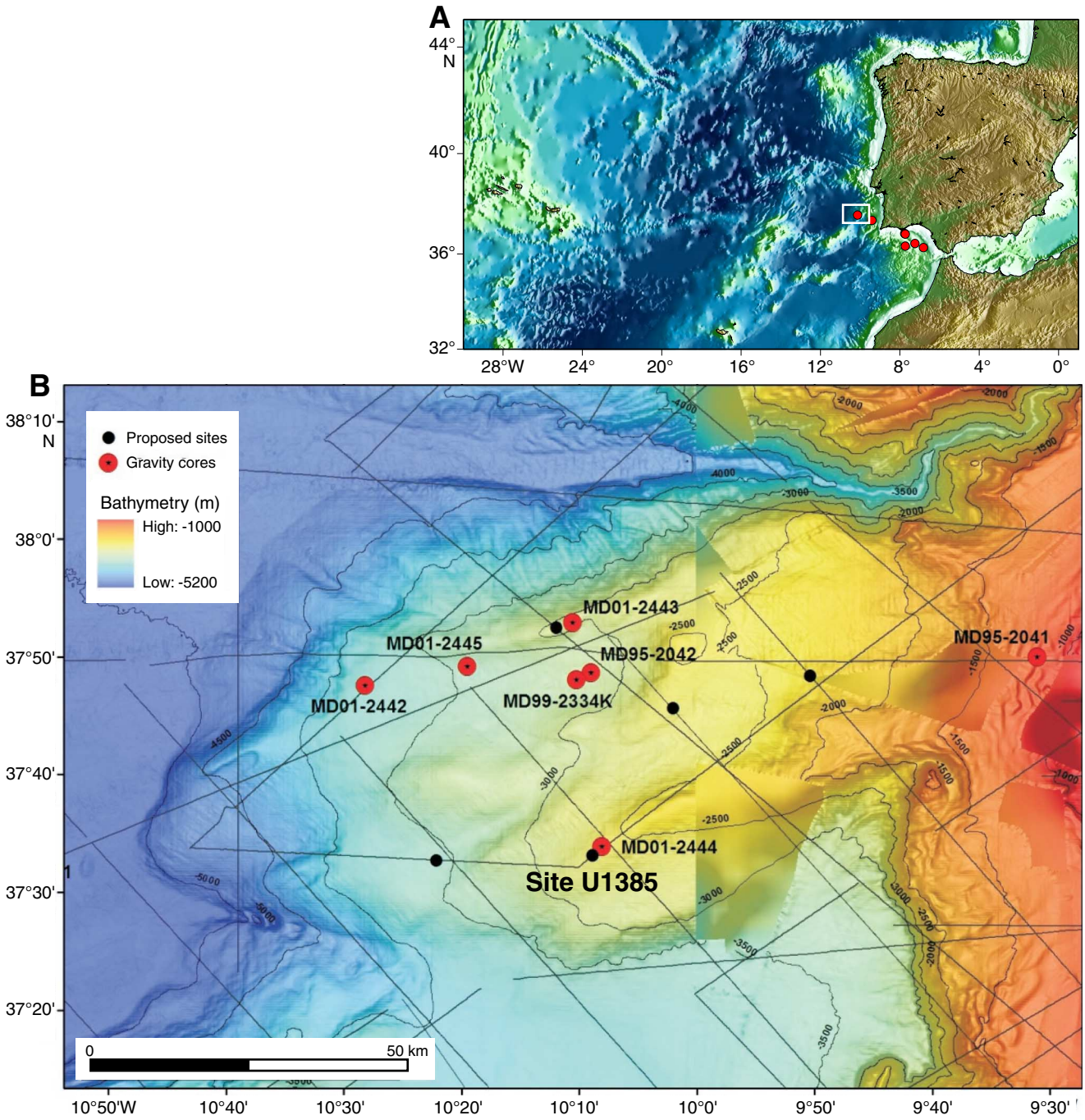

Figure F2. Bathymetric map of Site U1385 seafloor.

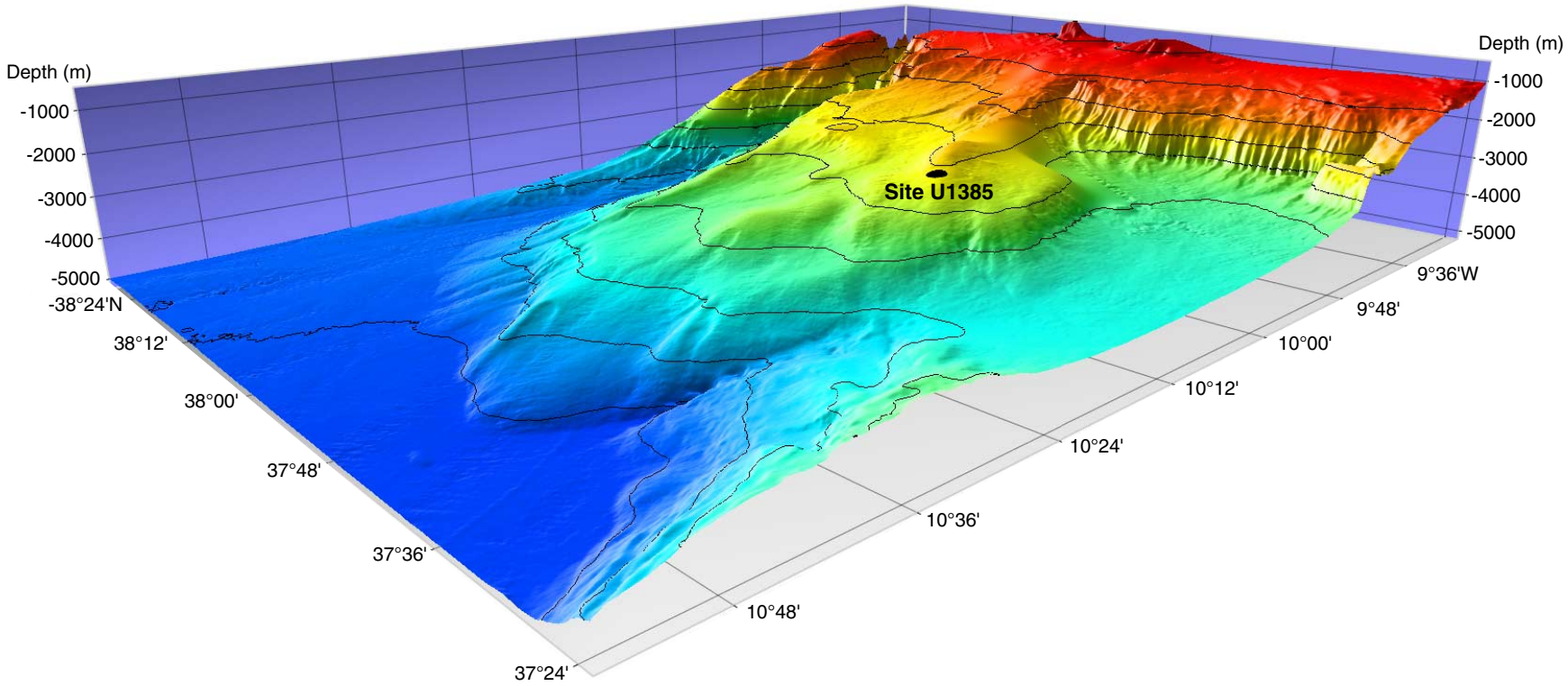

Figure F3. Correlation of $\delta^{18}O$ record of GISP ice core (red) to $\delta^{18}O$ of *Globigerina bulloides* (black) in Core MD95-2042. Resulting correlation of Vostok δD (green) and benthic $\delta^{18}O$ of Core MD95-2042 (blue) is based on methane synchronization. VPDB = Vienna Peedee belemnite, VSMOW = Vienna standard mean ocean water.

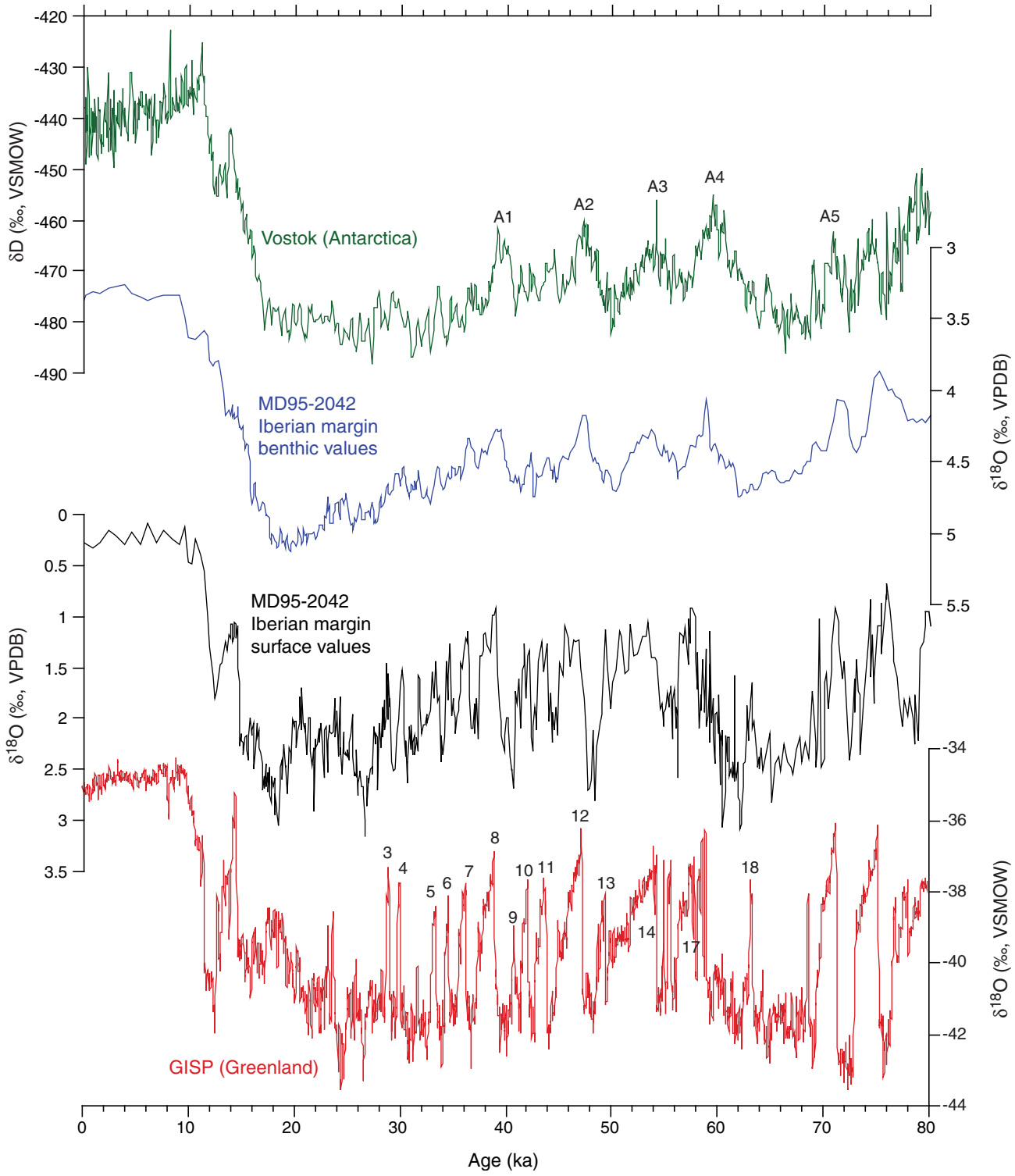

Figure F4. Plot of calcium carbonate, Hole U1385B.

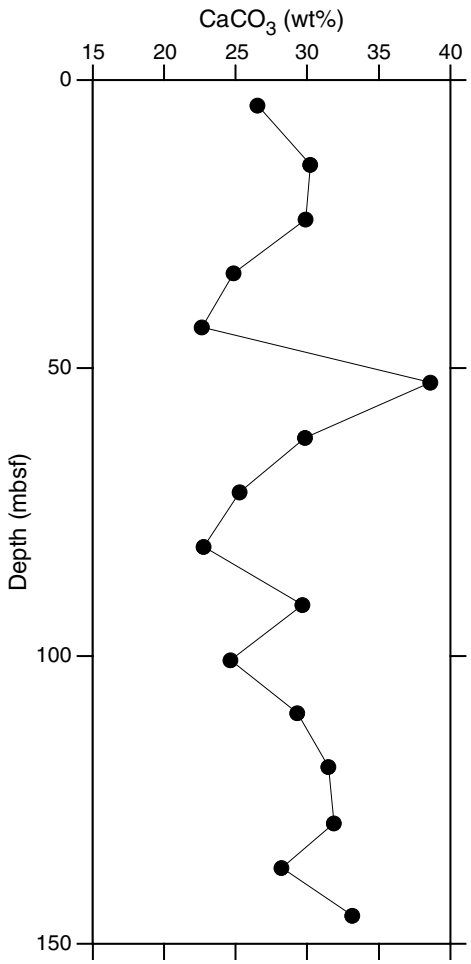

Figure F5. Plot of sediment component abundances estimated from smear slides, Hole U1385A. Note that data points are the original estimates made during shipboard core description; carbonate contents subsequently have been revised down.

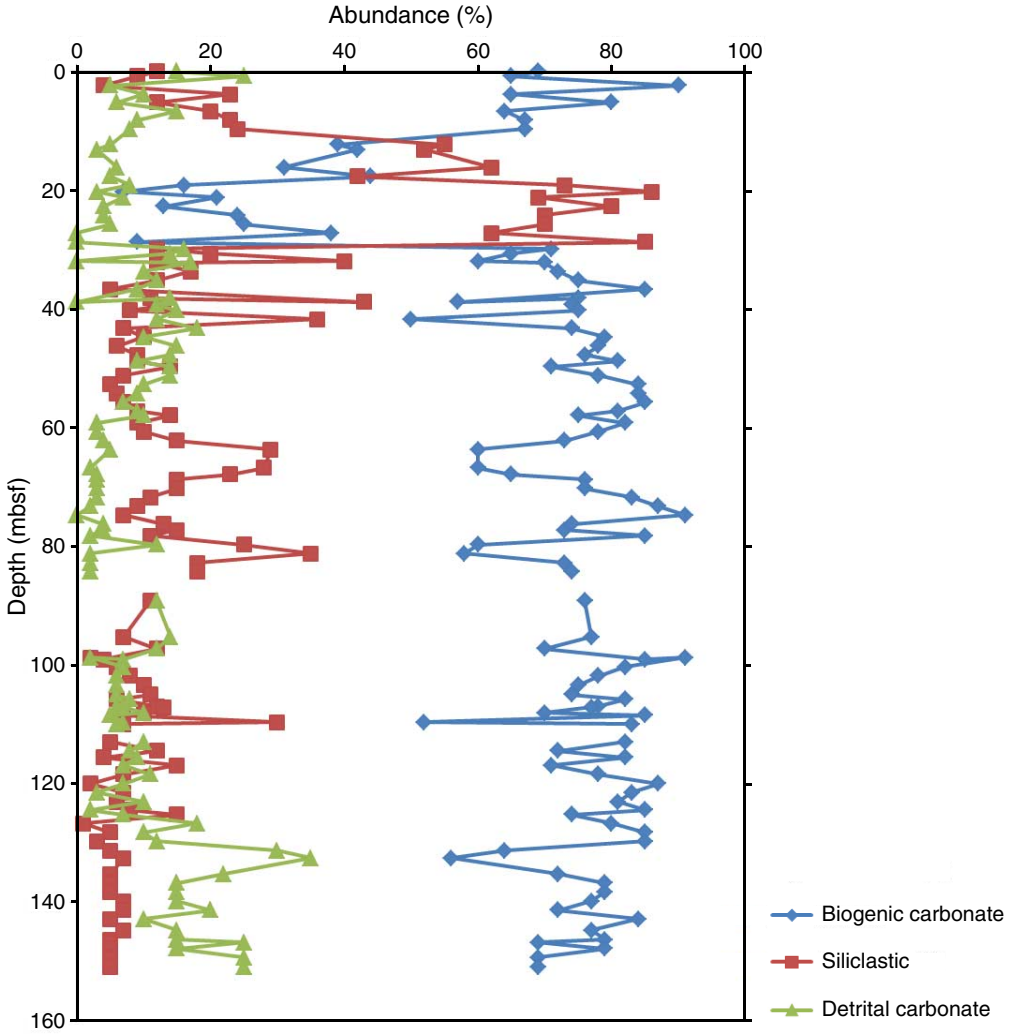

Figure F6. Graphic lithology summary, Hole U1385A. Lithologies revised according to the scheme in Table T3.

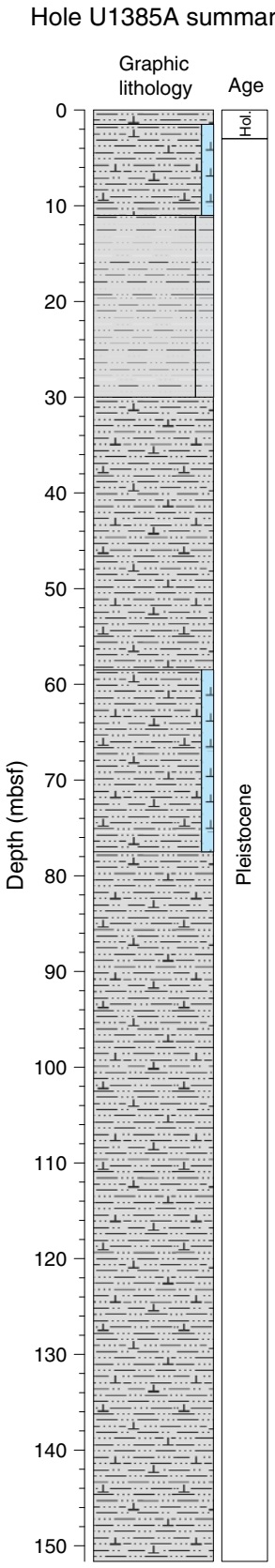

Figure F7. Graphic lithology summaries, Site U1385. **A.** Hole U1385A. (Continued on next four pages.).

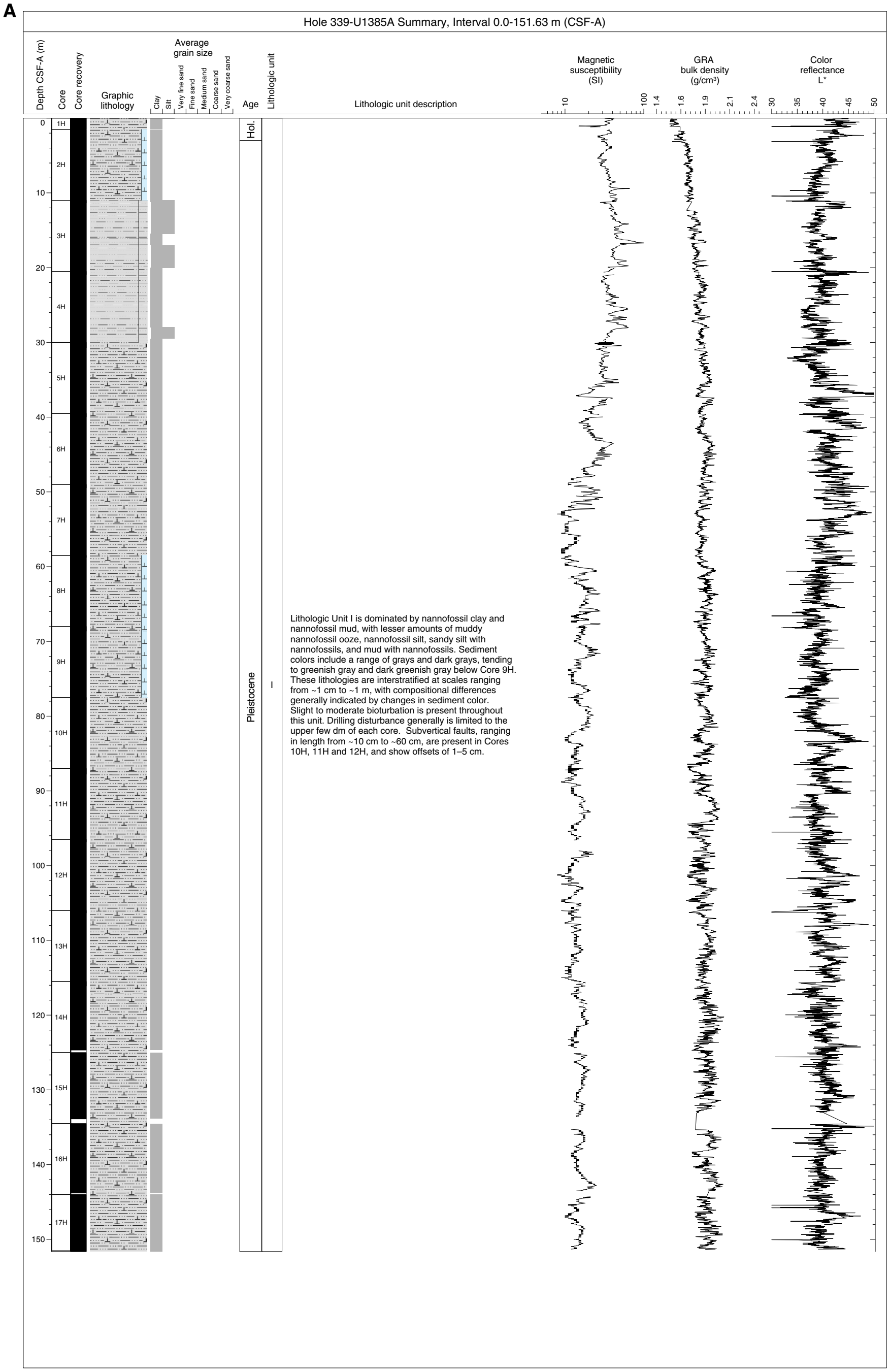

Figure F7 (continued). B. Hole U1385B. (Continued on next page.)

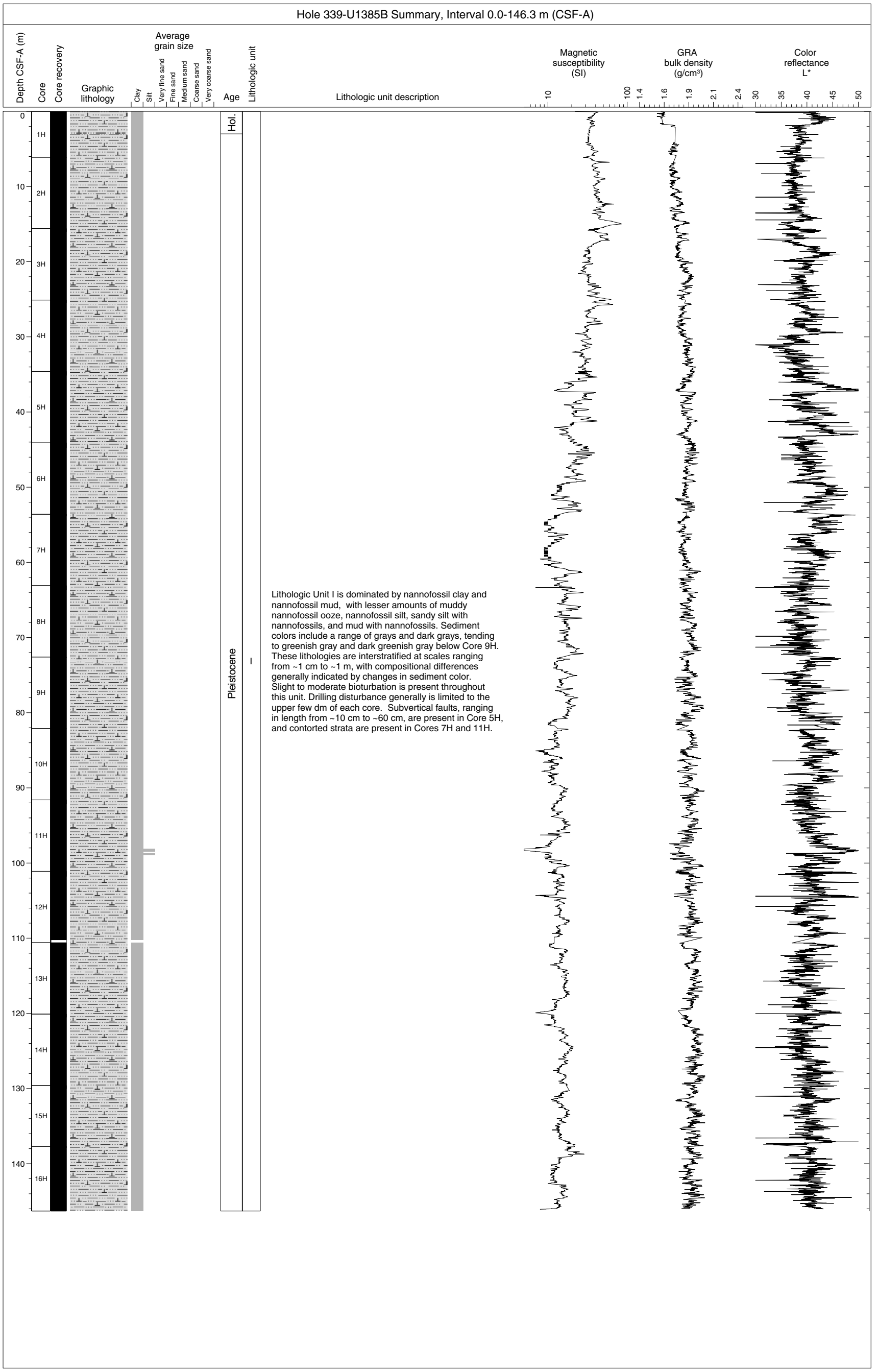

Figure F7 (continued). C. Hole U1385C. (Continued on next page.)

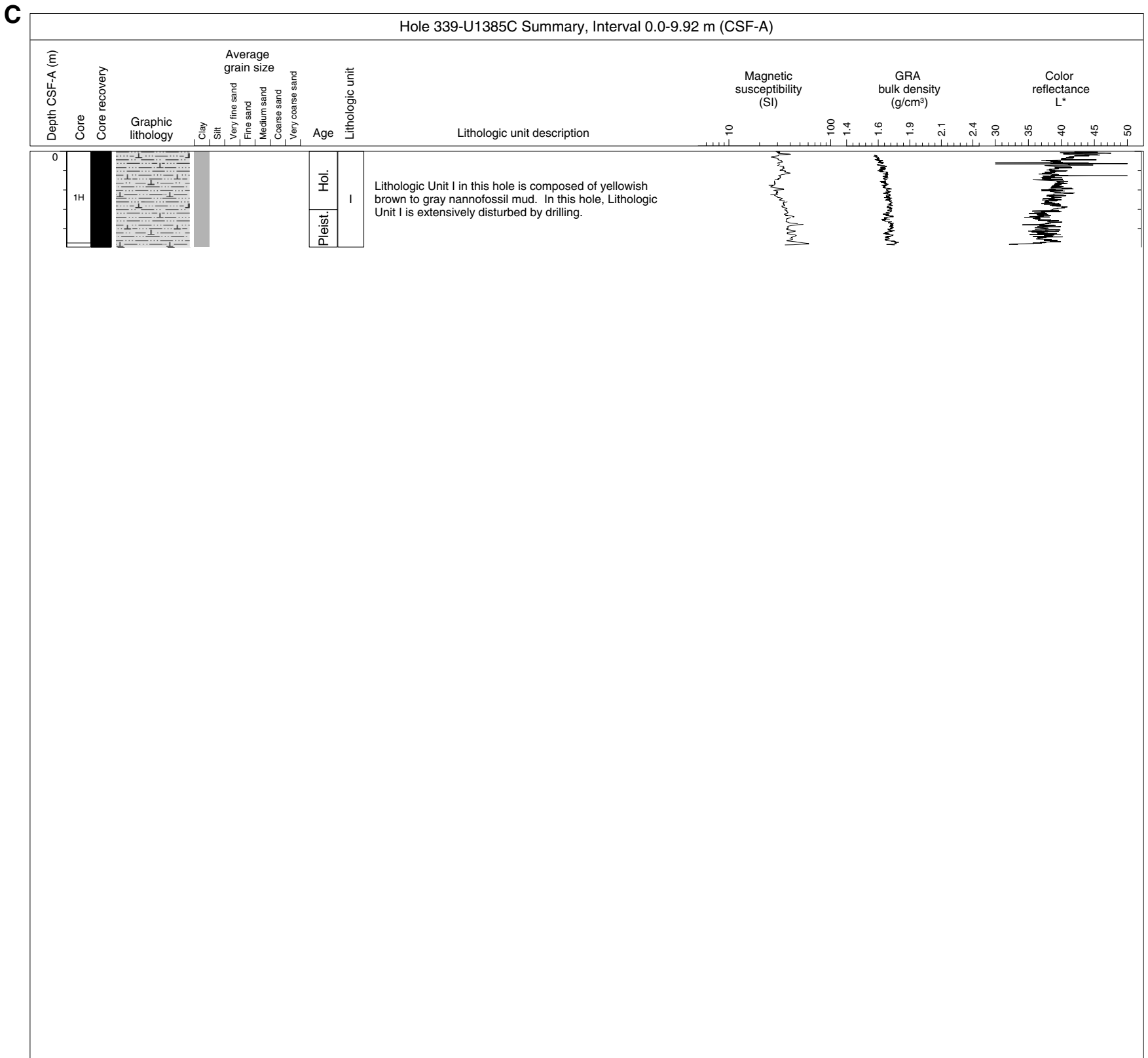

Figure F7 (continued). D. Hole U1385D (Continued on next page.)

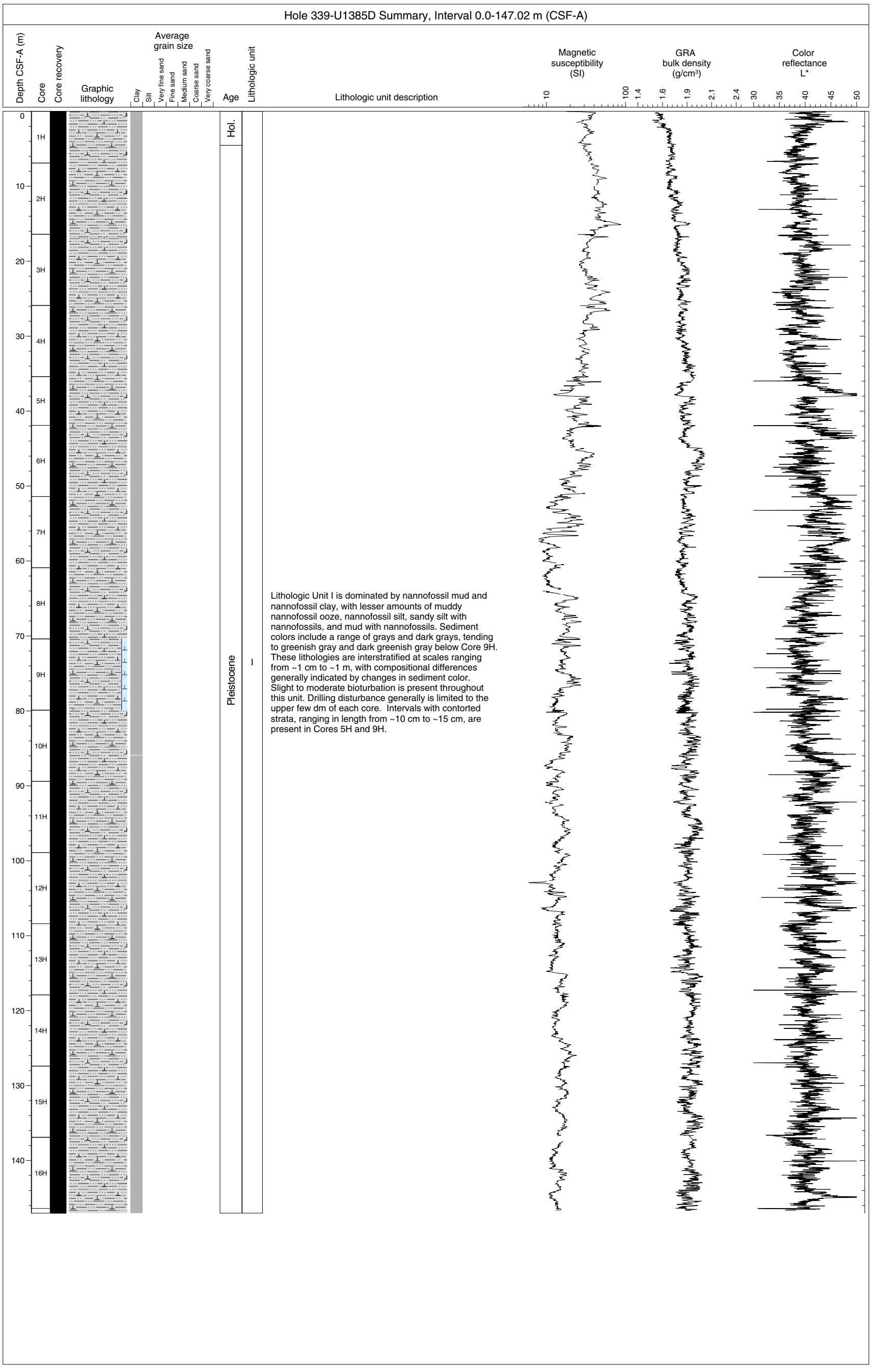

Figure F7 (continued). E. Hole U1385E.

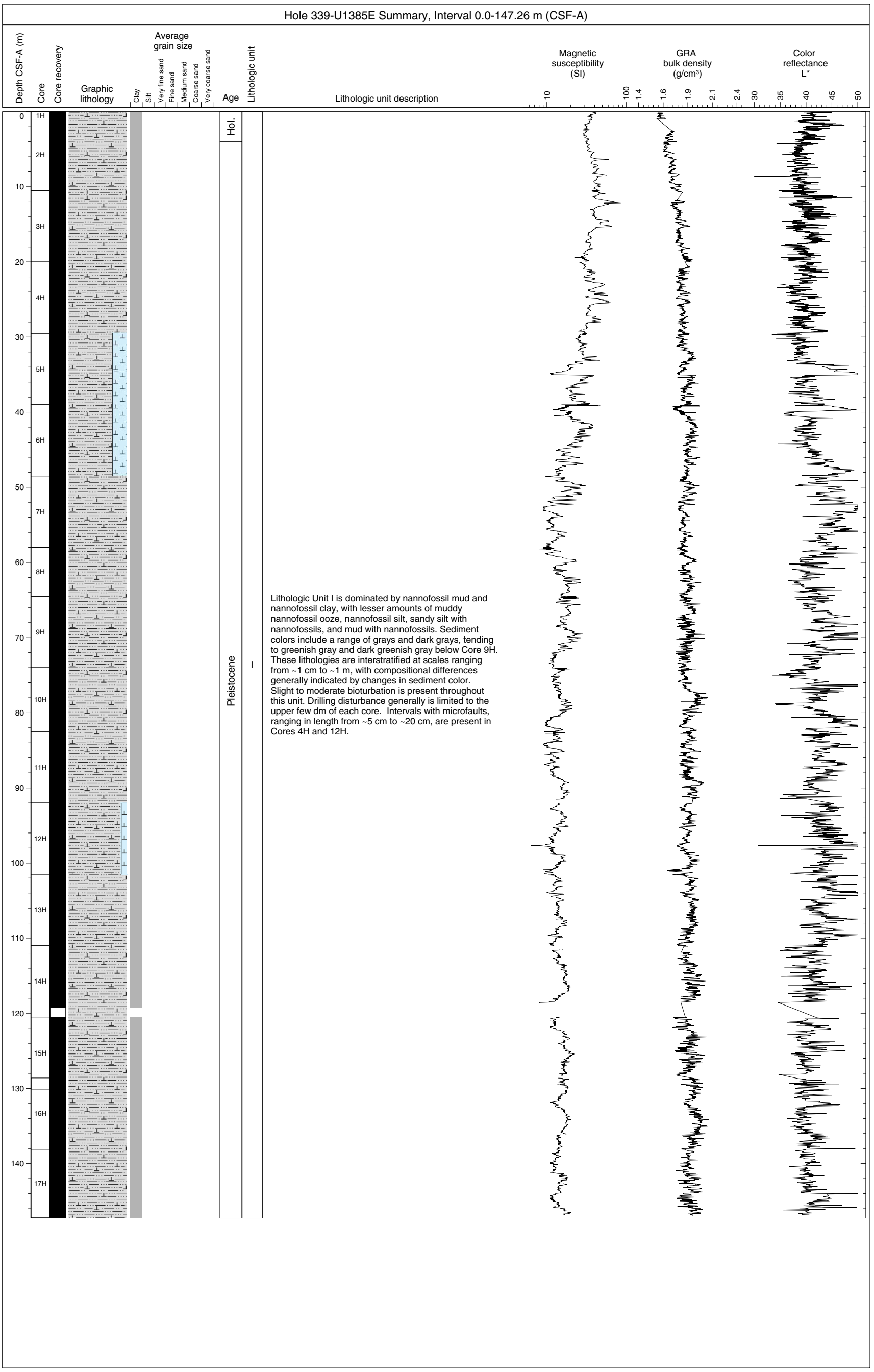

Figure F8. Photographs of pyrite nodule with embedded foraminifers (Sample 339-U1385D-12H-1, 96–97 cm).

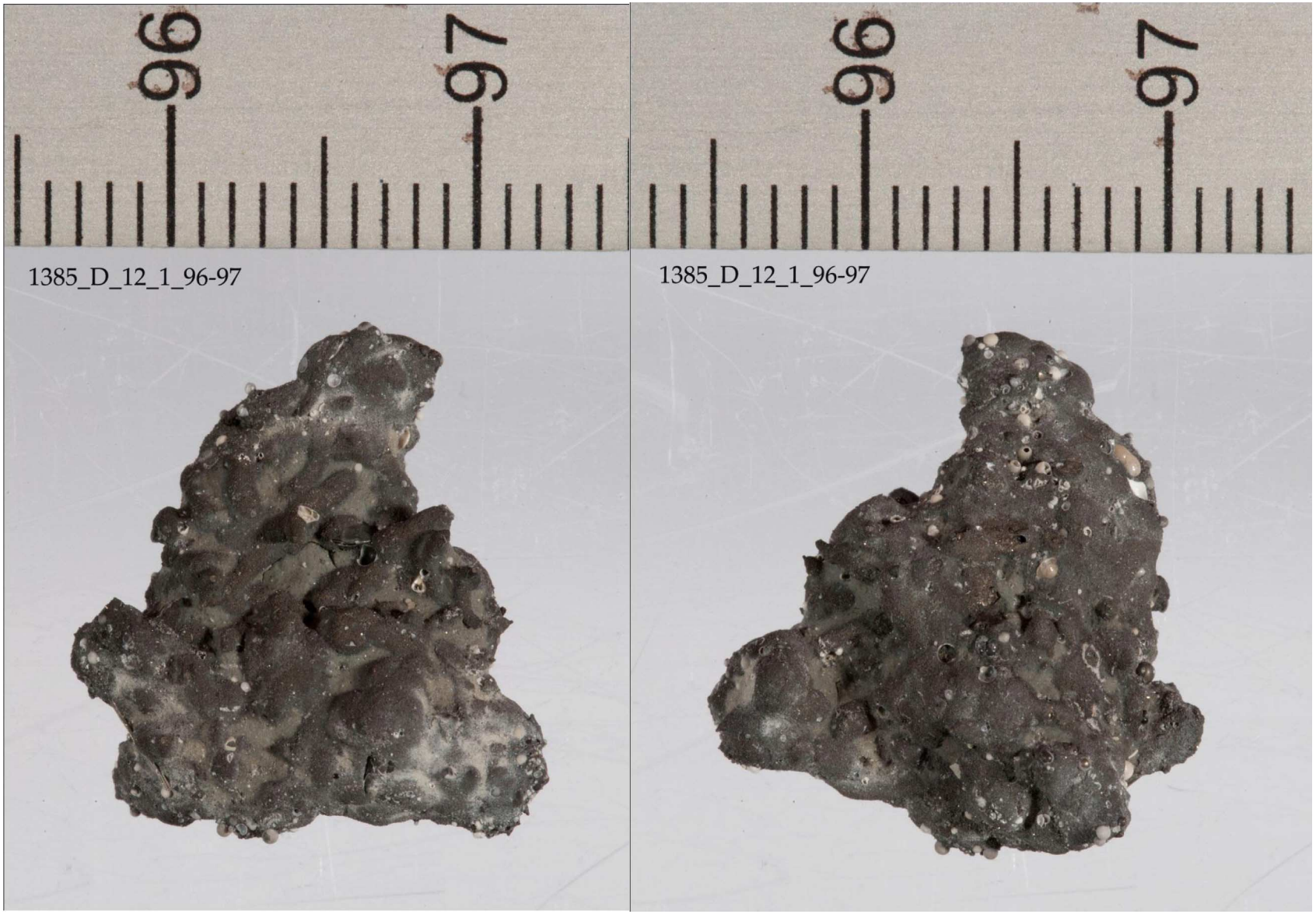

Figure F9. Core image of a vertical microfault displacing several large burrows (interval 339-U1385A-10H-3, 110–125 cm).

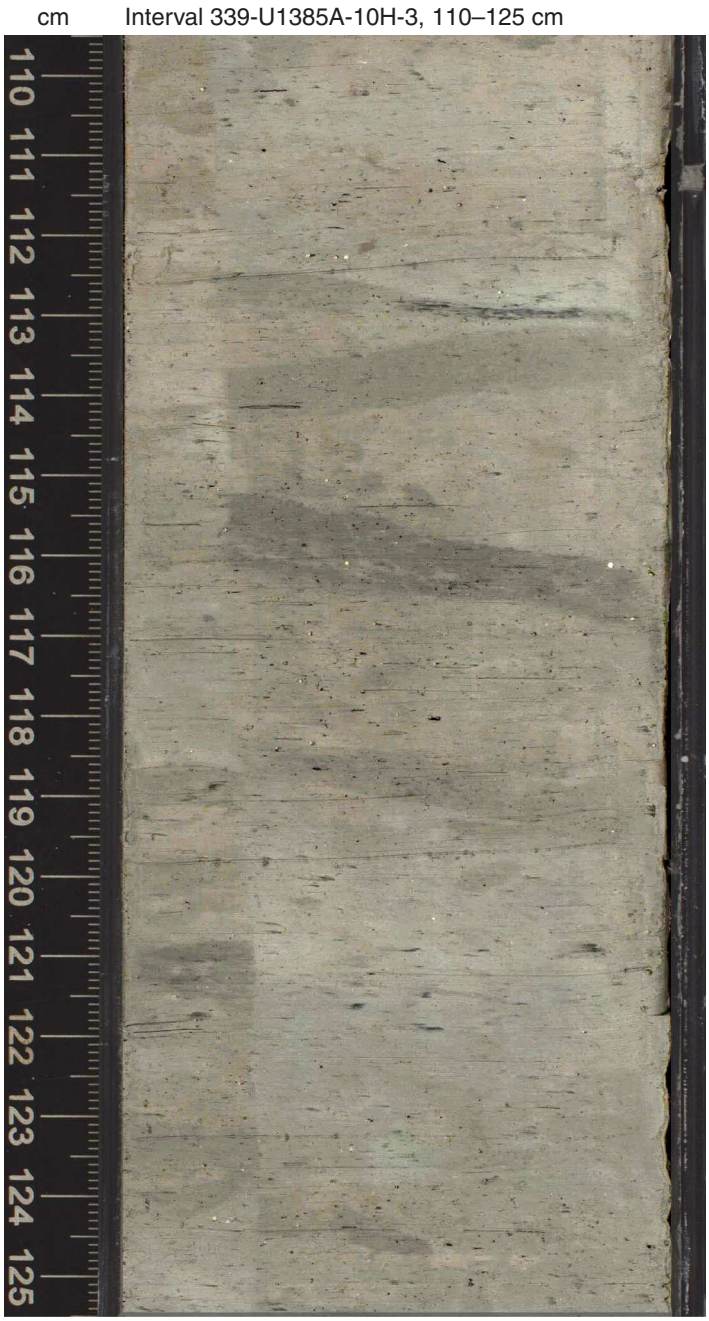

Figure F10. Photographs of a cold-water coral (Sample 339-U1385B-4H-2, 82 cm).

Figure F11. X-ray powder diffraction patterns from Holes U1385A and U1385B arranged with the shallowest sample at the top and the deepest sample at the bottom. The patterns are plotted with the intensity log to highlight the presence and nature of the smaller peaks. This figure shows that bulk mineralogy is nearly constant downhole, although minor changes occur in the intensities of the various peaks.

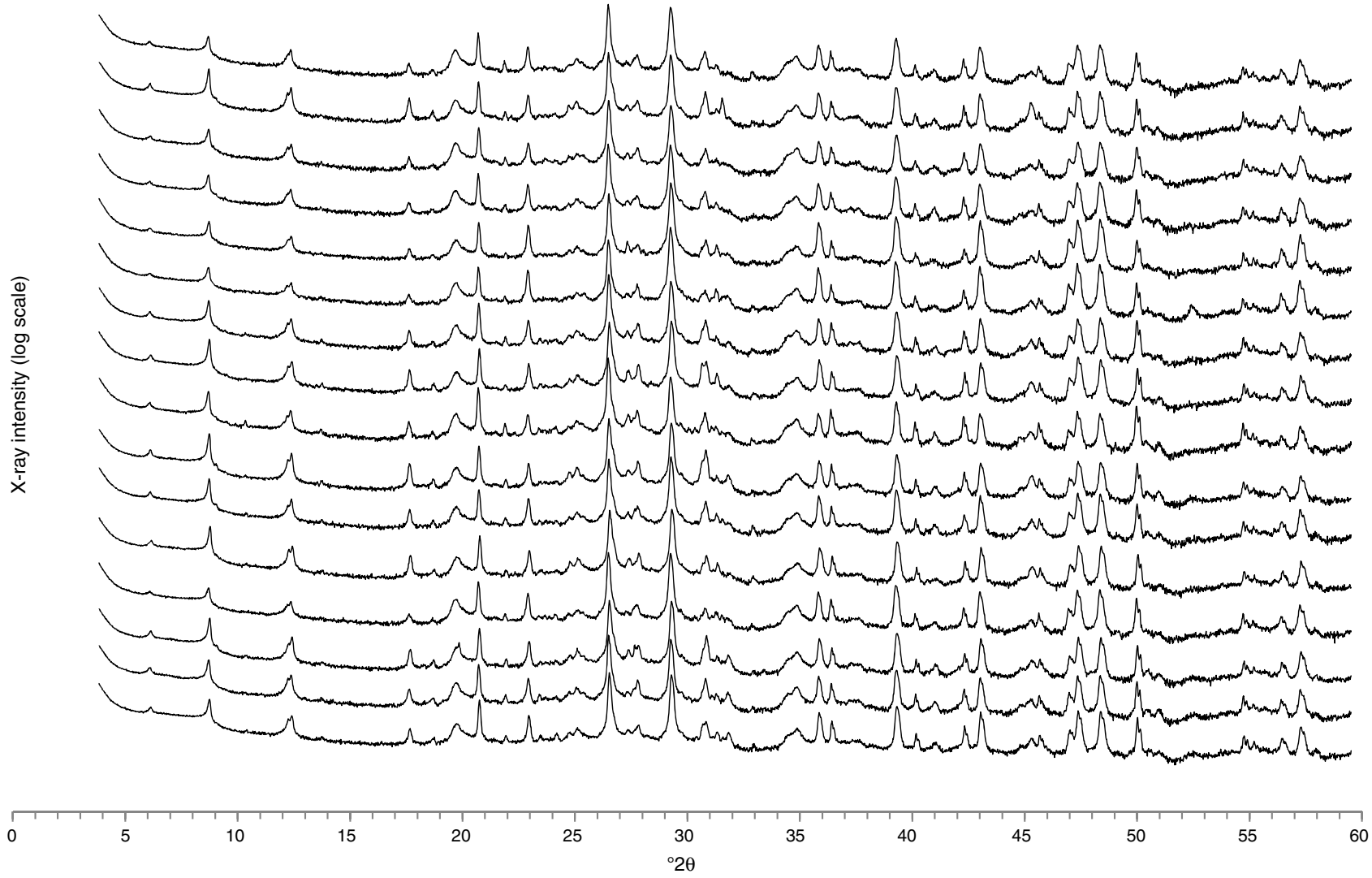

Figure F12. Superimposed X-ray powder diffraction patterns from 4° to 24°2θ, Site U1385. The scans show some minor variations in the baseline level from sample to sample, perhaps caused by variations in the packing of the sample holders, and a constant value was added or subtracted from each scan to make the scans line up better. Superimposing the scans in this fashion shows variation in X-ray intensity in the region from ~4° to 8°2θ, which may be caused by the presence of poorly crystalline clay material.

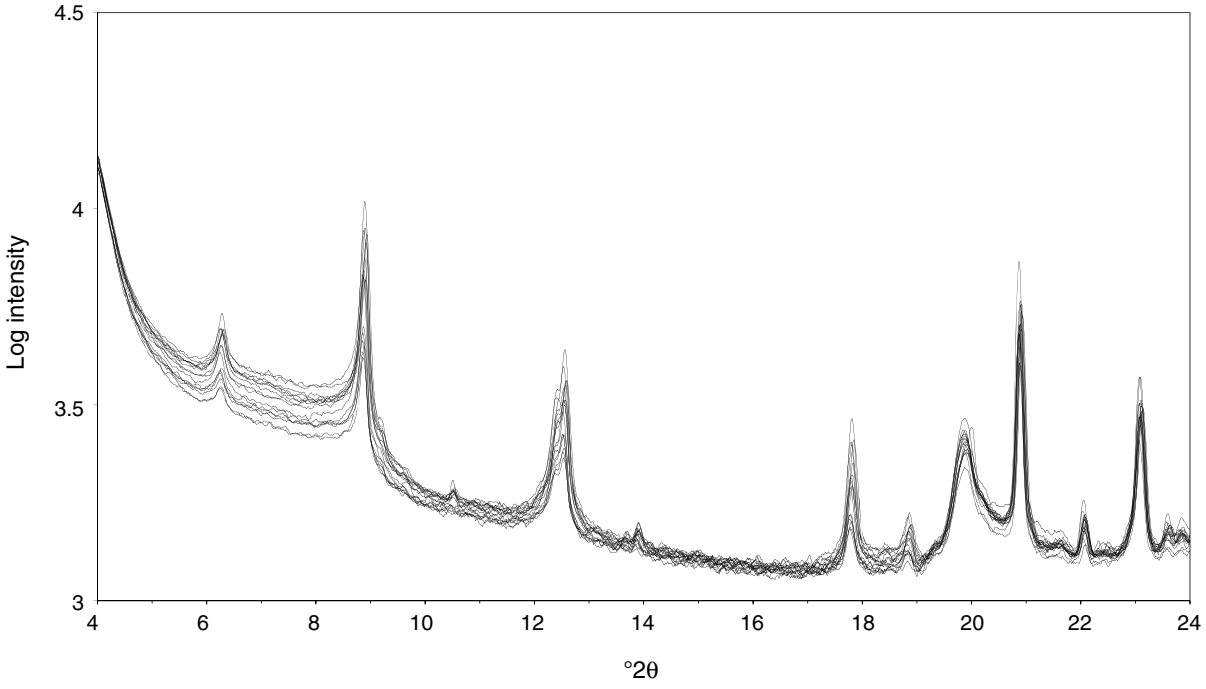

Figure F13. Scatter plot of X-ray intensity at 7°2θ plotted downhole, Site U1385. Note a general trend in increased intensity with increasing depth.

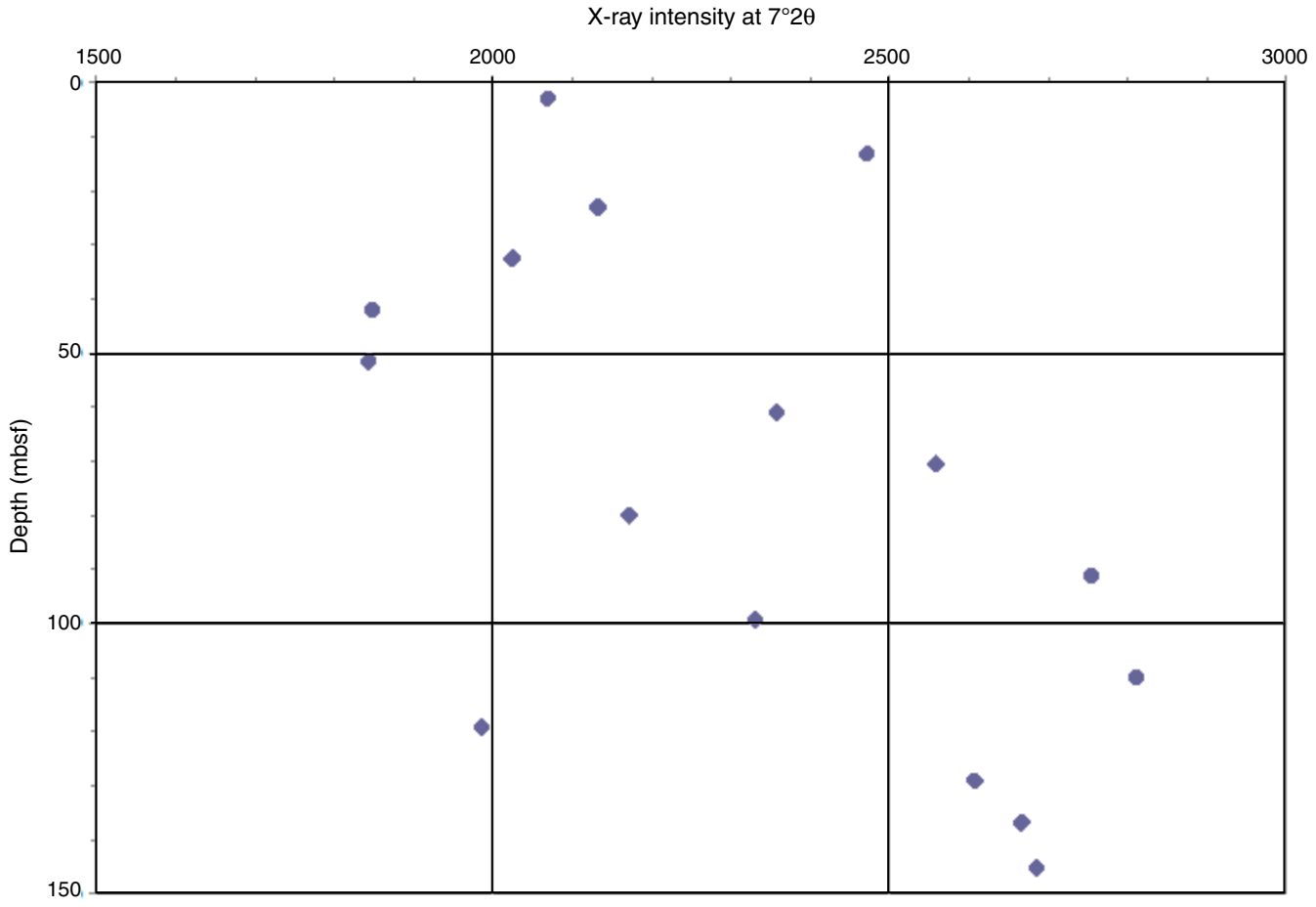

Figure F14. Superimposed glycolated powder XRD patterns from 4° to 24°2θ, Site U1385. X-ray intensity from ~7° to 8°2θ was reduced and intensity from ~5°2θ increased compared with the untreated material (Fig. F12), which is consistent with the presence of poorly crystalline clay material.

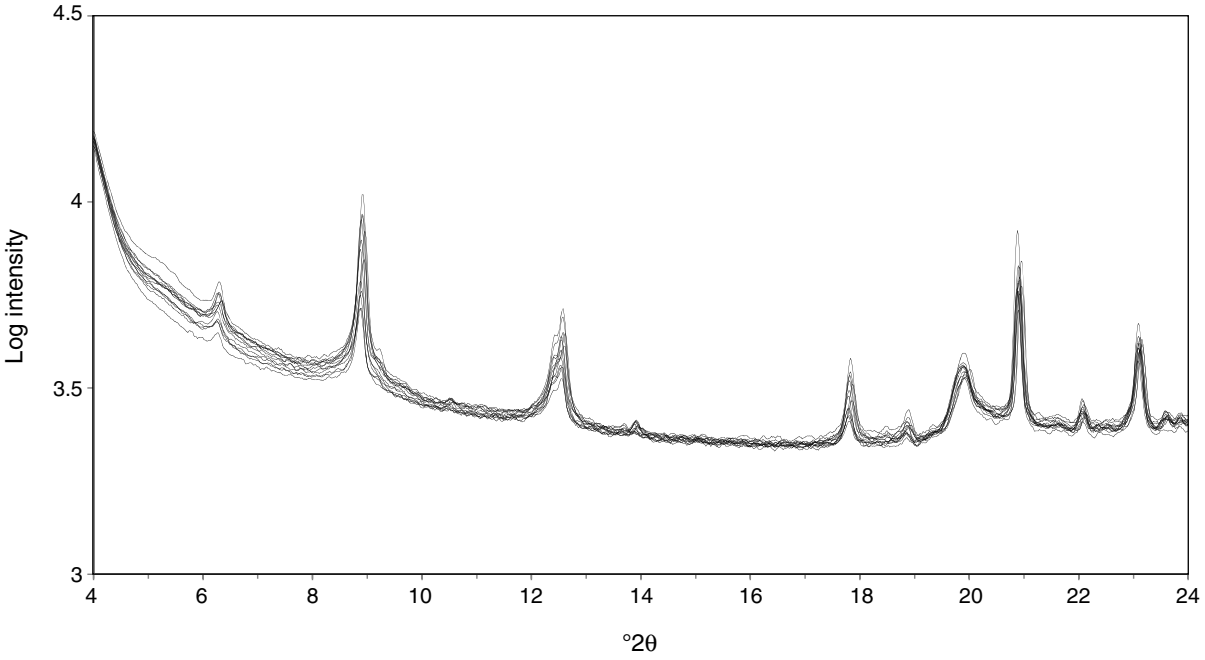

Figure F15. Downhole profile of the decrease in X-ray intensity at 7.65°2θ as a result of sample glycolation, Holes U1385A and U1385B. The profile suggests that relative abundances of smectite or smectite-bearing mixed-layer clays generally increases downhole.

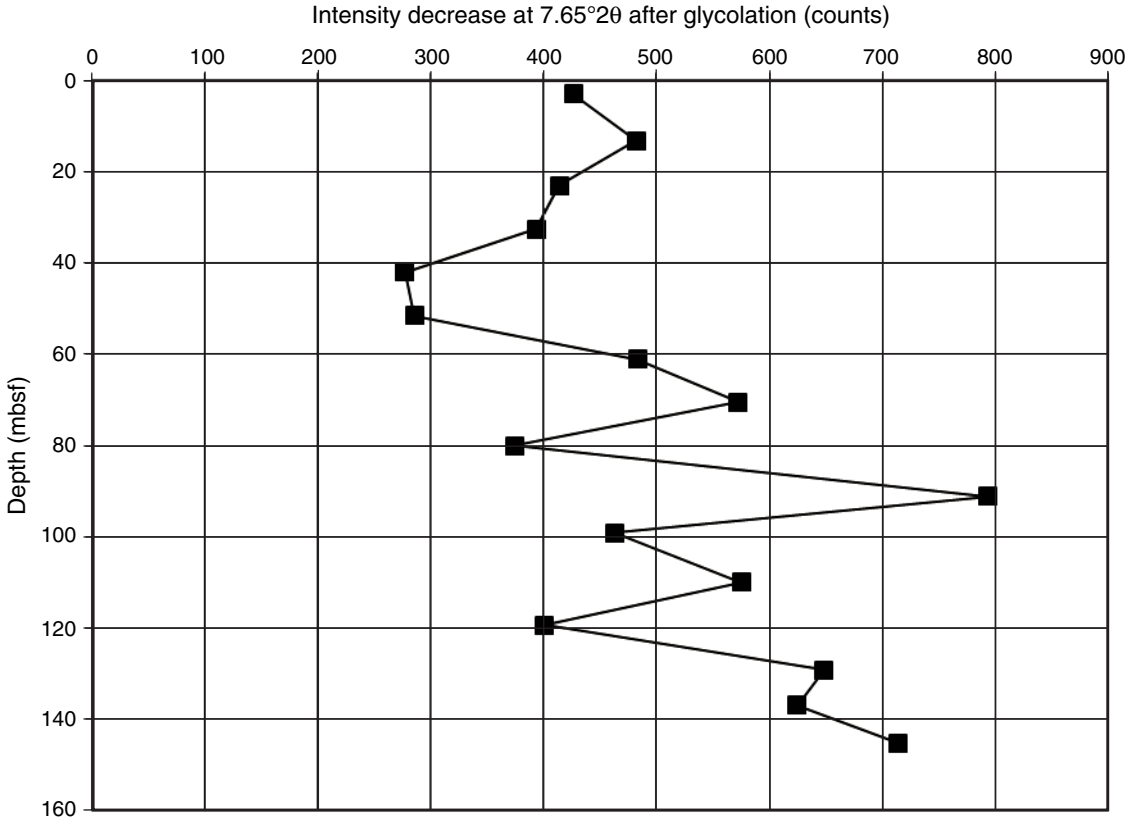

Figure F16. Biostratigraphic events vs. depth, Site U1385. Events are plotted at their mean depth (see Table T7).

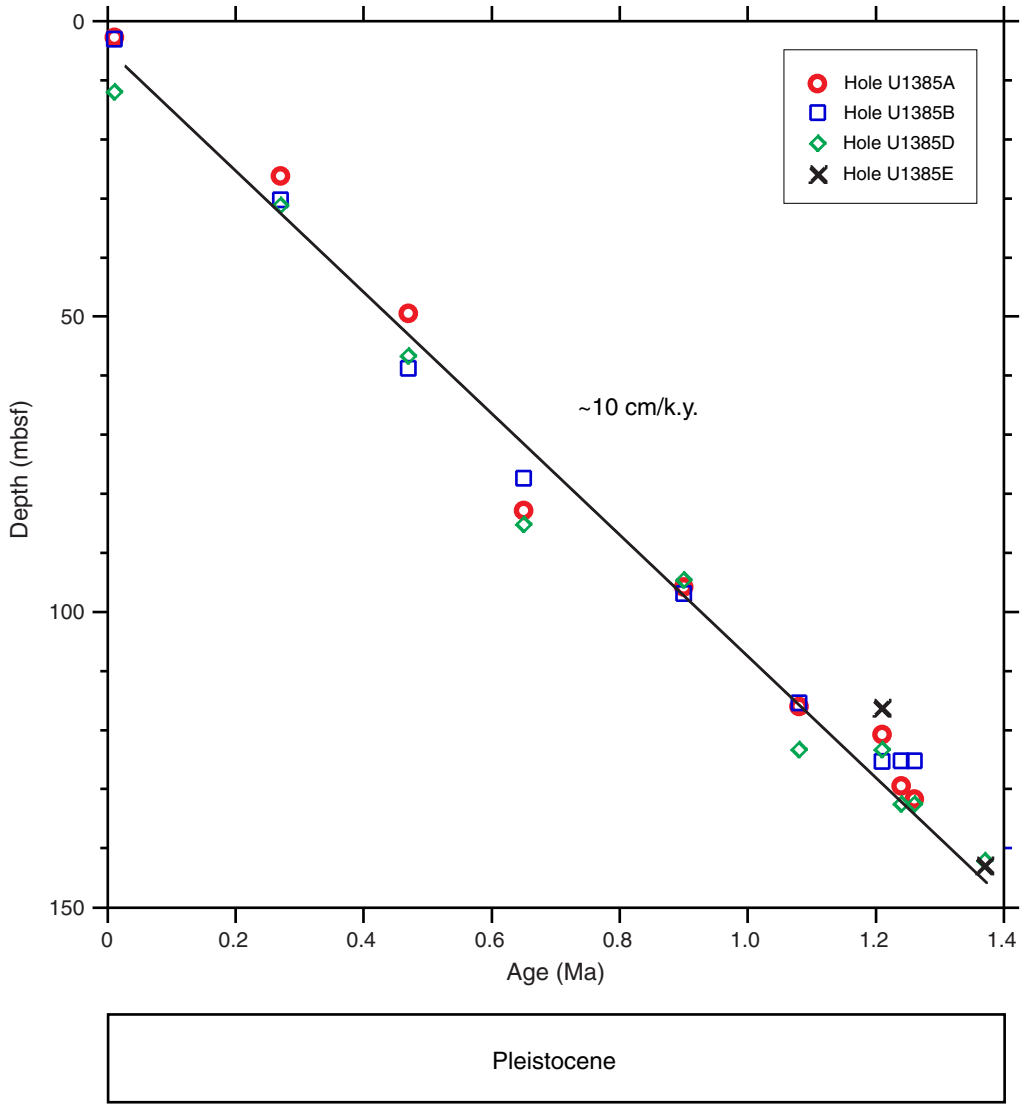

Figure F17. Preliminary pollen results from the analysis of nine samples from Hole U1385A. Mediterranean forest is mainly deciduous and evergreen with *Quercus, Olea,* and *Phillyrea*. Heathland is represented by Ericaceae. Inset photo (1000×) shows dinocyst species *Stelladinium* cf. *reidii,* ~60 µm in size, which is abundant in Sample 339-U1385A-11H-CC. Preservation: G = good, M = moderate, P = poor.

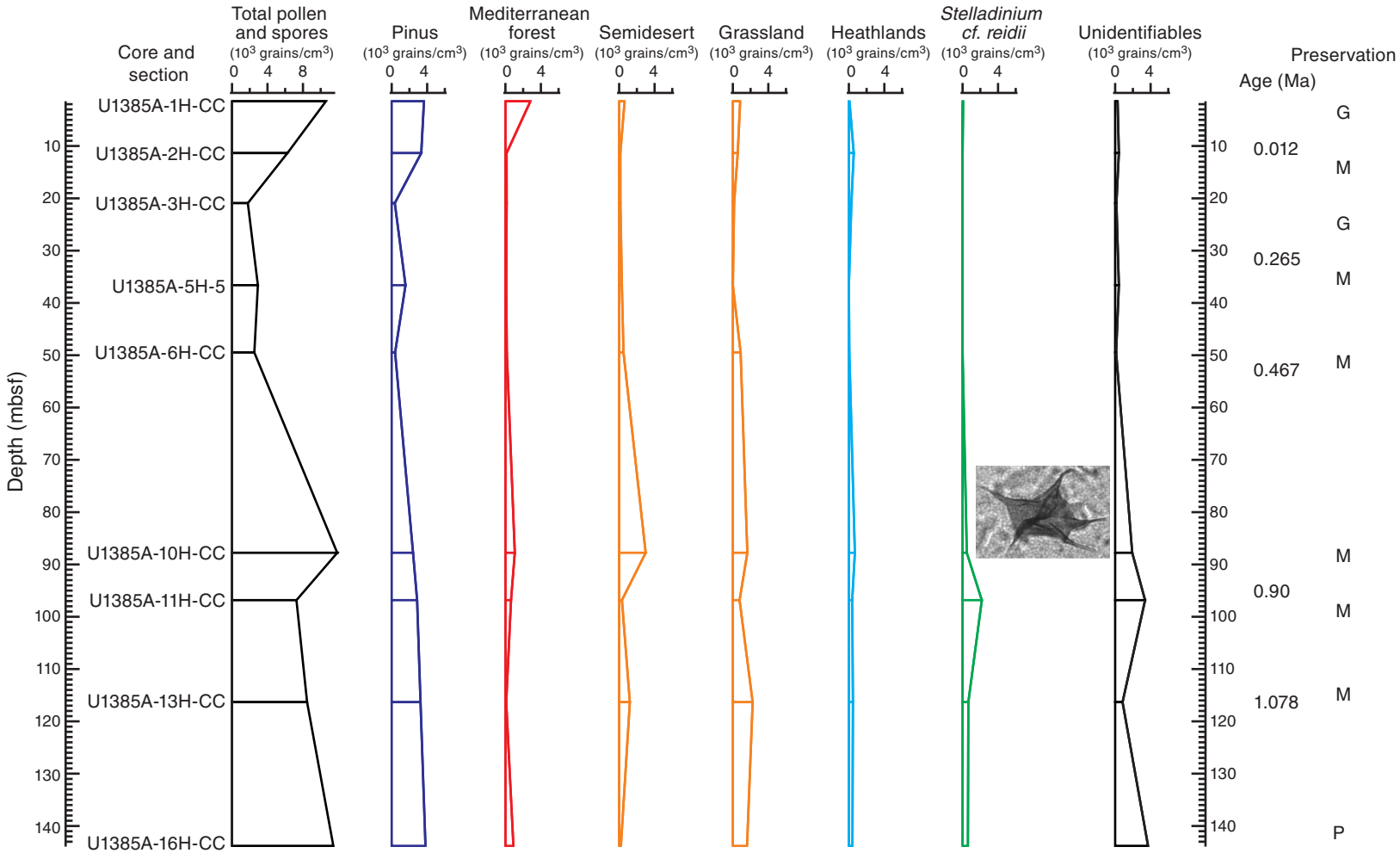

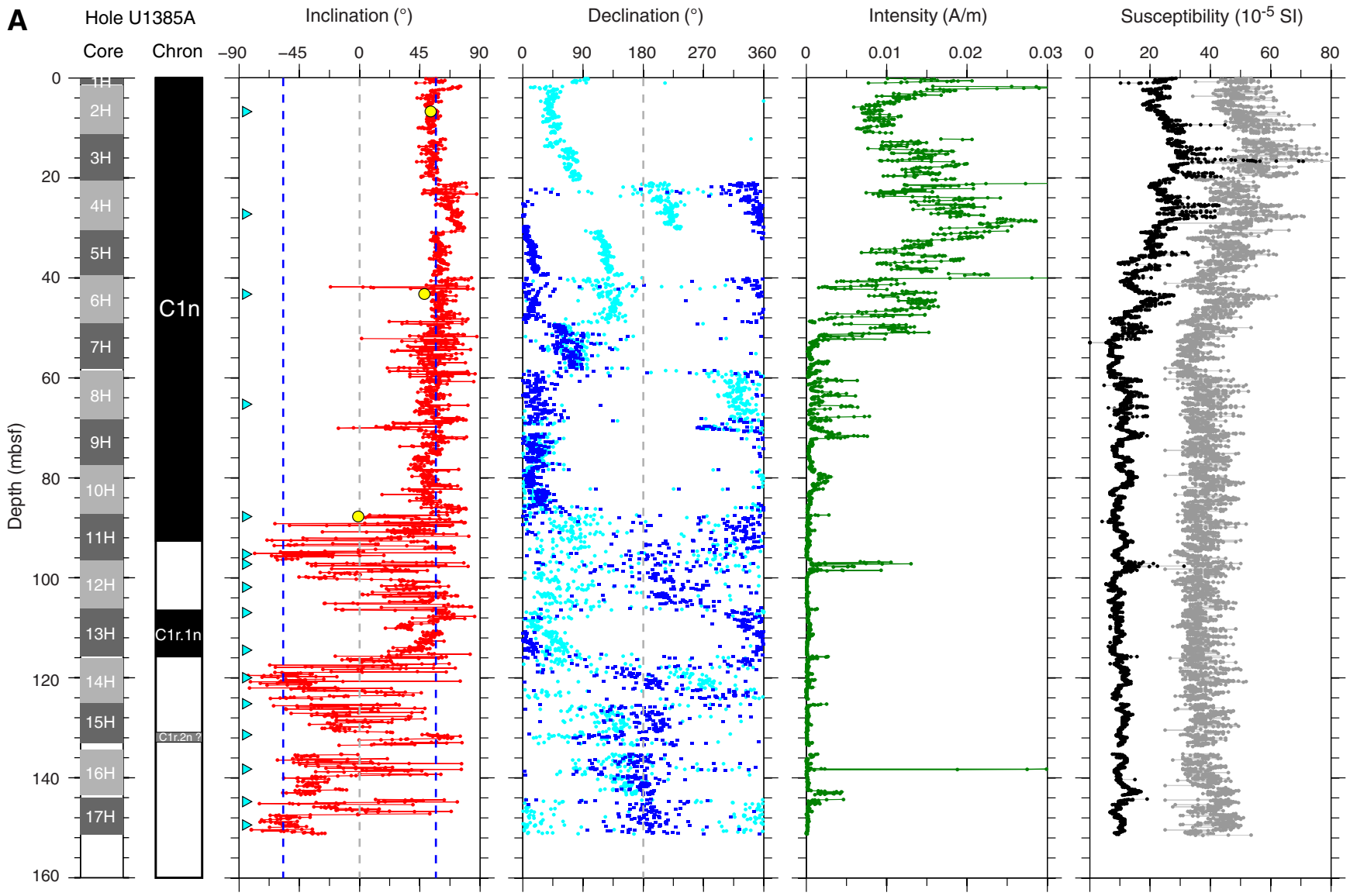

Figure F18. A–E. Paleomagnetism after 20 mT peak field AF demagnetization, Site U1385. Blue triangles = discrete sample locations. Yellow circles = component inclinations of discrete samples with maximum angular deviation less than ~15°. In Chron columns, black = normal polarity, white = reversed polarity, and gray = zones of possibly normal polarity (Cobb Mountain Subchron). In Inclination columns, blue dashed lines = expected GAD inclinations at the site latitude during reversed (left) and normal (right) polarities. In Declination columns, light blue circles = original declinations and dark blue squares = FlexIt tool–corrected declinations. In Susceptibility columns, gray lines represent SHMSL susceptibility plus 25 × 10^{-5} volume SI to better show the comparison with WRMSL susceptibility (black lines). **A.** Hole U1385A. (Continued on next four pages.)

Figure F18 (continued). B. Hole U1385B. (Caption shown on previous page.)

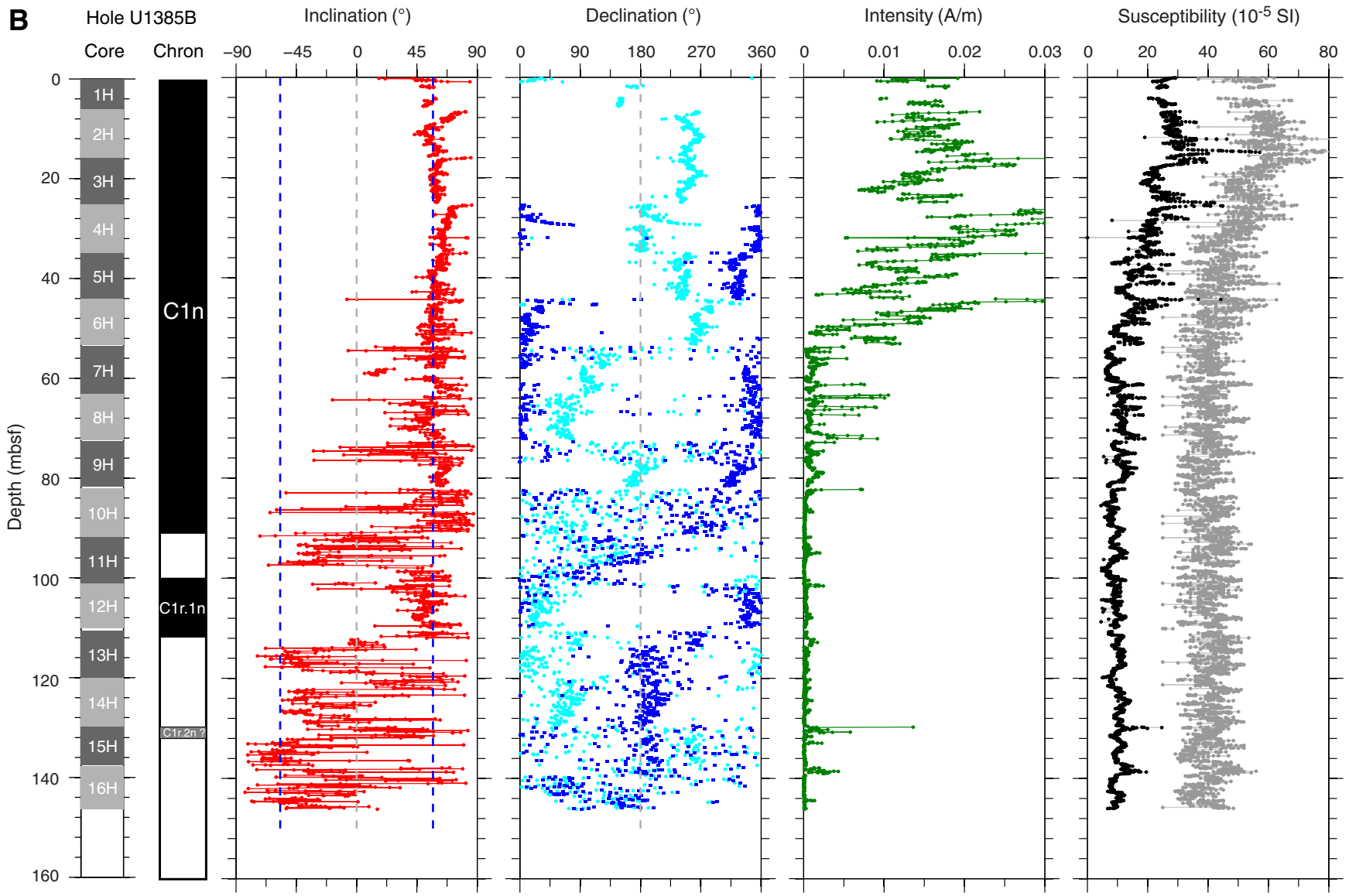

Figure F18 (continued). C. Hole U1385C. (Continued on next page.)

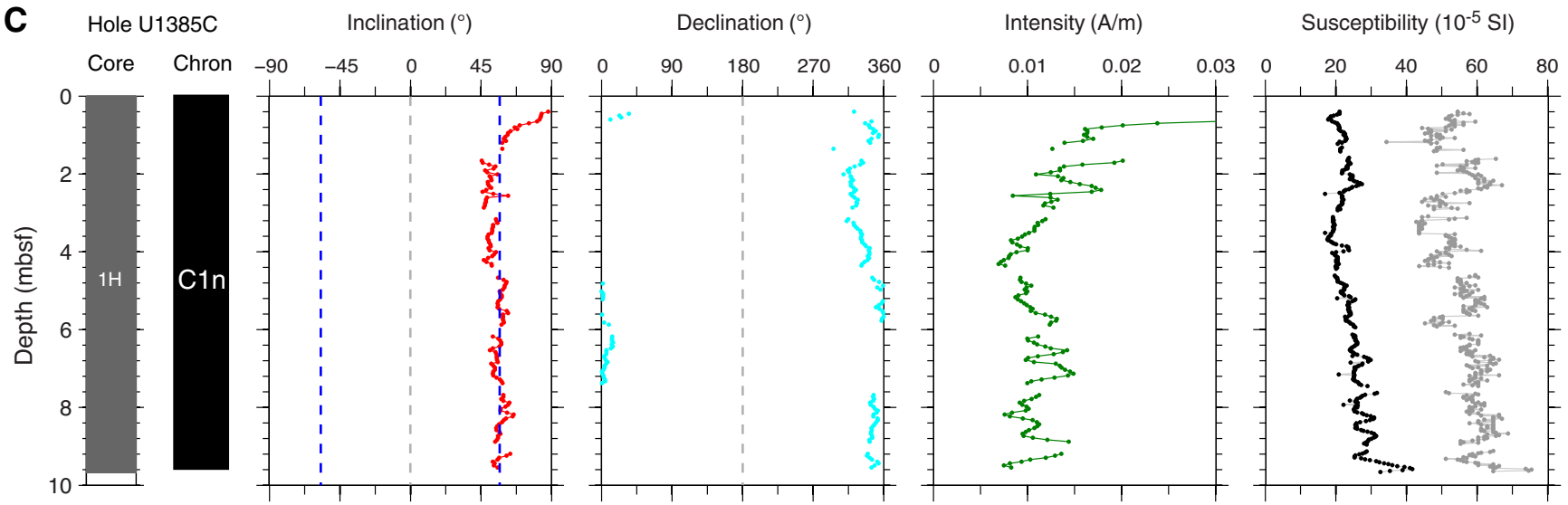

Figure F18 (continued). D. Hole U1385D. (Continued on next page.)

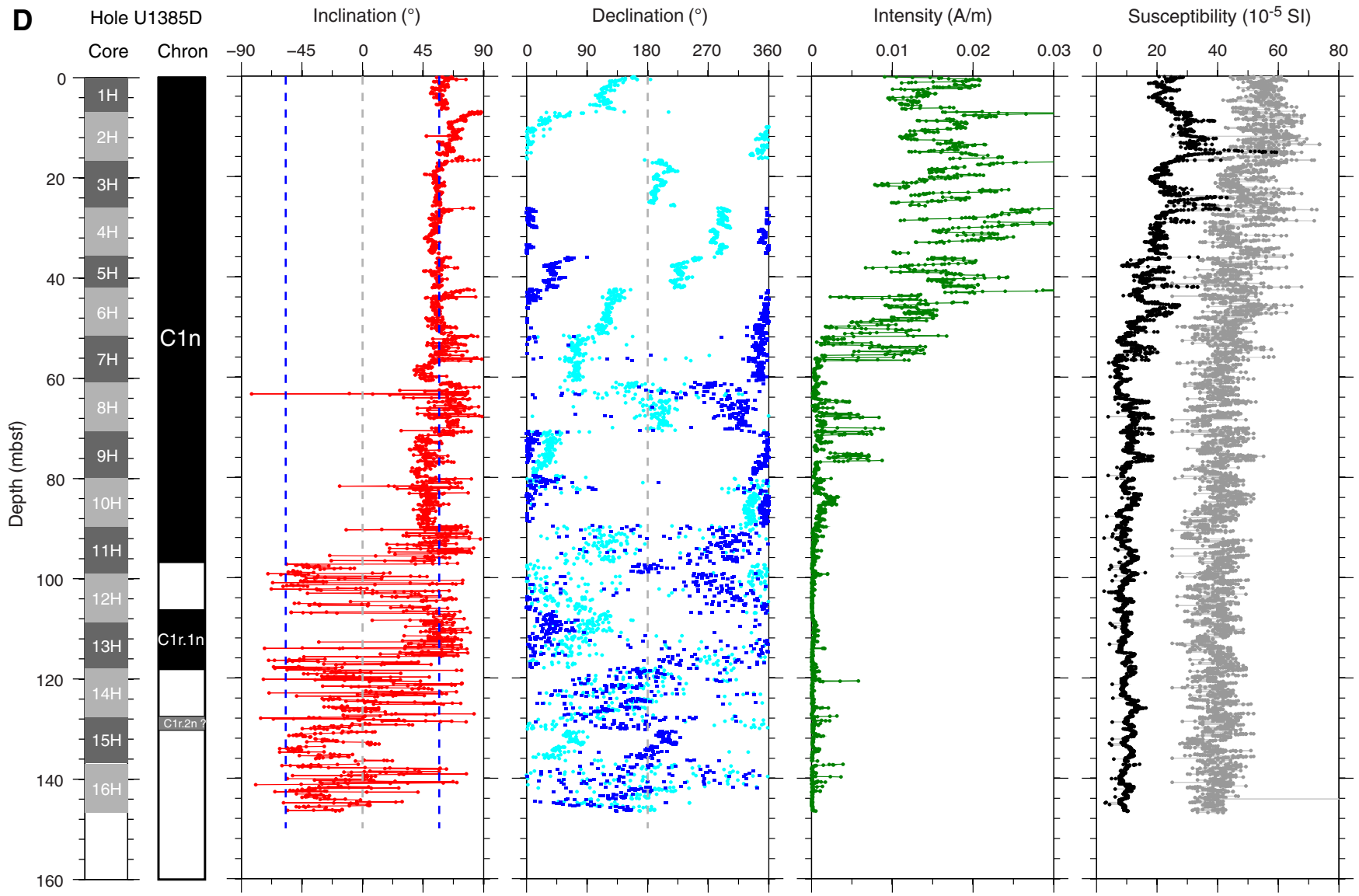

Figure F18 (continued). E. Hole U1385E.

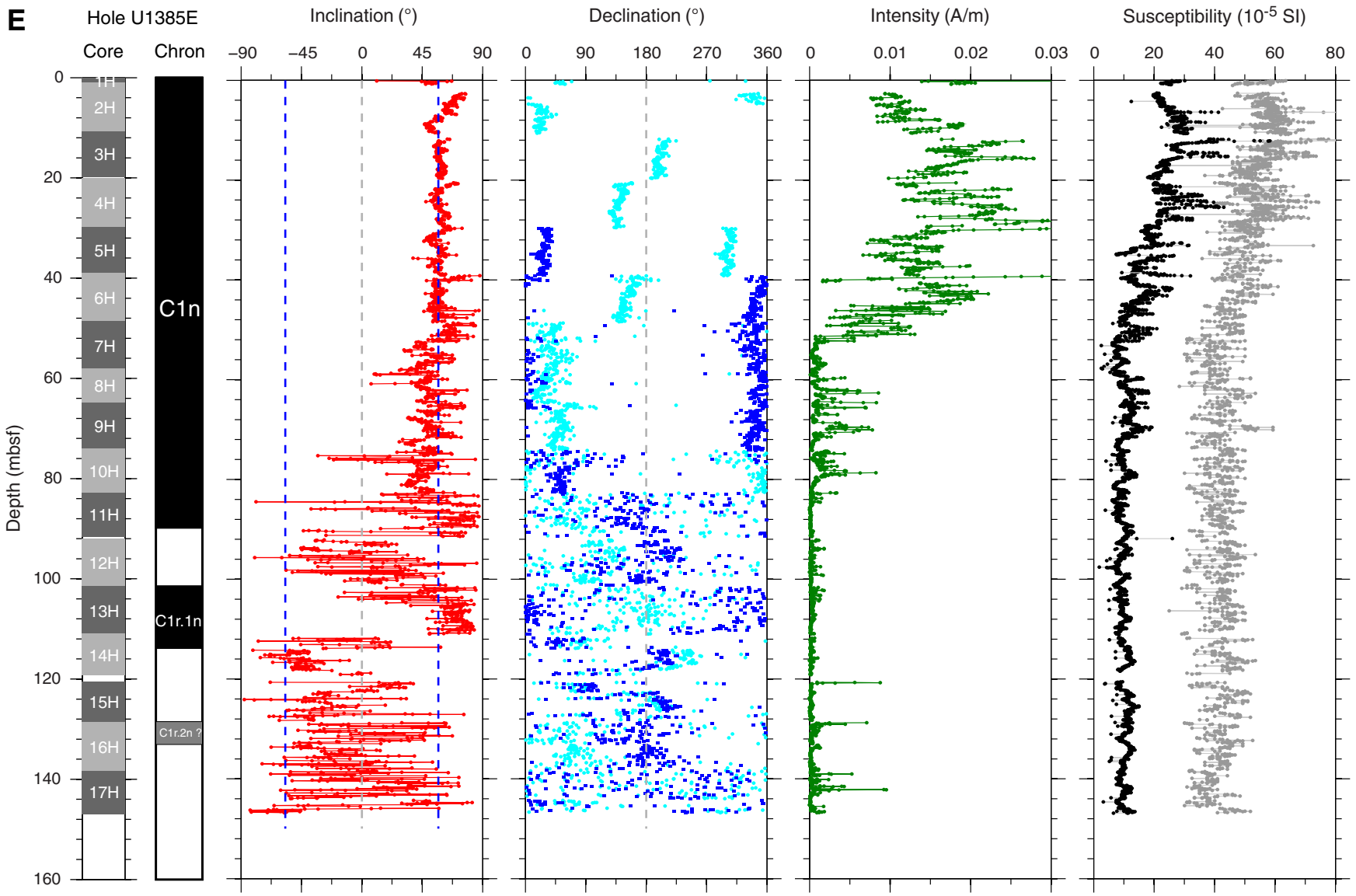

Figure F19. A–D. AF demagnetization results for four discrete samples, Hole U1385A. For each sample, the right plot shows the vector endpoints of paleomagnetic directions measured after each demagnetization treatment on an orthogonal projection (Zijderveld) plot. Squares = horizontal projections, circles = vertical projections. The left plot shows the intensity variation with progressive demagnetization. Orthogonal projection plots in A and B illustrate the removal of a steep drilling overprint by ~15–20 mT peak field AF demagnetization, with the remaining magnetization providing a well-resolved characteristic remanent magnetization. The weakly magnetized samples from below 50 mbsf (C and D) exhibit erratic behavior during demagnetization without a stable magnetic component.

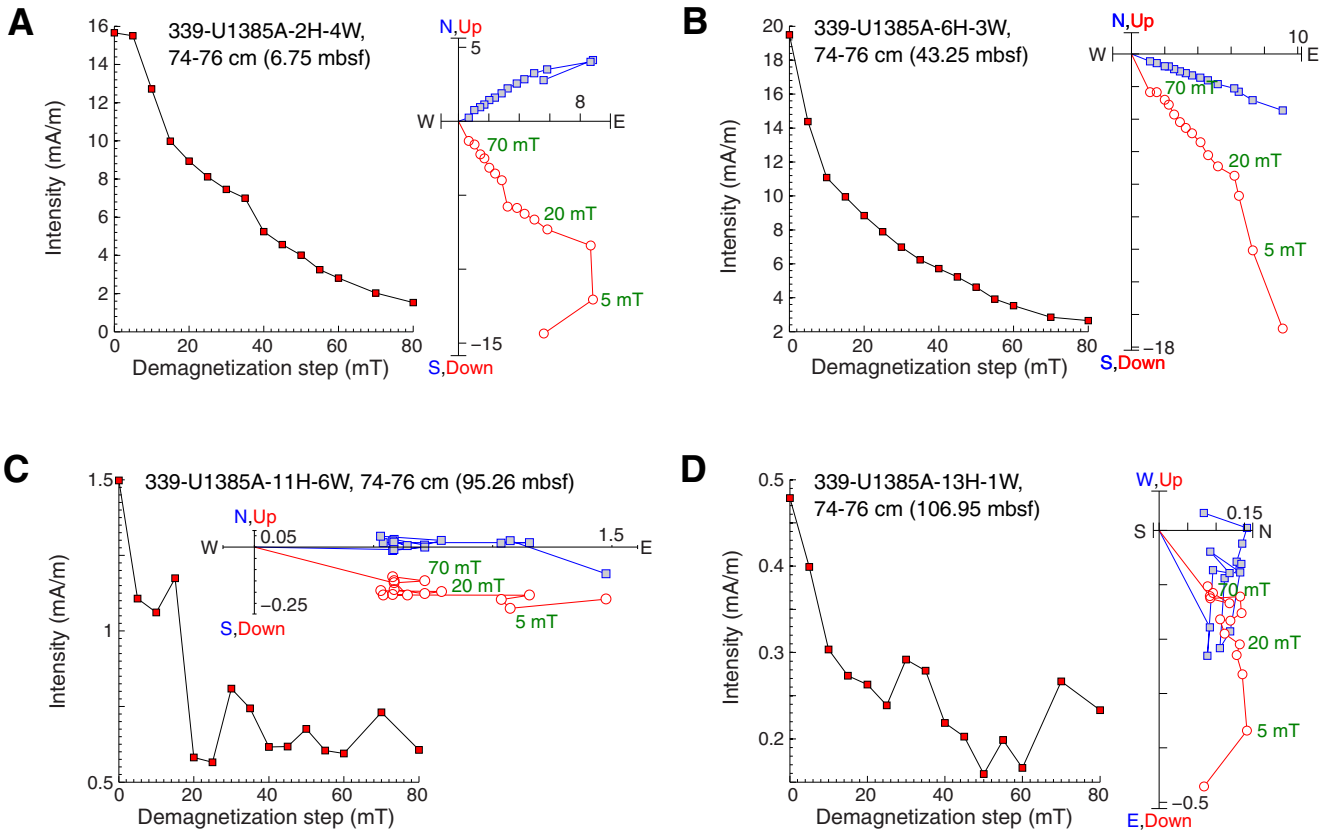

Figure F20. *P*-wave velocity and density logs, Site U1385. PWC auto = *P*-wave caliper (discrete samples) on automatic setting, PWC manual = *P*-wave caliper (discrete samples) on manual setting, PWL = *P*-wave logger on Whole Round Multisensor Logger (WRMSL), MAD = wet bulk moisture and density (discrete samples), GRA = gamma ray attenuation bulk density, STMSL = Special Task Multisensor Logger.

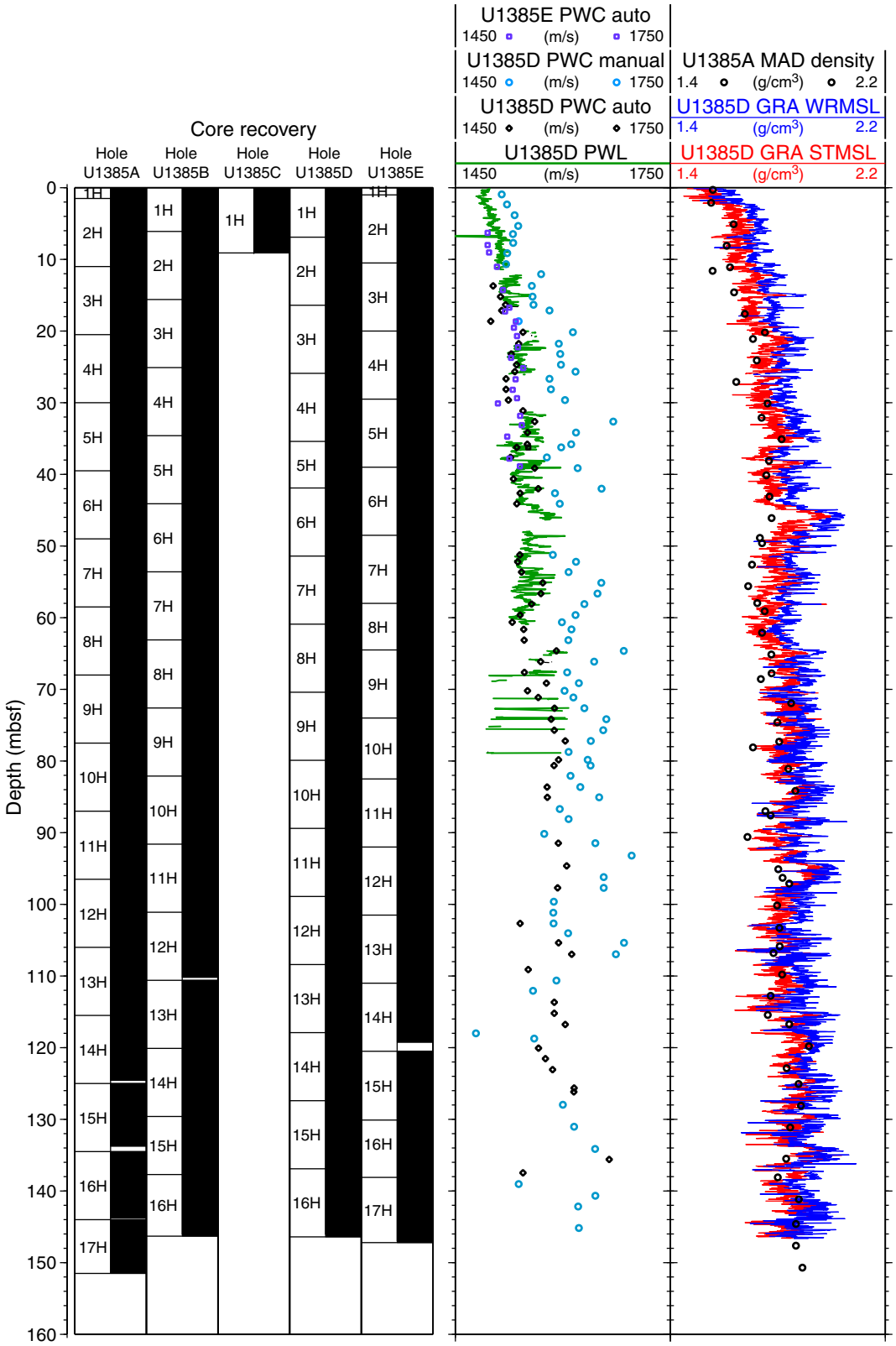

Figure F21. Plot of Whole-Round Multisensor Logger magnetic susceptibility measurements, Hole U1385A.

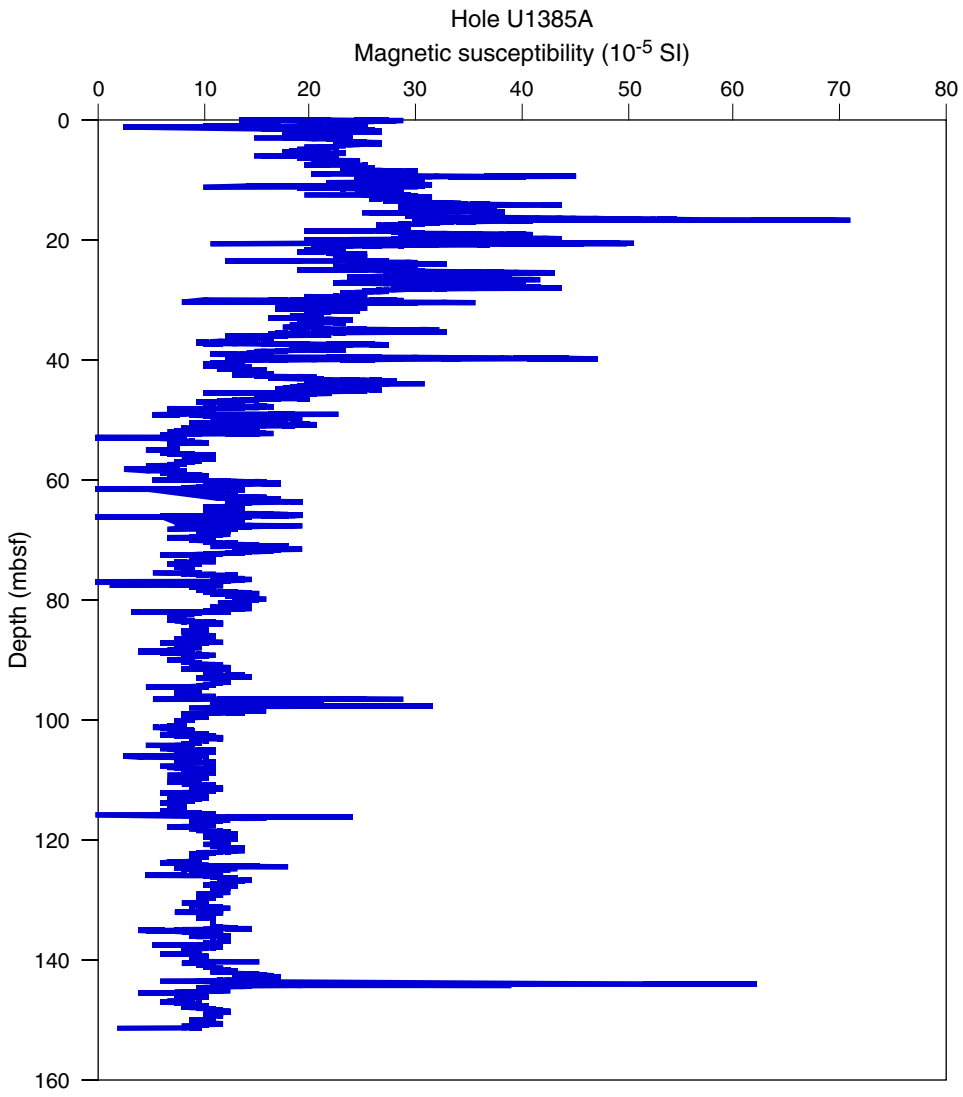

Figure F22. Plots of color reflectance (L*, a*) and natural gamma ray (NGR) measurements, Hole U1385A.

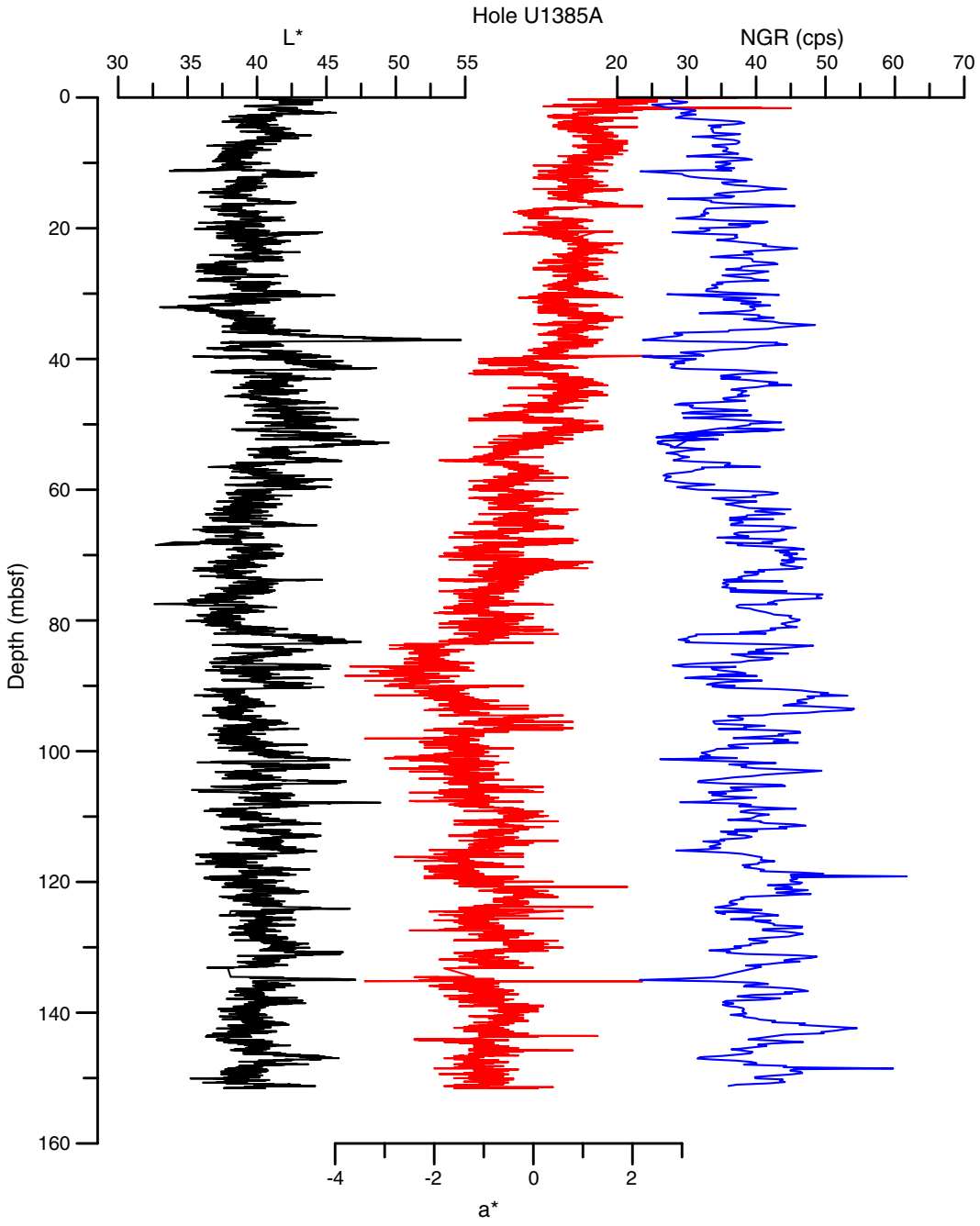

Figure F23. Plots of wet bulk and dry density from discrete measurements, Hole U1385A.

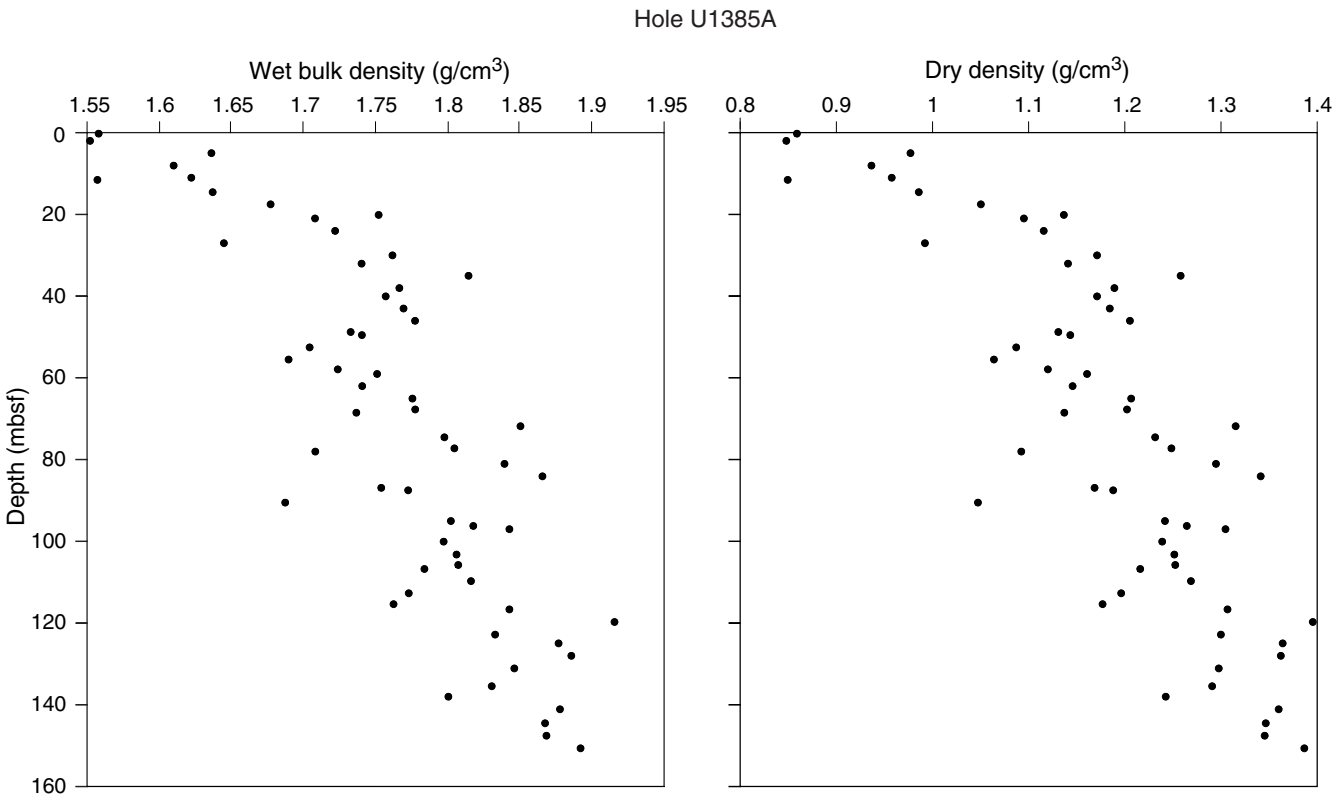

Figure F24. Plots of moisture content and grain density from discrete sample measurements, Hole U1385A.

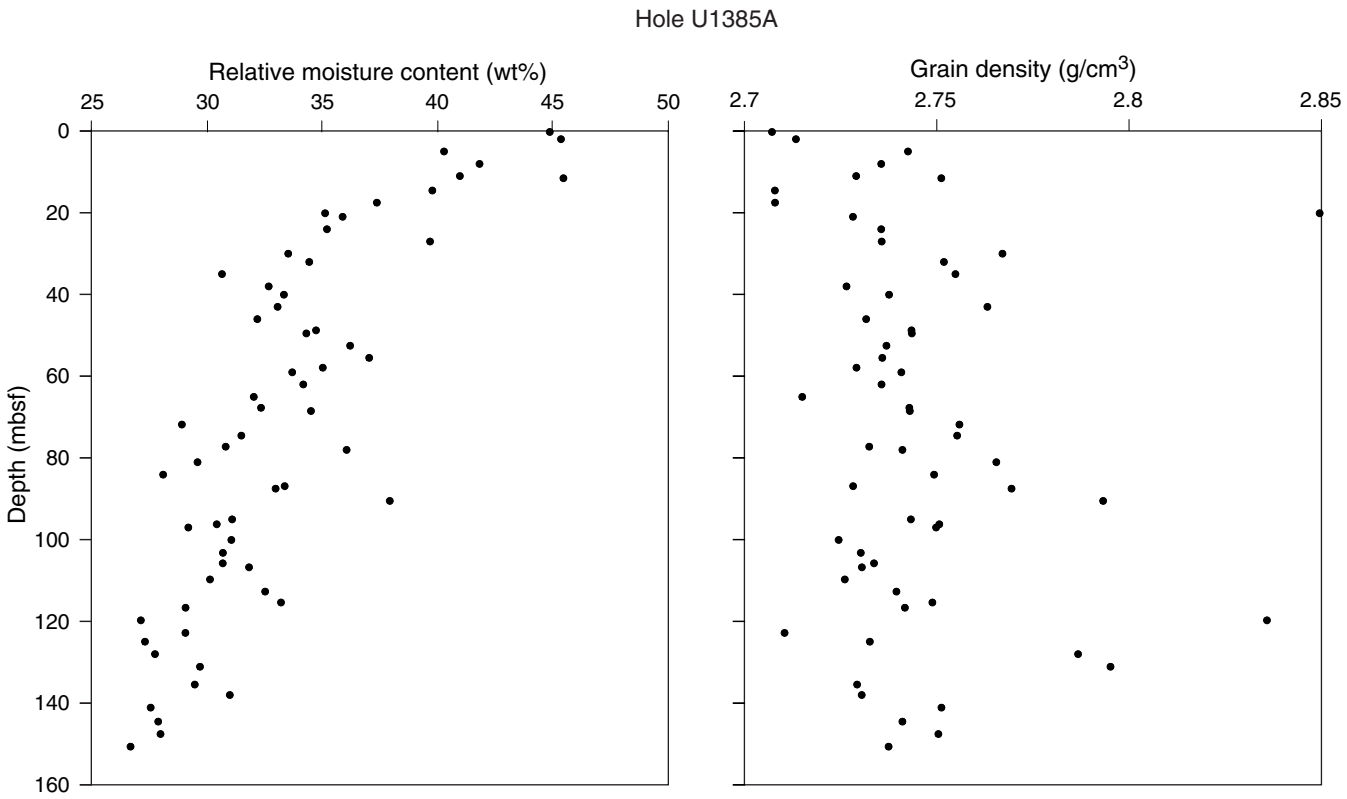

Figure F25. Plot of headspace gas analyses for volatile hydrocarbons, Hole U1385A.

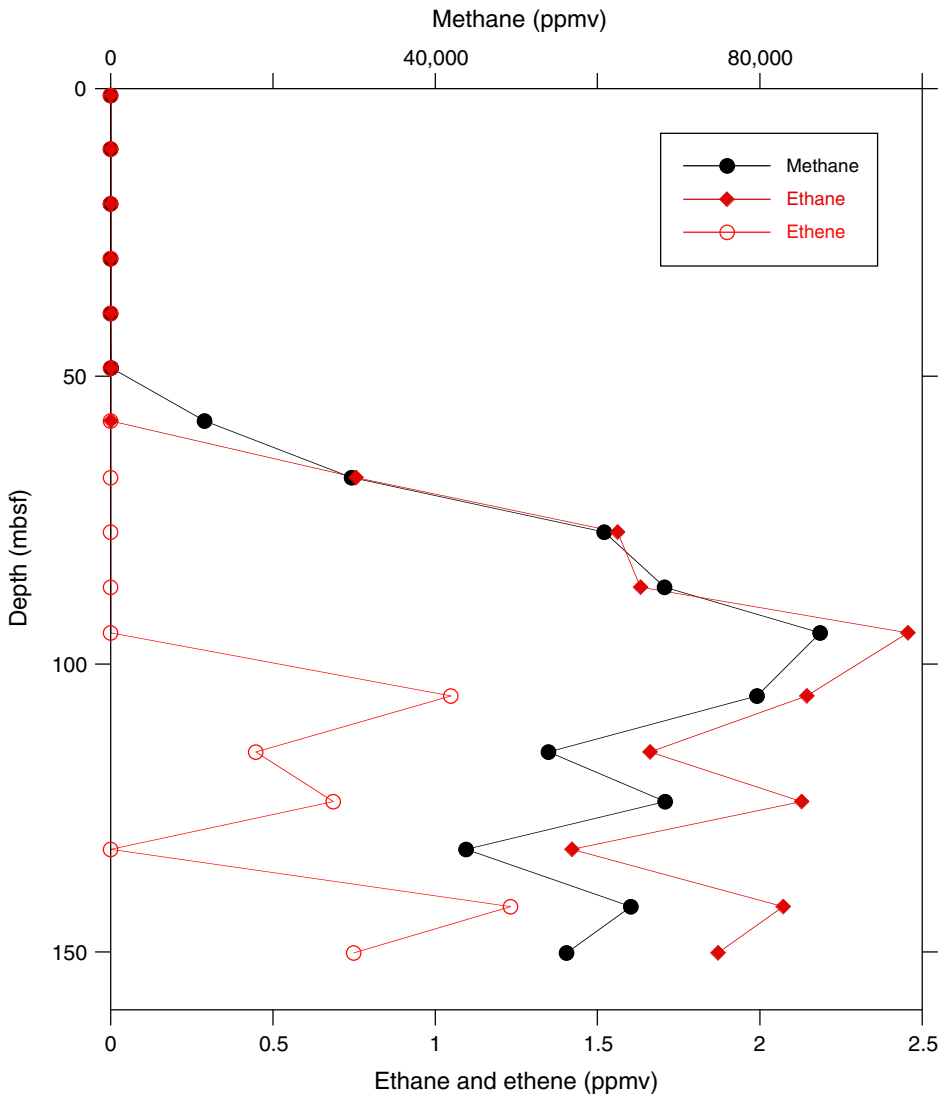

Figure F26. Plots of calculated total organic carbon (TOC), total nitrogen (TN), and C/N ratio, Hole U1385B.

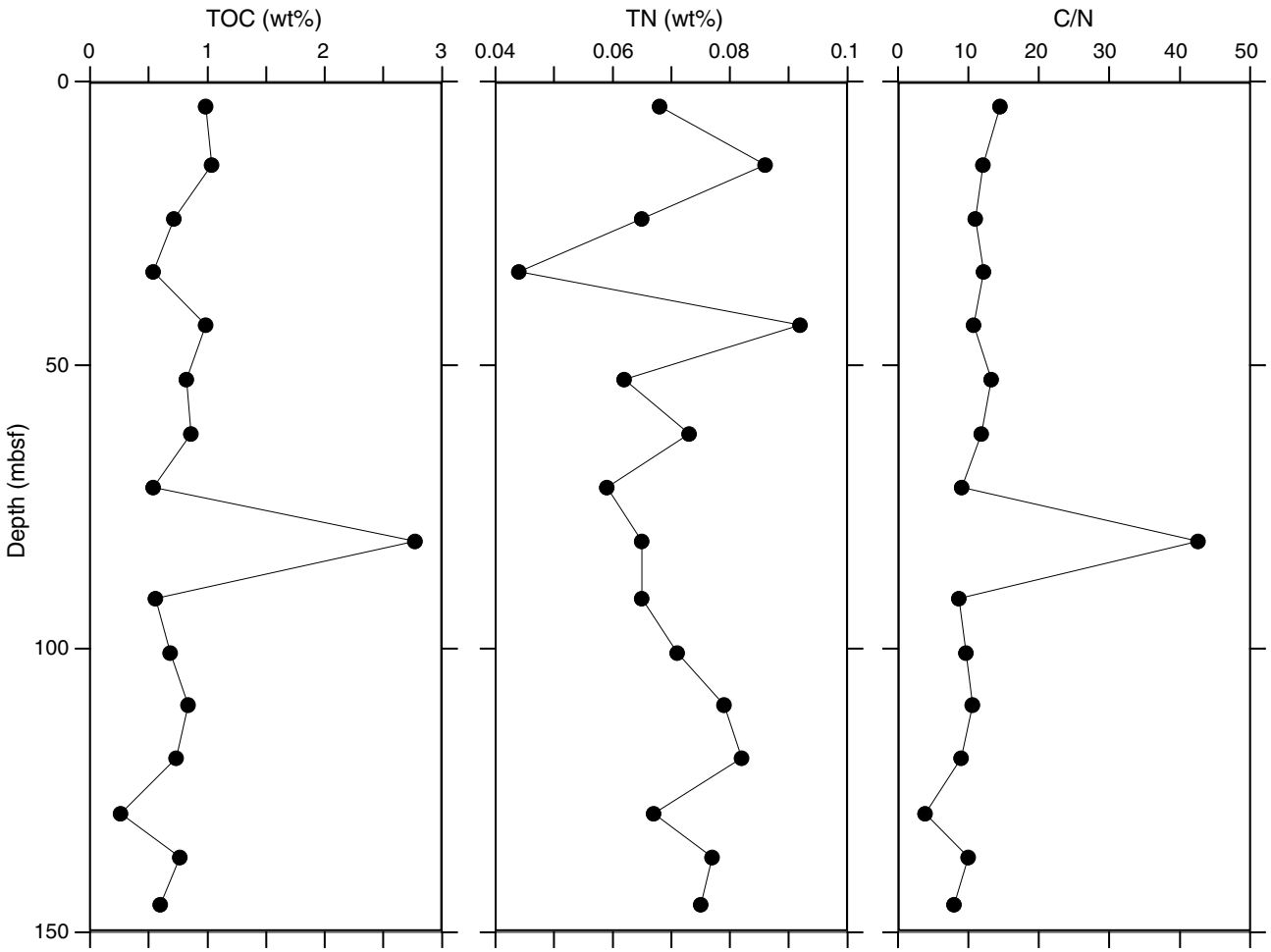

Figure F27. Plots of (**A–C**) interstitial water sulfate, alkalinity, and ammonium in Hole U1385B and (**D**) hydrocarbons in Hole U1385A (open circles = methane, solid circles = ethane, diamonds = ethene).

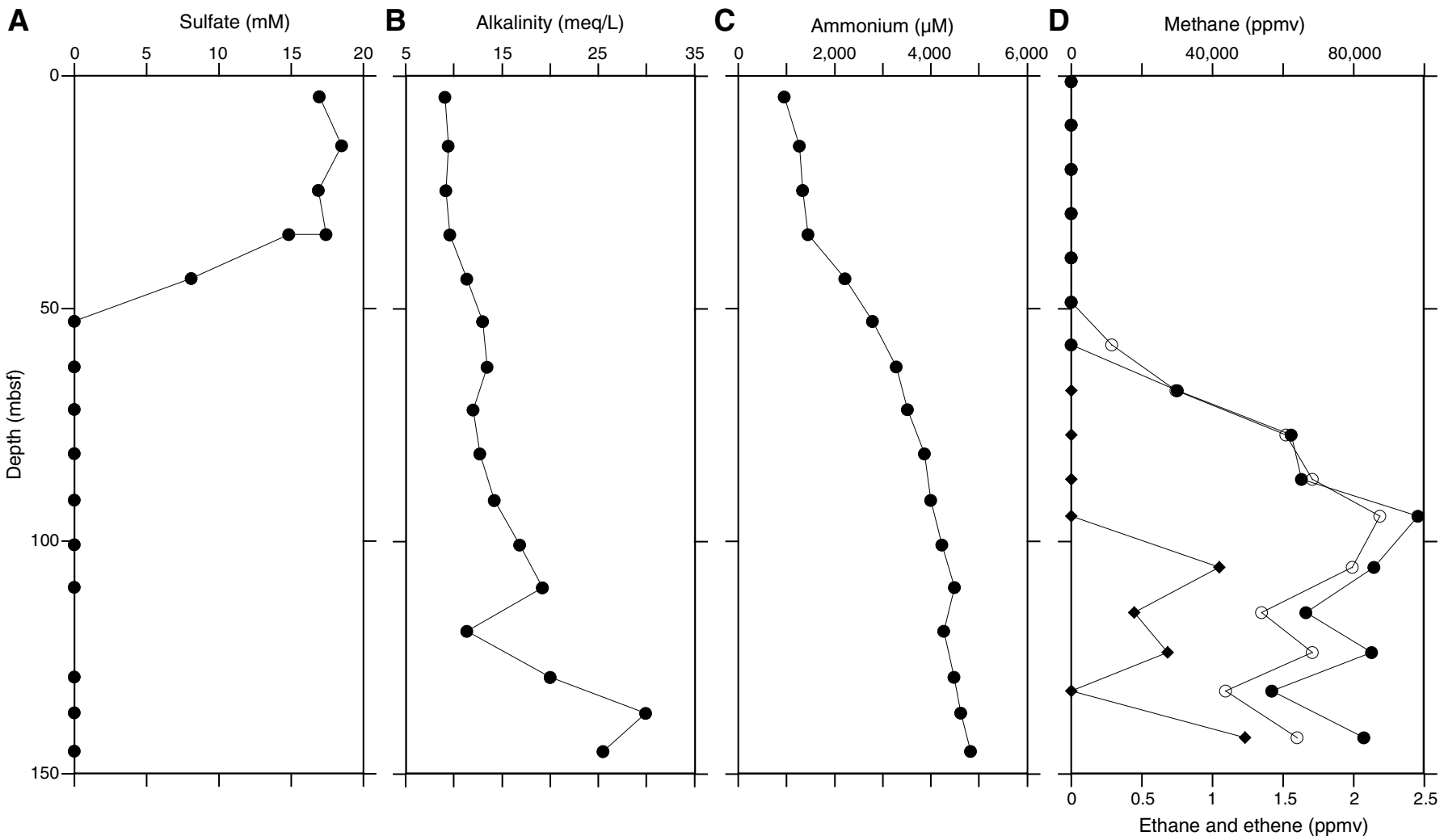

Figure F28. A–C. Plots of interstitial water calcium, magnesium, and potassium, Hole U1385B. Solid circles = inductively coupled plasma–atomic emission spectrometer measurement, open circles = ion chromatograph measurement.

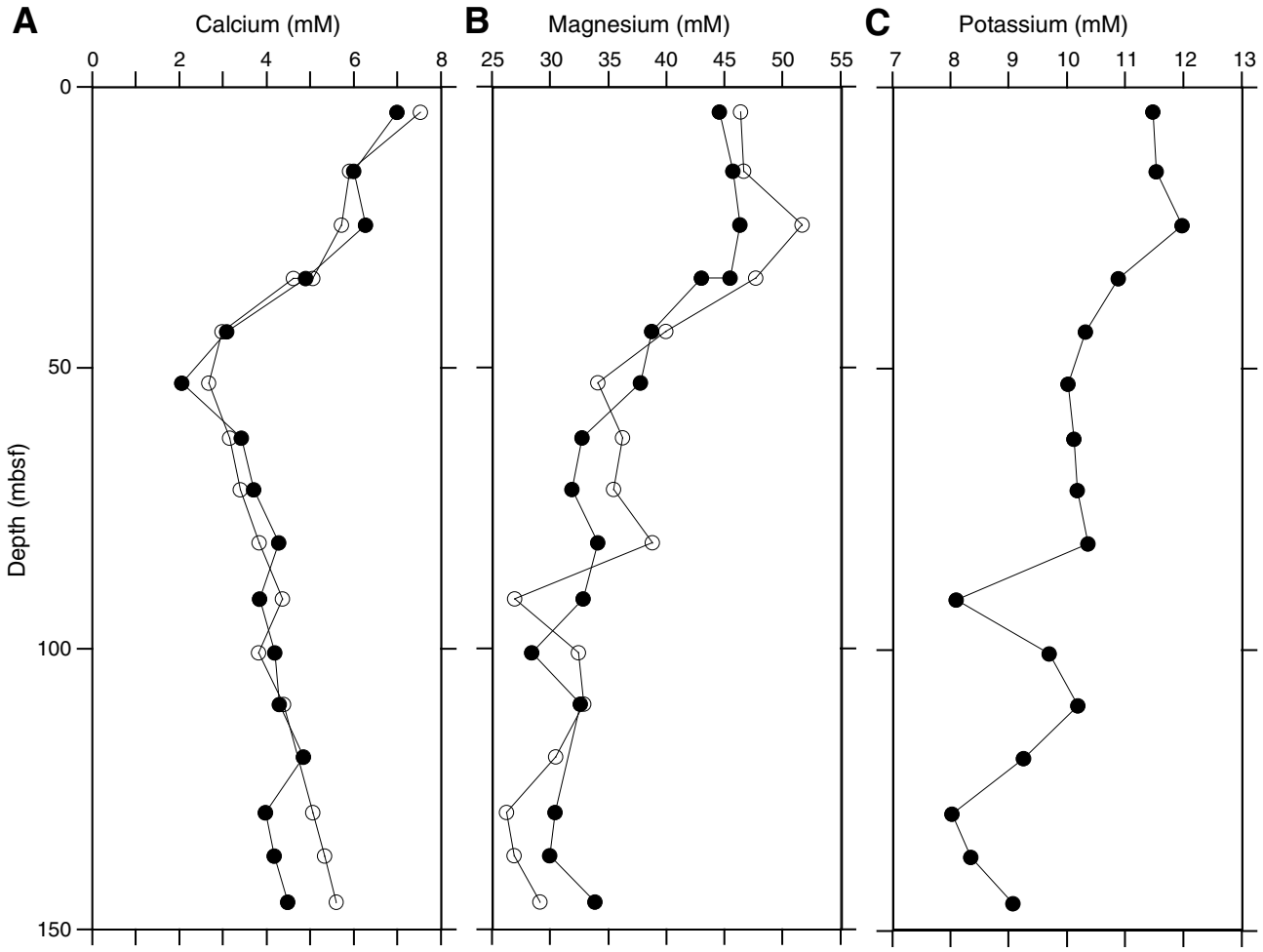

Figure F29. A–E. Plots of interstitial water strontium, barium, lithium, boron, and silicon, Hole U1385B.

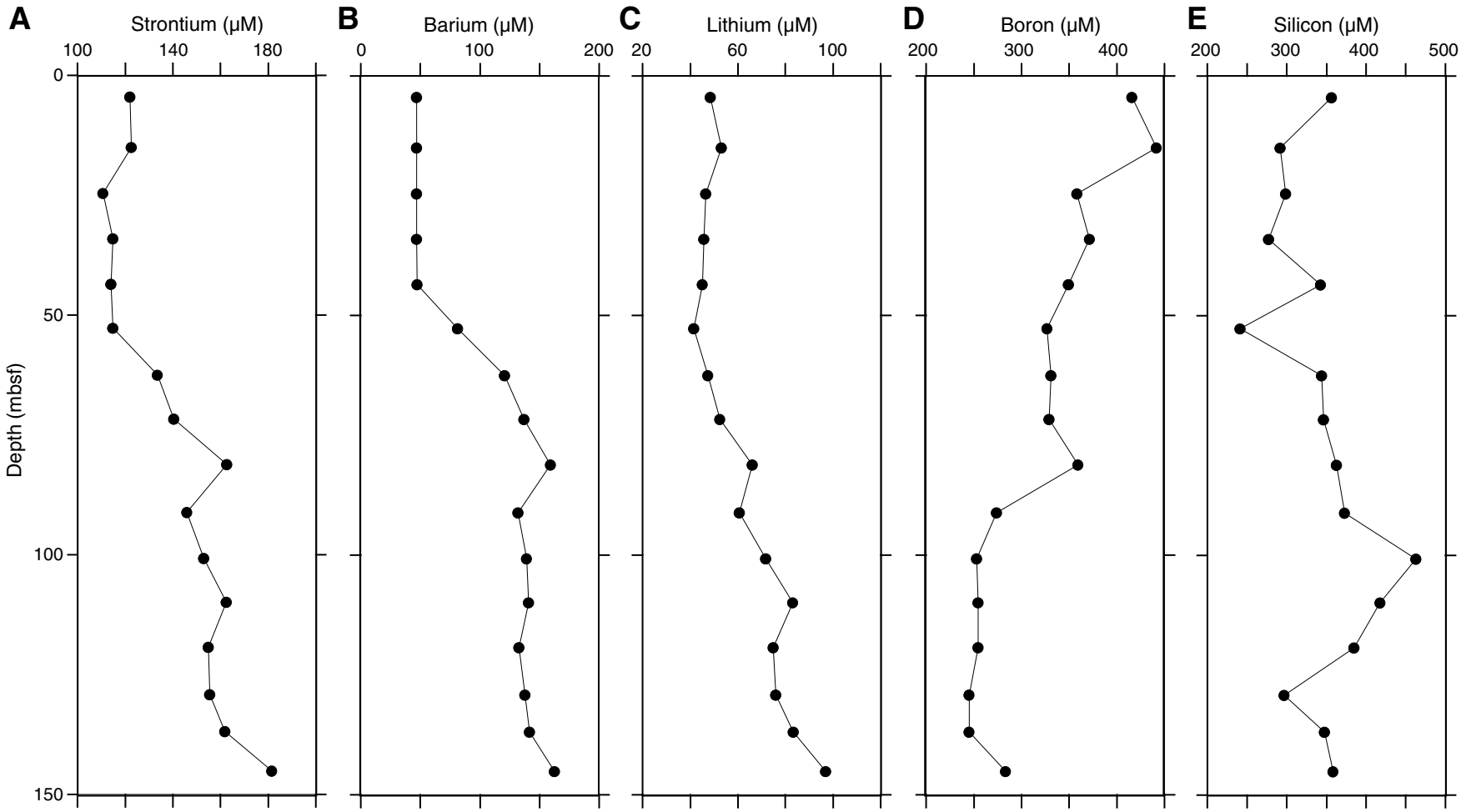

Figure F30. Plots of interstitial water manganese and iron, Hole U1385B.

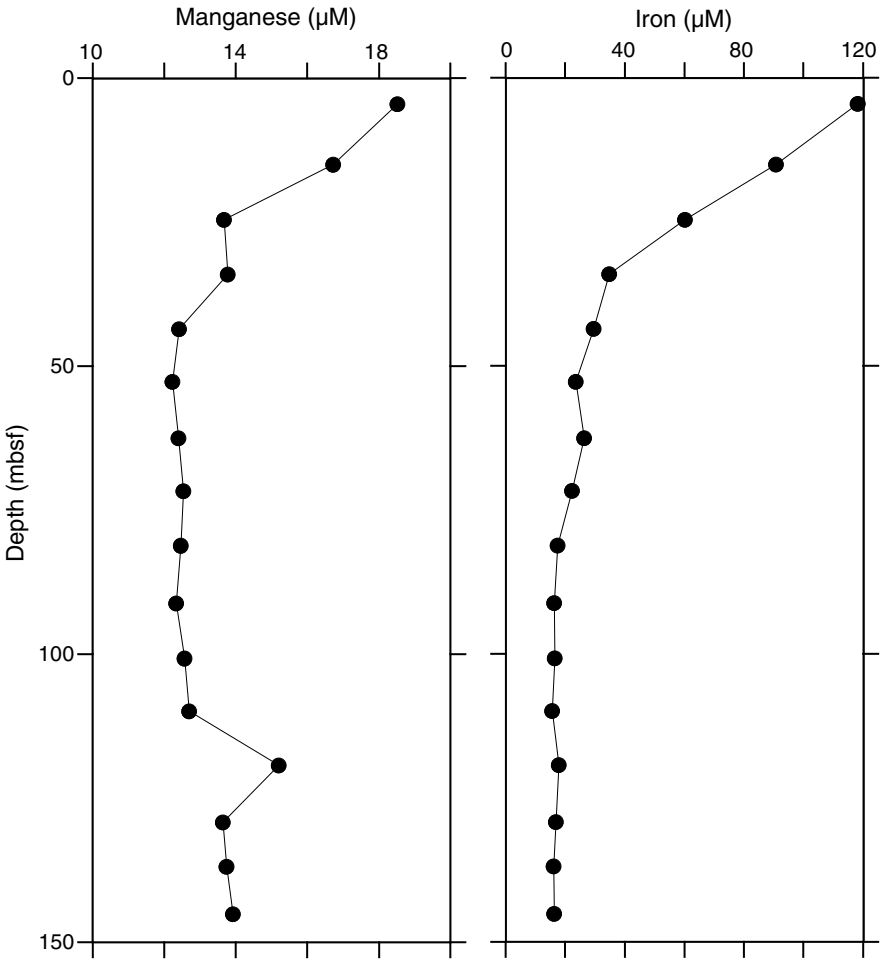

Figure F31. A–C. Plots of interstitial water stable isotopes and chloride from whole-round or syringe samples taken at the base of each core, Hole U1385B. VSMOW = Vienna standard mean ocean water.

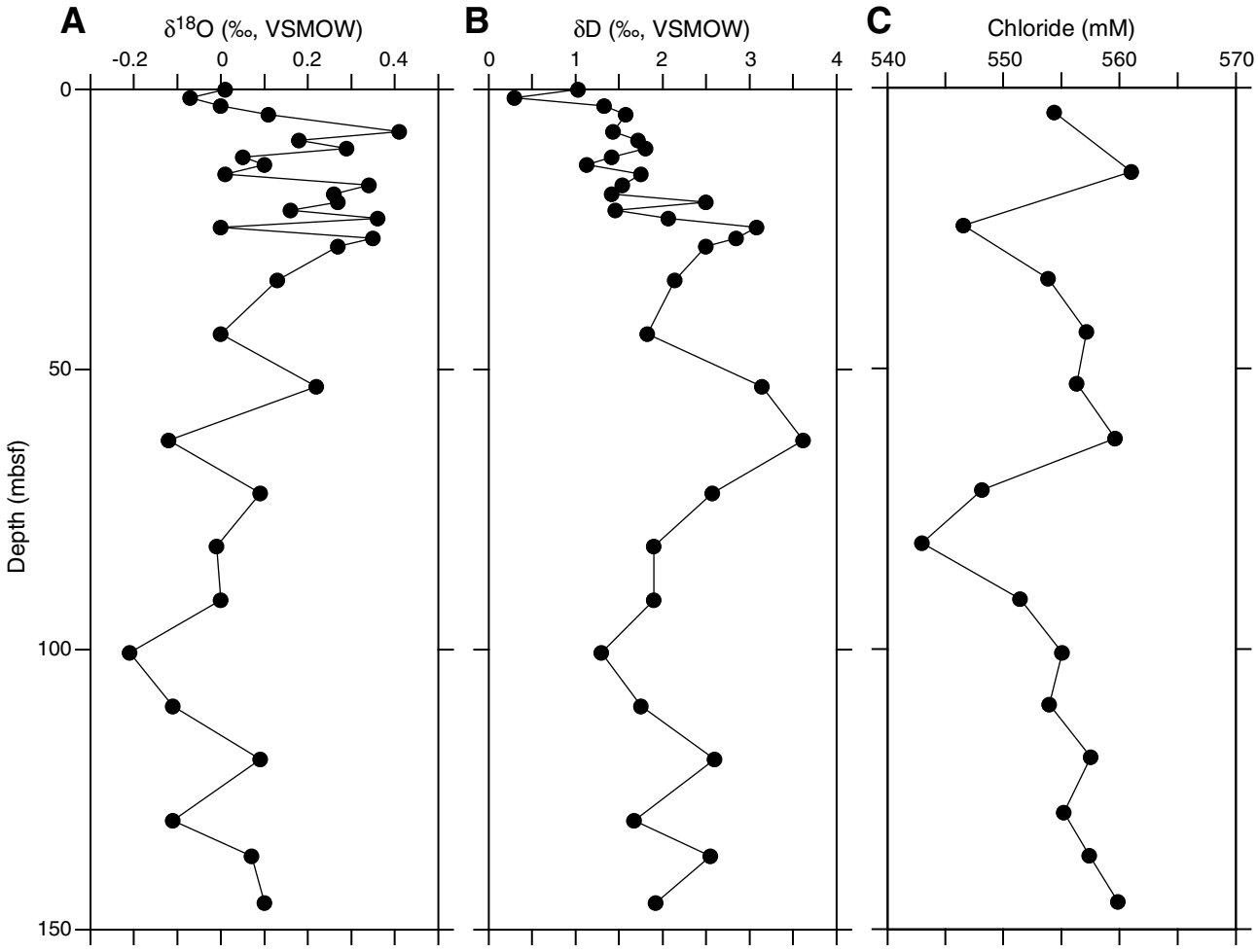

Figure F32. Plot of $\delta^{18}O$ vs. δD, Hole U1385B. VSMOW = Vienna standard mean ocean water.

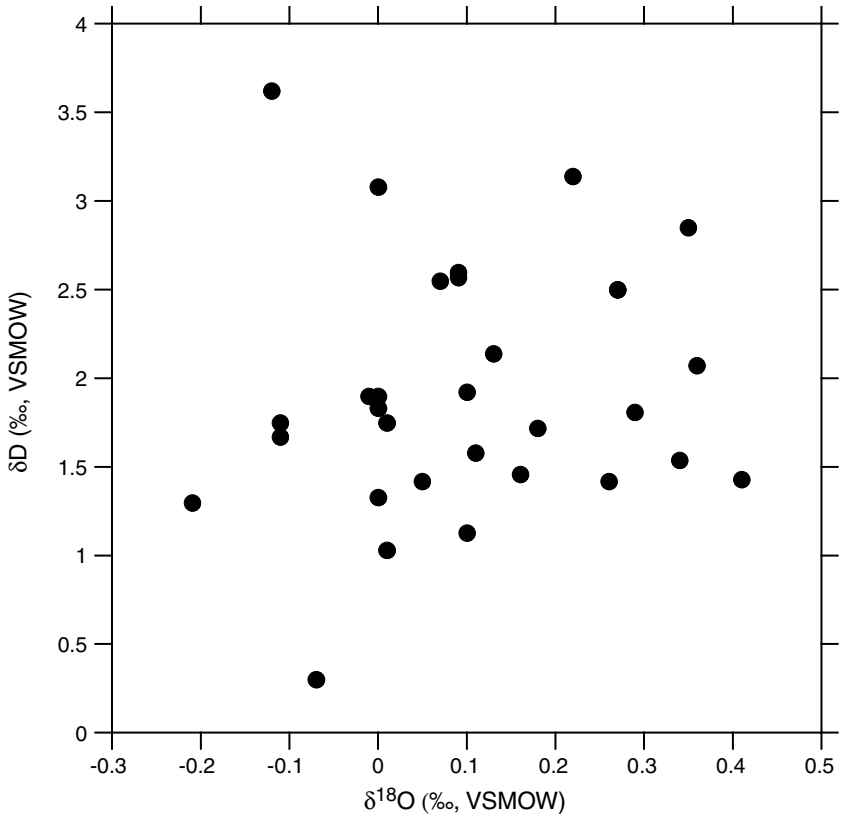

Figure F33. Plot of interstitial water sulfate concentrations using different sampling methods, Site U1385.

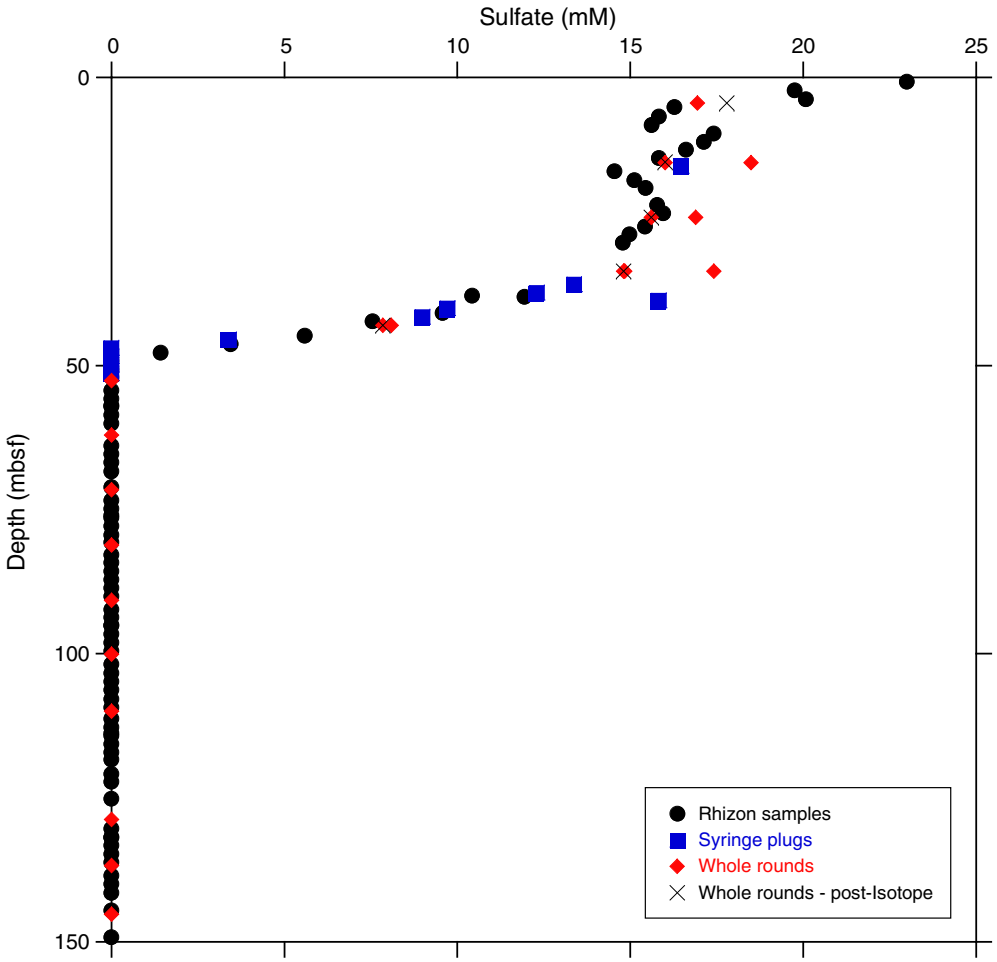

Figure F34. Plots of heat flow calculations, Site U1385. **A.** Sediment temperatures in Holes U1385A (red), U1385B (green), and U1385D (blue) with average values for Cores 4H, 7H, 10H, and 13H from each hole (black squares). **B.** Thermal conductivity data (circles) from Hole U1385A with calculated thermal resistance (solid line). **C.** Bullard plot in which heat flow is calculated from a linear fit of the temperature data.

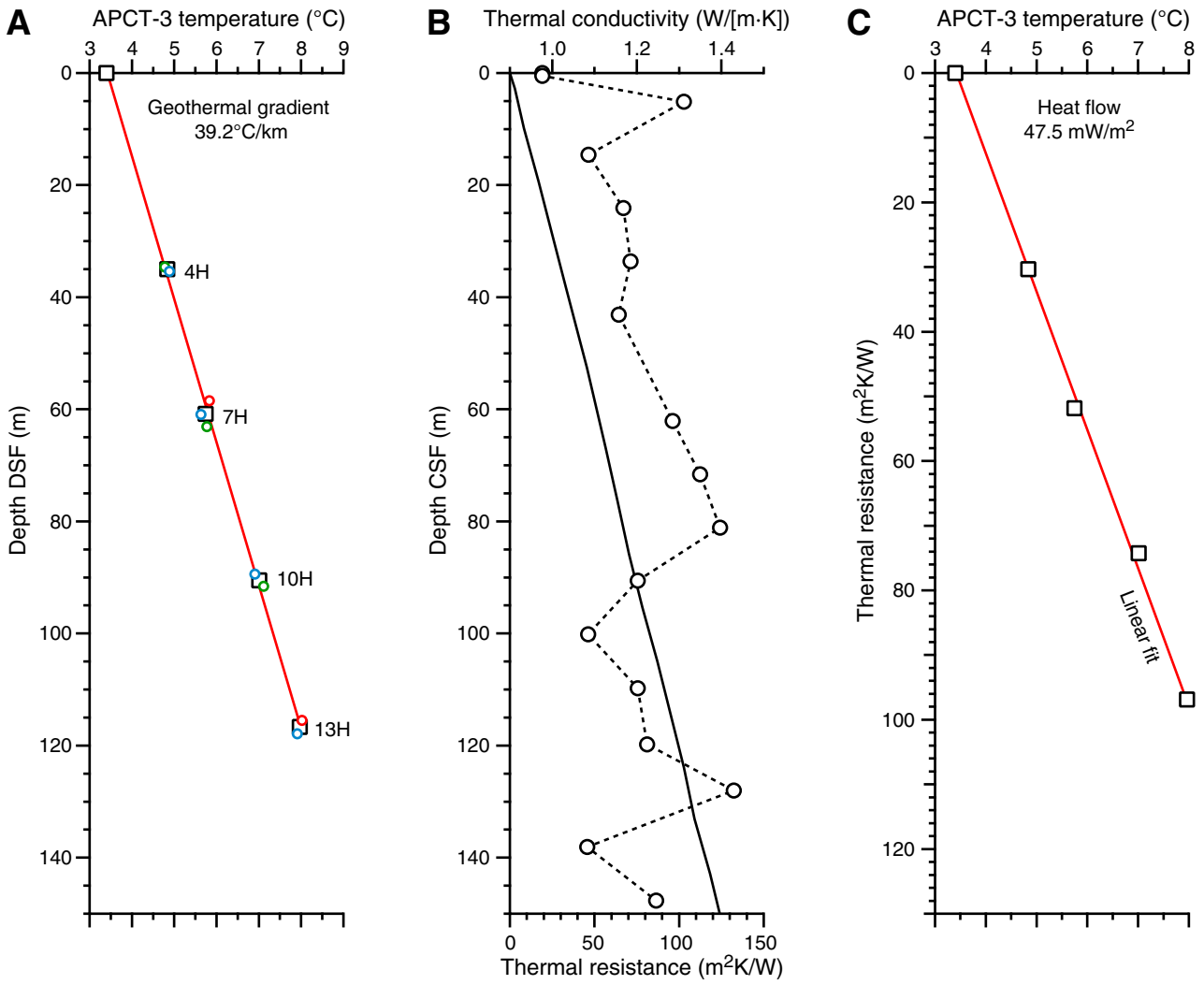

Figure F35. Plots of magnetic susceptibility vs. composite depth, Site U1385. **A.** 0–40 mcd. (Continued on next three pages.)

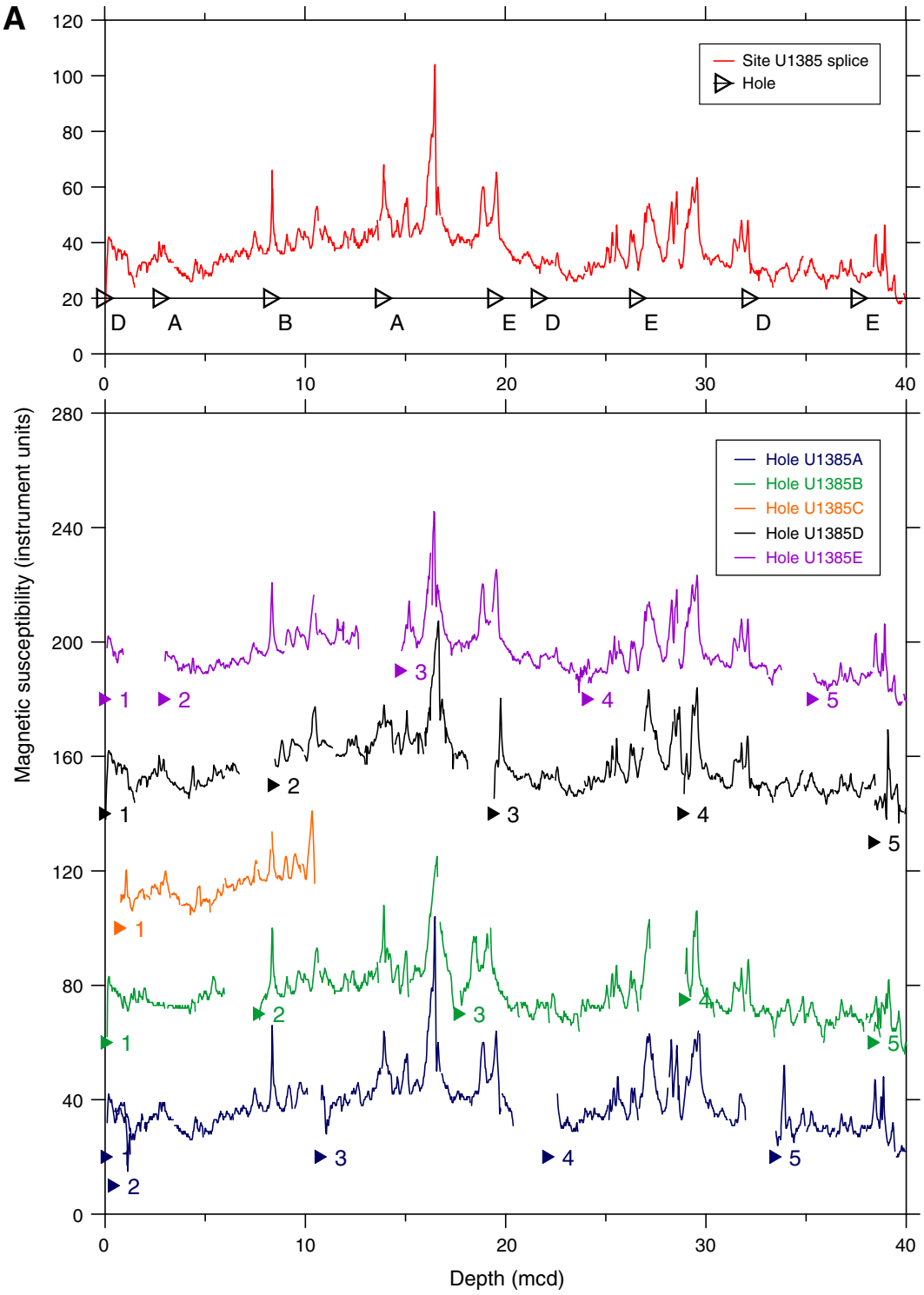

Figure F35 (continued). B. 40–80 mcd. (Continued on next page.)

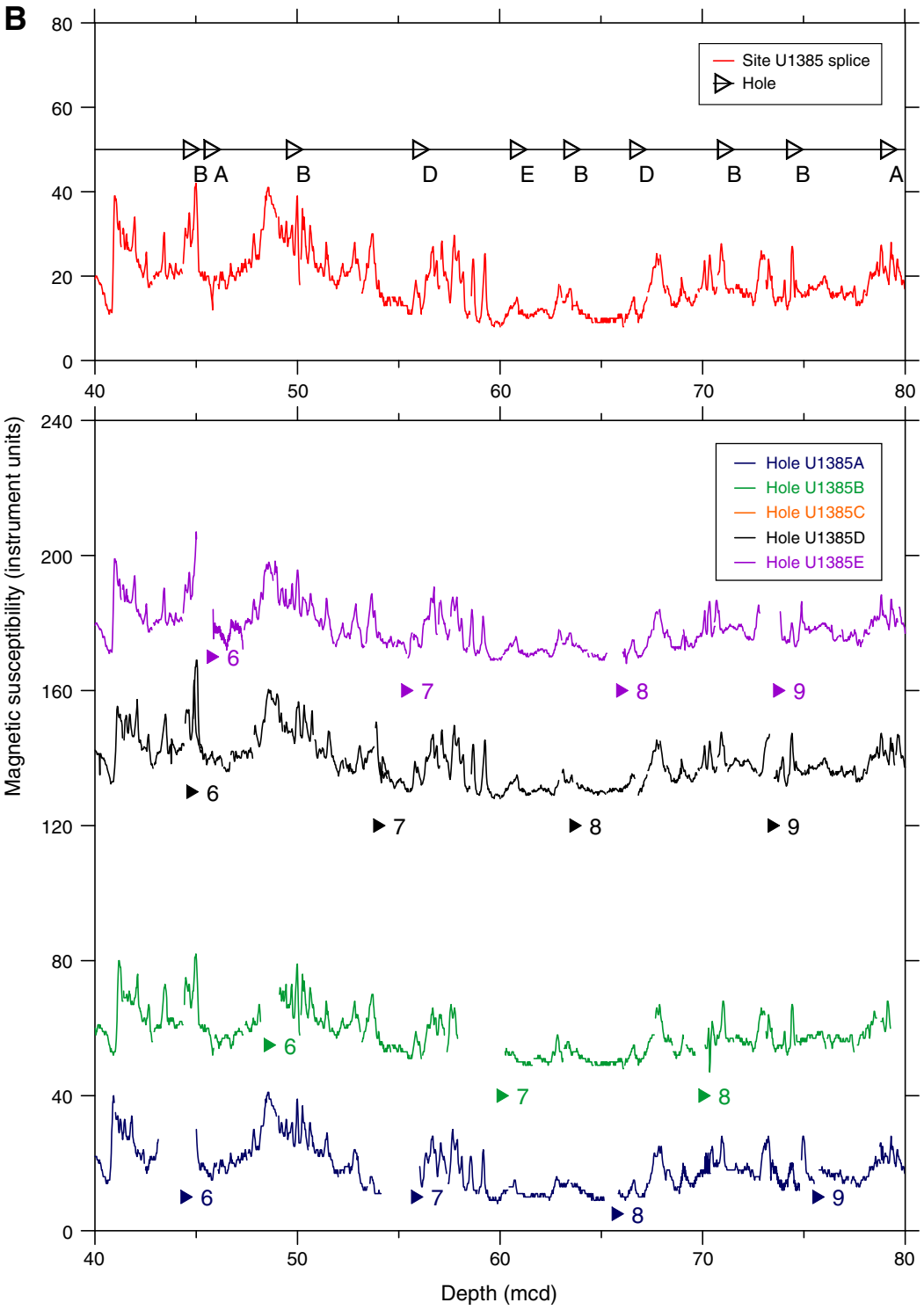

Figure F35 (continued). C. 80–120 mcd. (Continued on next page.)

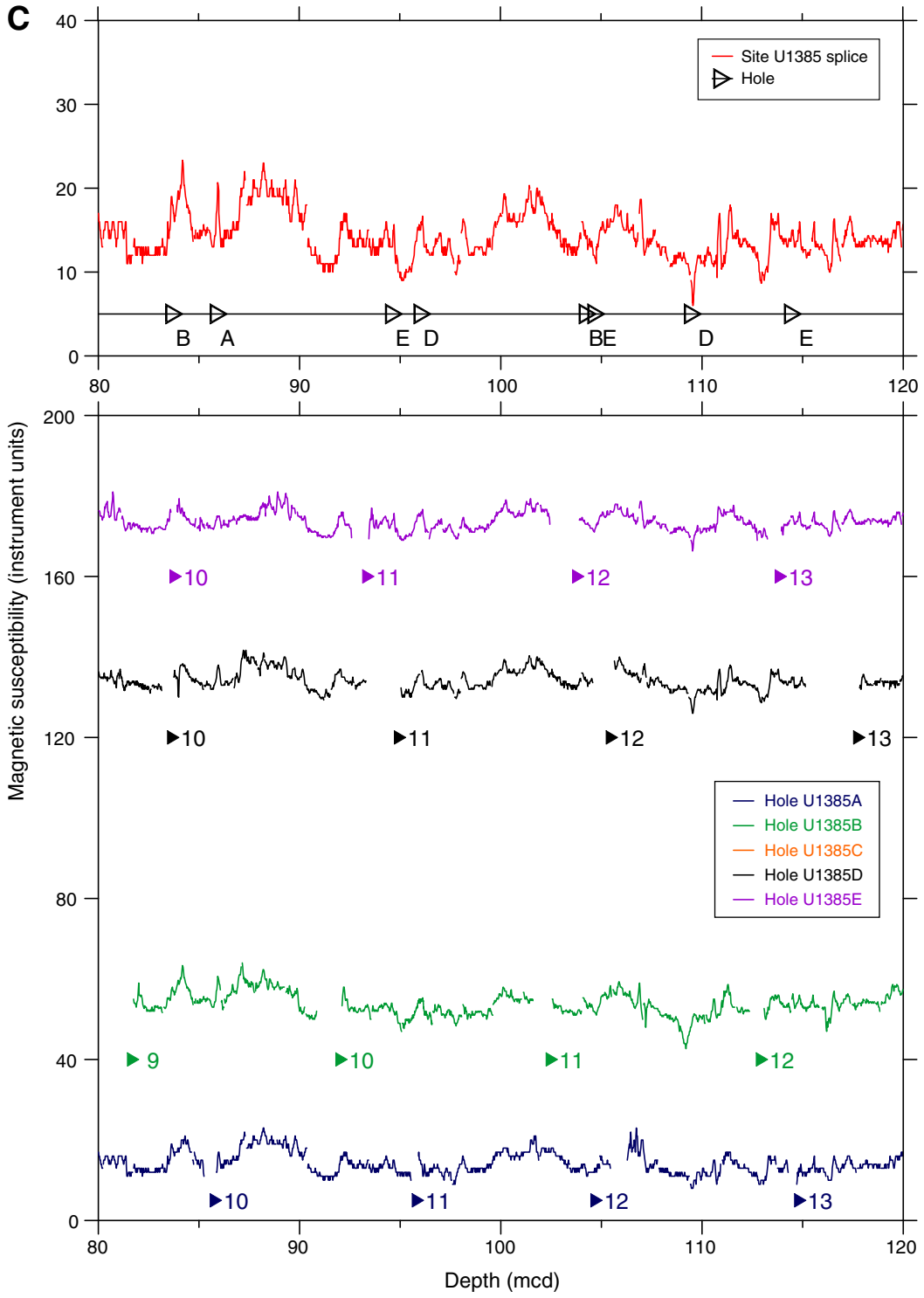

Figure F35 (continued). D. 120–170 mcd.

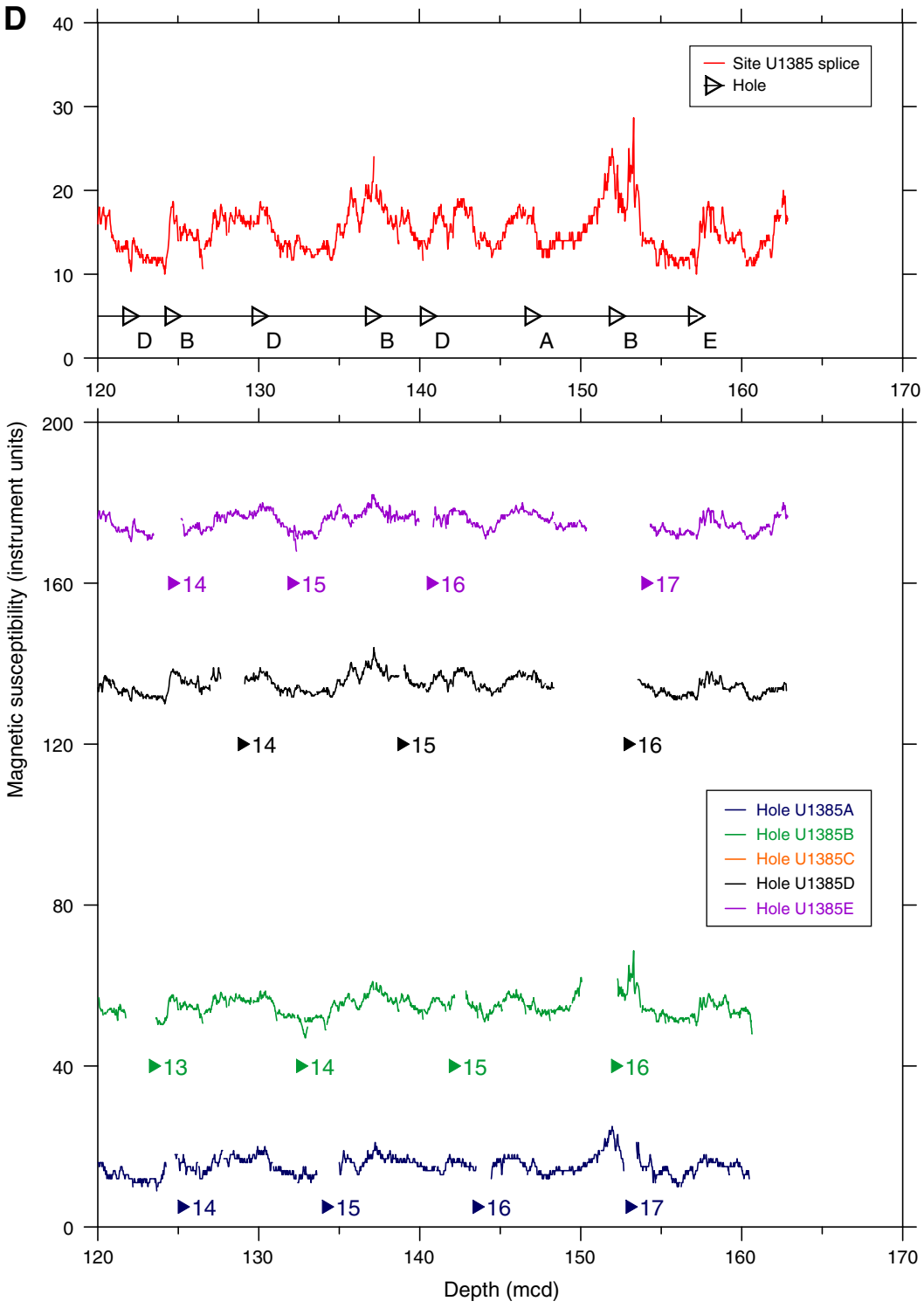

Figure F36. Plots of core top depths for mbsf vs. mcd. Lines fit through the core top depths for each hole give the relative expansion of the mcd scale relative to the mbsf scale.

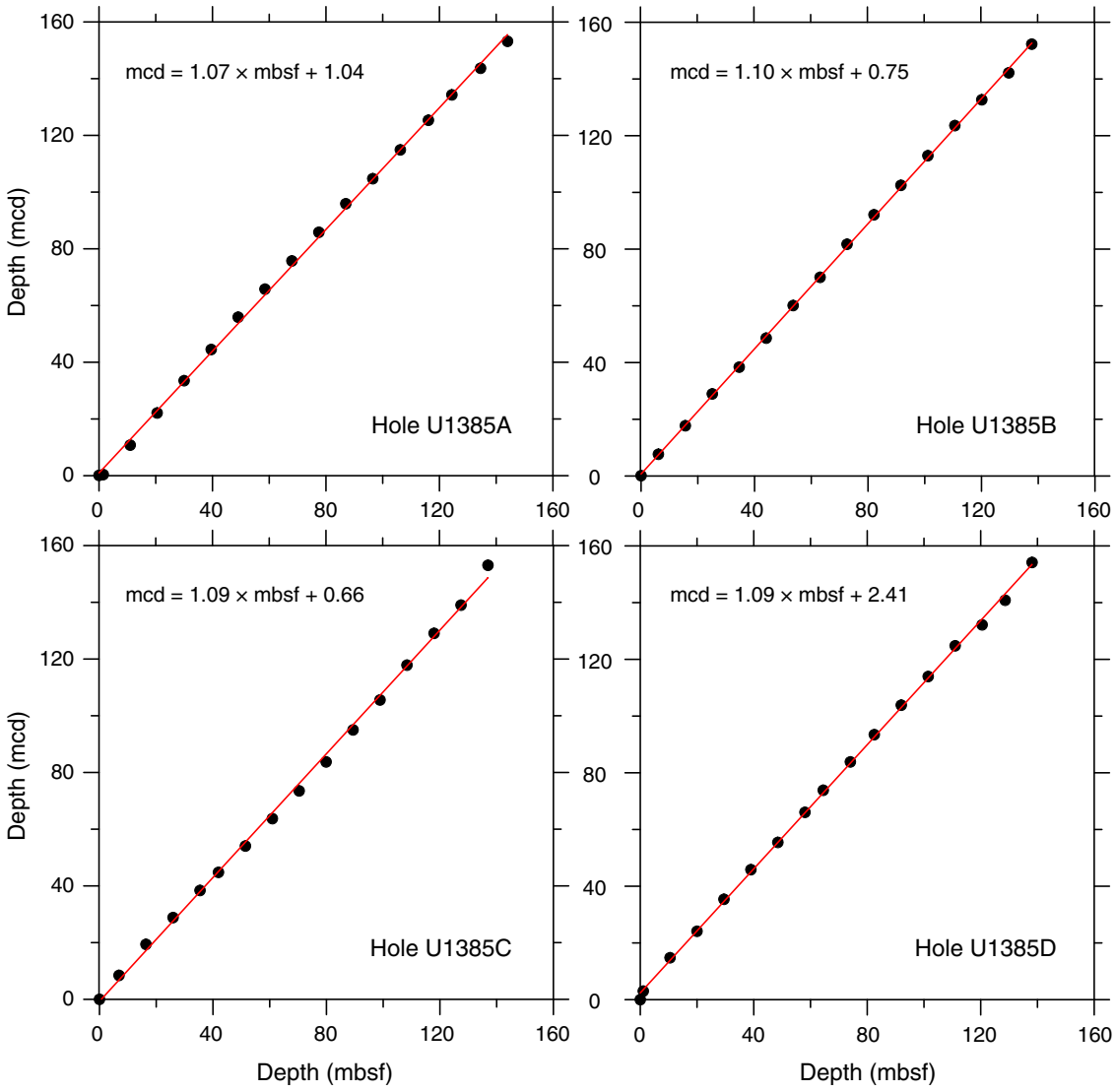

Figure F37. Plots of secondary stratigraphic splices compared with the primary splice, Site U1385. **A.** 0–40 mcd. (Continued on next three pages.)

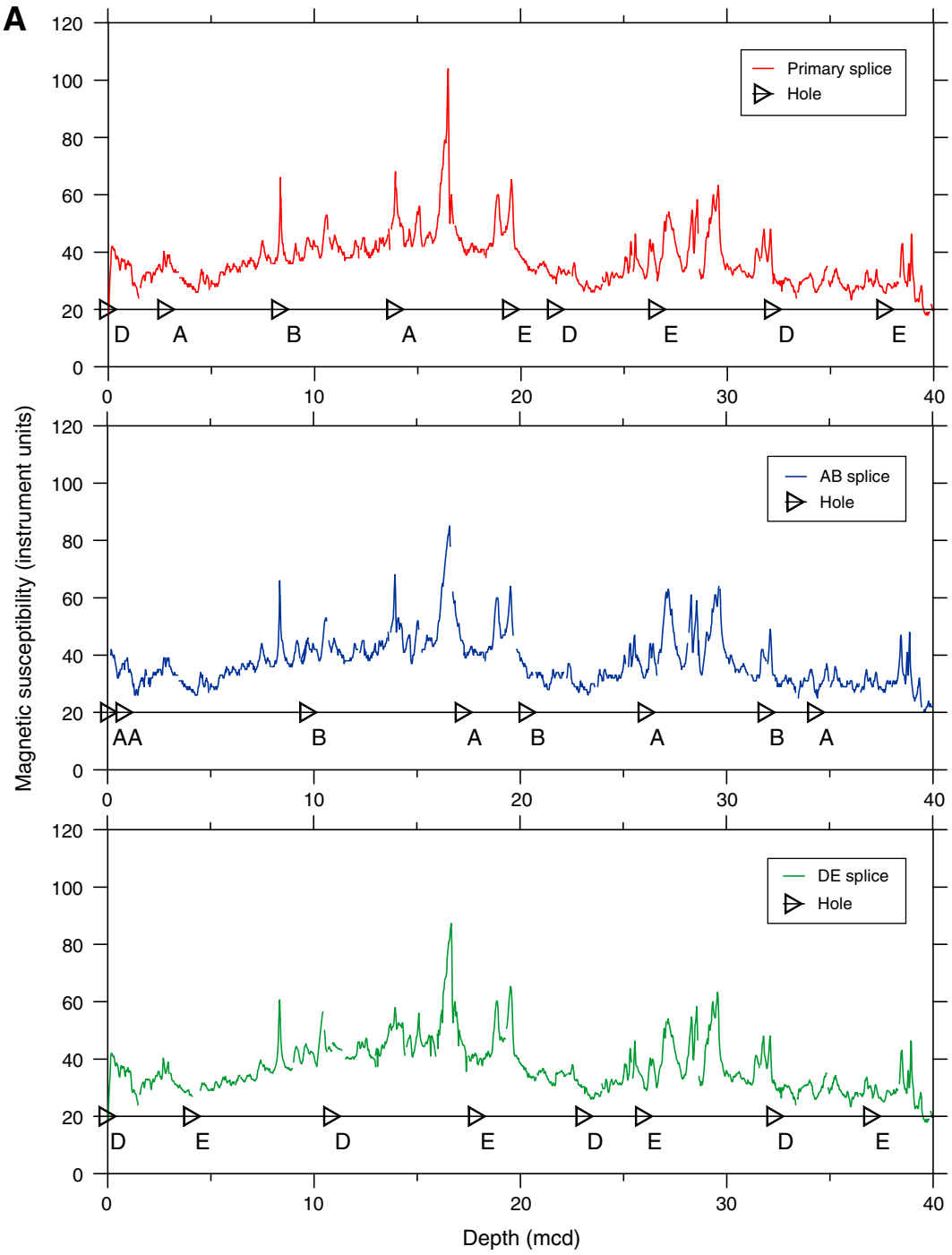

Figure F37 (continued). B. 40–80 mcd. (Continued on next page.)

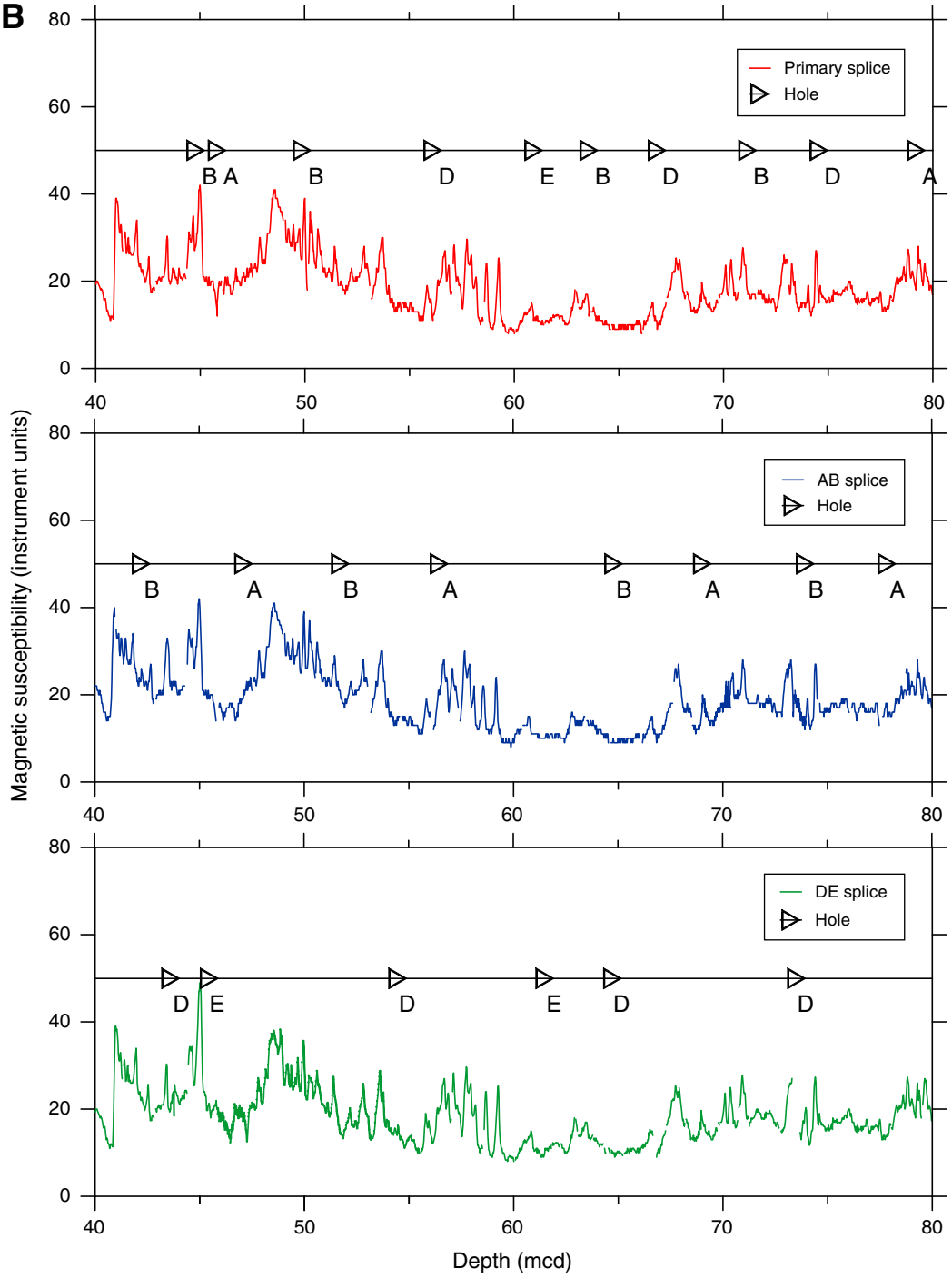

Figure F37 (continued). C. 80–120 mcd. (Continued on next page.)

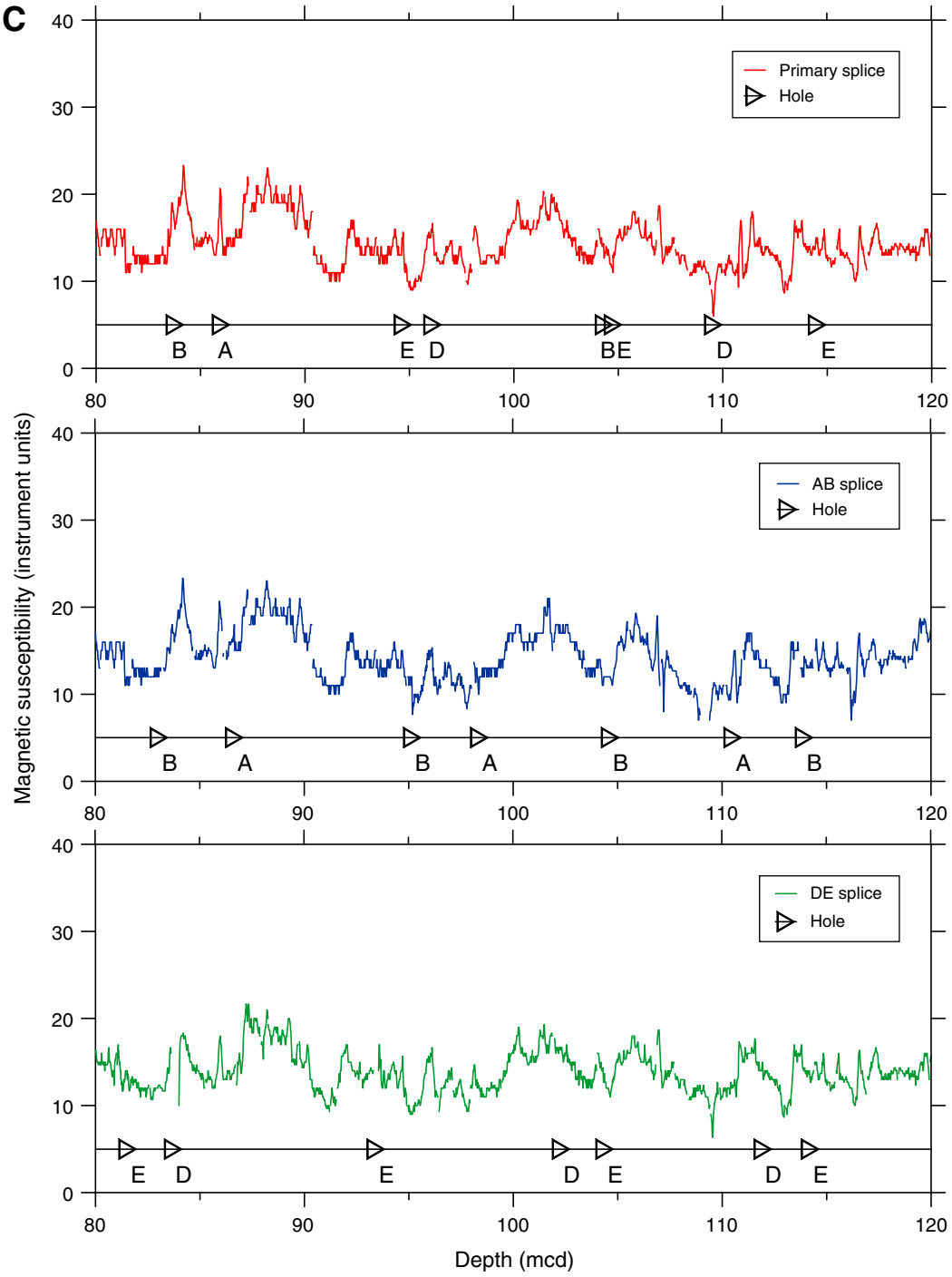

Figure F37 (continued). D. 120–170 mcd.

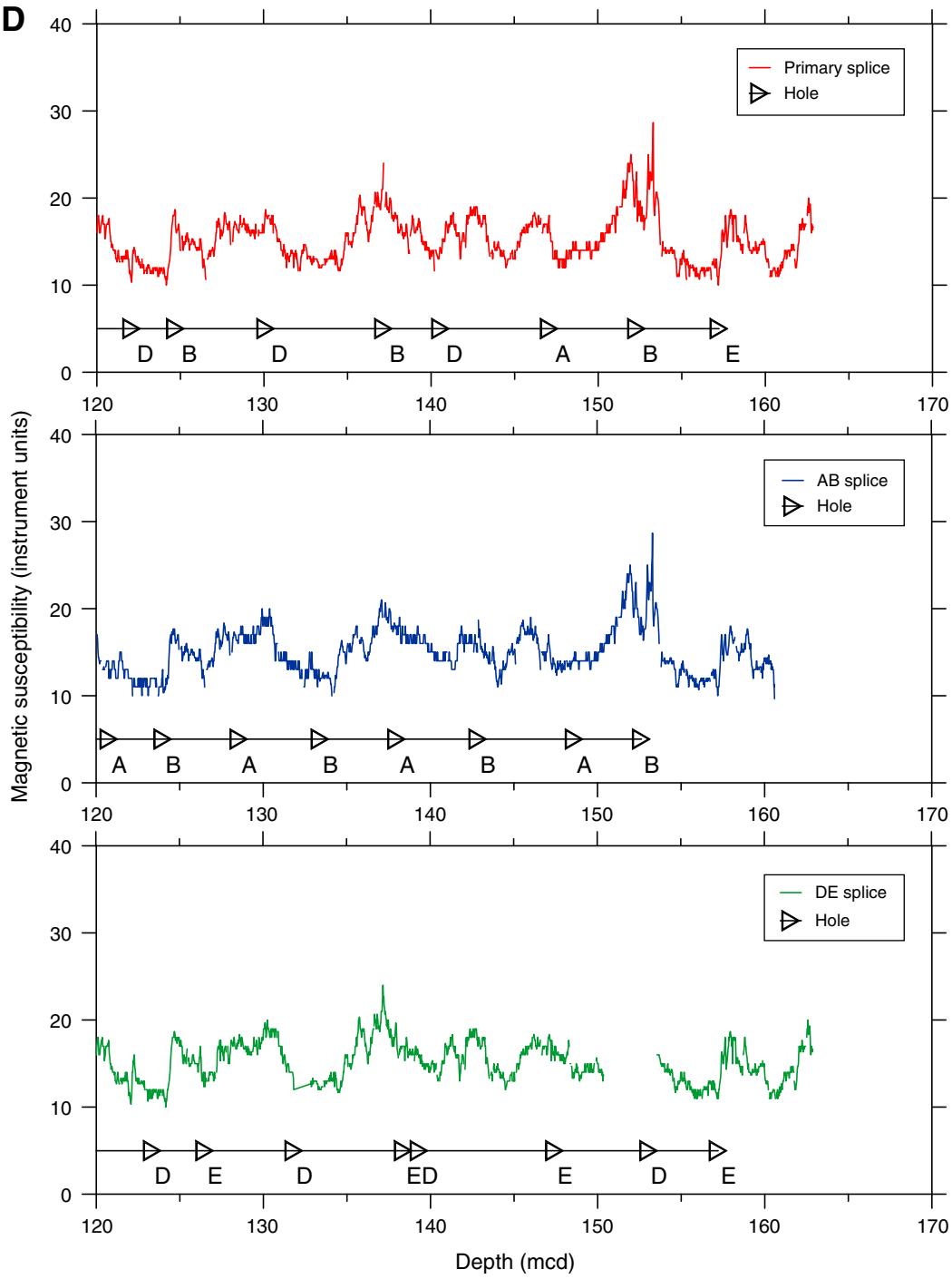

Figure F38. Plots of core top depths for mcd vs. mbsf*, Holes U1385A–U1385E. Line fit through the core top depths of all holes gives an estimate of the amount the mcd scale has to be compressed to derive the mbsf* scale.

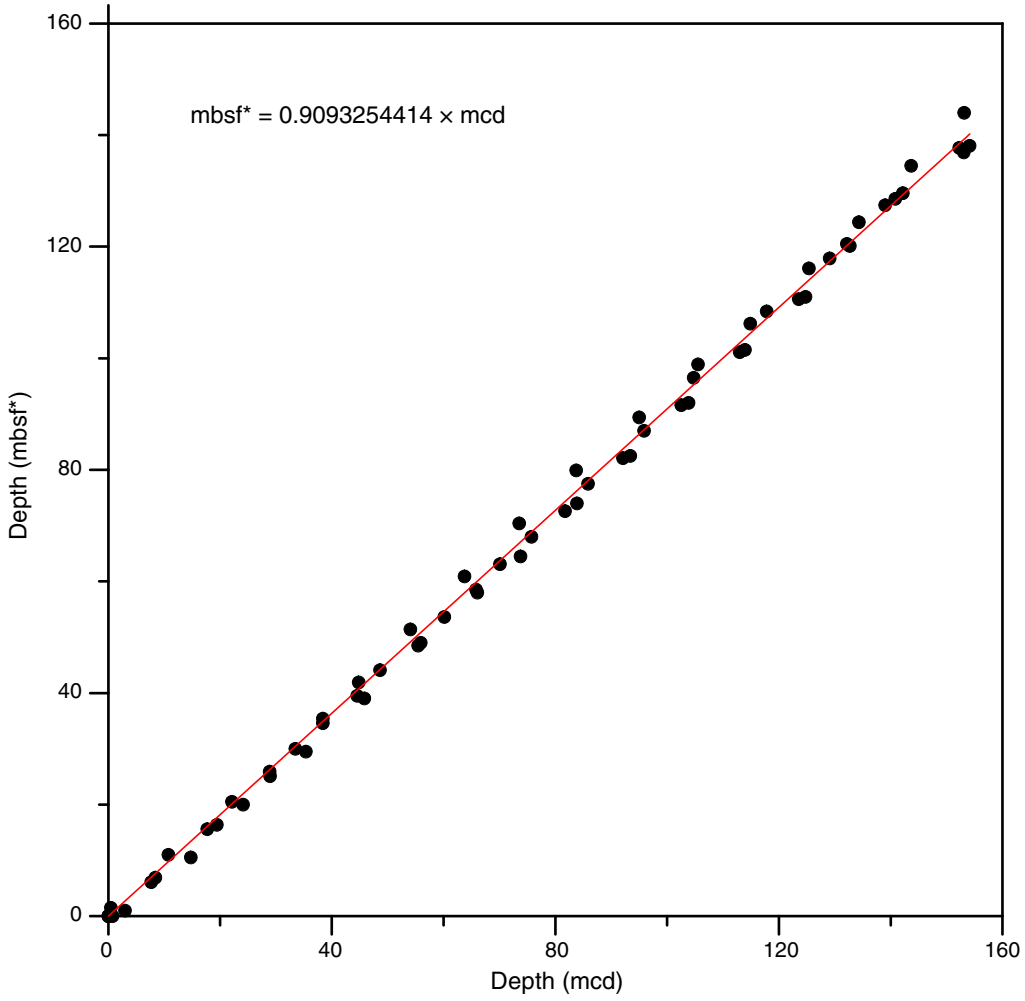

Table T1. Coring summary, Site U1385. (Continued on next two pages.)

Hole U1385A
Latitude: 37°34.2894′N
Longitude: 10°7.5708′W
Time on hole (d): 1.7
Seafloor (drill pipe measurement below rig floor, m DRF): 2598 (APC mudline)
Distance between rig floor and sea level (m): 11.0
Water depth (drill pipe measurement from sea level, mbsl): 2587
Total penetration (drilling depth below seafloor, m DSF): 151.5
Total length of cored section (m): 151.5
Total core recovered (m): 155.87
Core recovery (%): 103
Total number of cores: 17

Hole U1385B
Latitude: 37°34.2892′N
Longitude: 10°7.5561′W
Time on hole (d): 0.8
Seafloor (drill pipe measurement below rig floor, m DRF): 2598 (APC mudline)
Distance between rig floor and sea level (m): 11.0
Water depth (drill pipe measurement from sea level, mbsl): 2587
Total penetration (drilling depth below seafloor, m DSF): 146.3
Total length of cored section (m): 146.3
Total core recovered (m): 150.73
Core recovery (%): 103
Total number of cores: 16

Hole U1385C
Latitude: 37°34.2892′N
Longitude: 10°7.5561′W
Time on hole (d): 0.1
Seafloor (drill pipe measurement below rig floor, m DRF): 2598 (APC mudline)
Distance between rig floor and sea level (m): 11.0
Water depth (drill pipe measurement from sea level, mbsl): 2587
Total penetration (drilling depth below seafloor, m DSF): 9.1
Total length of cored section (m): 9.5
Total core recovered (m): 9.87
Core recovery (%): 104
Total number of cores: 1

Hole U1385D
Latitude: 37°34.2784′N
Longitude: 10°7.5559′W
Time on hole (d): 0.8
Seafloor (drill pipe measurement below rig floor, m DRF): 2595 (APC mudline)
Distance between rig floor and sea level (m): 11.0
Water depth (drill pipe measurement from sea level, mbsl): 2584
Total penetration (drilling depth below seafloor, m DSF): 146.4
Total length of cored section (m): 146.4
Total core recovered (m): 153.95
Core recovery (%): 105
Total number of cores: 16

Hole U1385E
Latitude: 37°34.2785′N
Longitude: 10°7.5692′W
Time on hole (d): 1.1
Seafloor (drill pipe measurement below rig floor, m DRF): 2600 (APC mudline)
Distance between rig floor and sea level (m): 11.0
Water depth (drill pipe measurement from sea level, mbsl): 2589
Total penetration (drilling depth below seafloor, m DSF): 148.7
Total length of cored section (m): 148.7
Total core recovered (m): 151.32
Core recovery (%): 102
Total number of cores: 17

Site U1385 totals
Number of cores: 67
Penetration (m): 602.4
Cored (m): 602.4
Recovered (m): 621.7 (103.2%)

Table T1 continued. (Continued on next page.)

Core	Date (2011)	Time (h)	Depth DSF (m) Top of cored interval	Depth DSF (m) Bottom of cored interval	Interval advanced (m)	Depth CSF (m) Top of recovered core	Depth CSF (m) Bottom of recovered core	Length of core recovered (m)	Curated length (m)	Recovery (%)
339-U1385A-										
1H	25 Nov	2325	0.0	1.5	1.5	0.0	1.44	1.53	1.44	102
2H	26 Nov	0222	1.5	11.0	9.5	1.5	11.35	9.85	9.85	104
3H	26 Nov	0329	11.0	20.5	9.5	11.0	20.92	9.92	9.92	104
4H	26 Nov	0440	20.5	30.0	9.5	20.5	30.71	10.21	10.21	107
5H	26 Nov	0534	30.0	39.5	9.5	30.0	39.97	9.97	9.97	105
6H	26 Nov	0632	39.5	49.0	9.5	39.5	49.48	9.98	9.98	105
7H	26 Nov	0800	49.0	58.5	9.5	49.0	58.77	9.77	9.77	103
8H	26 Nov	0855	58.5	68.0	9.5	58.5	68.64	10.14	10.14	107
9H	26 Nov	0940	68.0	77.5	9.5	68.0	77.83	9.83	9.83	103
10H	26 Nov	1030	77.5	87.0	9.5	77.5	87.78	10.28	10.28	108
11H	26 Nov	1125	87.0	96.5	9.5	87.0	96.83	9.83	9.83	103
12H	26 Nov	1210	96.5	106.0	9.5	96.5	106.34	9.70	9.84	102
13H	26 Nov	1305	106.0	115.5	9.5	106.0	116.12	10.12	10.12	107
14H	26 Nov	1345	115.5	125.0	9.5	115.5	124.67	9.08	9.17	96
15H	26 Nov	1450	125.0	134.5	9.5	125.0	133.88	8.77	8.88	92
16H	26 Nov	1540	134.5	144.0	9.5	134.5	143.80	9.30	9.30	98
17H	26 Nov	1625	144.0	151.5	7.5	144.0	151.63	7.59	7.63	101
				Advanced total:	151.5					
				Total interval cored:	155.87					
339-U1385B-										
1H	27 Nov	0055	0.0	6.1	6.1	0.0	6.14	6.14	6.14	101
2H	27 Nov	0200	6.1	15.6	9.5	6.1	16.01	9.91	9.91	104
3H	27 Nov	0240	15.6	25.1	9.5	15.6	25.44	9.84	9.84	104
4H	27 Nov	0340	25.1	34.6	9.5	25.1	35.12	10.02	10.02	105
5H	27 Nov	0440	34.6	44.1	9.5	34.6	44.78	10.18	10.18	107
6H	27 Nov	0525	44.1	53.6	9.5	44.1	53.85	9.75	9.75	103
7H	27 Nov	0630	53.6	63.1	9.5	53.6	63.65	10.05	10.05	106
8H	27 Nov	0725	63.1	72.6	9.5	63.1	72.68	9.58	9.58	101
9H	27 Nov	0810	72.6	82.1	9.5	72.6	82.13	9.53	9.53	100
10H	27 Nov	0915	82.1	91.6	9.5	82.1	92.16	9.97	10.06	105
11H	27 Nov	1010	91.6	101.1	9.5	91.6	101.78	10.14	10.18	107
12H	27 Nov	1055	101.1	110.6	9.5	101.1	110.22	9.09	9.12	96
13H	27 Nov	1155	110.6	120.1	9.5	110.6	120.52	9.97	9.92	105
14H	27 Nov	1240	120.1	129.6	9.5	120.1	130.01	9.80	9.91	103
15H	27 Nov	1325	129.6	137.7	8.1	129.6	137.89	8.16	8.29	101
16H	27 Nov	1415	137.7	146.3	8.6	137.7	146.30	8.60	8.60	100
				Advanced total:	146.3					
				Total interval cored:	150.73					
339-U1385C-										
1H	27 Nov	1845	0.0	9.5	9.5	0.0	9.92	9.87	9.92	104
				Advanced total:	9.5					
				Total interval cored:	9.87					
339-U1385D-										
1H	27 Nov	2100	0.0	6.9	6.9	0.0	6.99	6.95	6.99	101
2H	27 Nov	2145	6.9	16.4	9.5	6.9	16.89	9.93	9.99	105
3H	27 Nov	2240	16.4	25.9	9.5	16.4	26.34	9.88	9.94	104
4H	27 Nov	2335	25.9	35.4	9.5	25.9	36.07	10.14	10.17	107
5H	28 Nov	0035	35.4	41.9	6.5	35.4	42.73	7.30	7.33	112
6H	28 Nov	0130	41.9	51.4	9.5	41.9	51.94	10.02	10.04	105
7H	28 Nov	0230	51.4	60.9	9.5	51.4	61.39	9.97	9.99	105
8H	28 Nov	0315	60.9	70.4	9.5	60.9	70.85	9.94	9.95	105
9H	28 Nov	0410	70.4	79.9	9.5	70.4	80.48	9.97	10.08	105
10H	28 Nov	0505	79.9	89.4	9.5	79.9	89.94	9.97	10.04	105
11H	28 Nov	0600	89.4	98.9	9.5	89.4	99.40	9.89	10.00	104
12H	28 Nov	0655	98.9	108.4	9.5	98.9	108.91	9.94	10.01	105
13H	28 Nov	0755	108.4	117.9	9.5	108.4	118.78	10.36	10.38	109
14H	28 Nov	0905	117.9	127.4	9.5	117.9	127.87	9.90	9.97	104
15H	28 Nov	0955	127.4	136.9	9.5	127.4	137.07	9.69	9.67	102
16H	28 Nov	1110	136.9	146.4	9.5	136.9	147.02	10.10	10.12	106
				Advanced total:	146.4					
				Total interval cored:	153.95					

Table T1 (continued).

Core	Date (2011)	Time (h)	Depth DSF (m) Top of cored interval	Depth DSF (m) Bottom of cored interval	Interval advanced (m)	Depth CSF (m) Top of recovered core	Depth CSF (m) Bottom of recovered core	Length of core recovered (m)	Curated length (m)	Recovery (%)
339-U1385E-										
1H	28 Nov	1535	0.0	1.0	1.0	0.0	1.13	1.13	1.13	113
2H	28 Nov	1630	1.0	10.5	9.5	1.0	10.99	9.93	9.99	105
3H	28 Nov	1710	10.5	20.0	9.5	10.5	20.17	9.62	9.67	101
4H	28 Nov	1750	20.0	29.5	9.5	20.0	30.05	10.02	10.05	105
5H	28 Nov	1840	29.5	39.0	9.5	29.5	39.50	9.96	10.00	105
6H	28 Nov	1925	39.0	48.5	9.5	39.0	48.89	9.89	9.89	104
7H	28 Nov	2020	48.5	58.0	9.5	48.5	58.60	10.10	10.10	106
8H	28 Nov	2120	58.0	64.5	6.5	58.0	65.08	7.08	7.08	109
9H	28 Nov	2205	64.5	74.0	9.5	64.5	74.55	10.05	10.05	106
10H	28 Nov	2255	74.0	82.5	8.5	74.0	82.98	8.98	8.98	106
11H	28 Nov	2345	82.5	92.0	9.5	82.5	91.97	9.40	9.47	99
12H	29 Nov	0030	92.0	101.5	9.5	92.0	101.76	9.76	9.76	103
13H	29 Nov	0120	101.5	111.0	9.5	101.5	111.49	9.93	9.99	105
14H	29 Nov	0205	111.0	120.5	9.5	111.0	119.25	8.28	8.25	87
15H	29 Nov	0430	120.5	130.1	9.6	120.5	128.74	8.10	8.24	84
16H	29 Nov	0530	128.6	138.1	9.5	128.6	138.67	9.99	10.07	105
17H	29 Nov	0630	138.1	147.2	9.1	138.1	147.26	9.10	9.16	100
				Advanced total:	148.7					
				Total interval cored:	151.32					

DRF = drilling depth below rig floor, DSF = drilling depth below seafloor, CSF = core depth below seafloor. H = hydraulic piston coring system. Time is Universal Time Coordinated.

Table T2. Results from coulometric and CHNS analysis on whole-round squeezecake samples, Hole U1385B.

Core, section	Depth (mbsf)	Calcium carbonate (wt%)	Inorganic carbon (wt%)	Total nitrogen (wt%)	Organic carbon (wt%)	C/N
339-U1385B-						
1H-3	4.475	26.537	3.182	0.068	0.988	14.53
2H-6	15.075	30.214	3.623	0.086	1.037	12.06
3H-6	24.575	29.881	3.583	0.065	0.717	11.03
4H-6	34.075	24.883	2.983	0.044	0.537	12.20
5H-6	43.575	22.635	2.714	0.092	0.986	10.72
6H-6	52.775	38.620	4.630	0.062	0.823	13.27
7H-6	62.575	29.843	3.578	0.073	0.862	11.81
8H-6	71.680	25.301	3.033	0.059	0.537	9.10
9H-6	81.130	22.779	2.731	0.065	2.769	42.60
10H-6	91.175	29.680	3.559	0.065	0.561	8.63
11H-6	100.775	24.666	2.957	0.071	0.683	9.62
12H-6	109.975	29.309	3.514	0.079	0.836	10.58
13H-6	119.315	31.481	3.774	0.082	0.736	8.98
14H-6	129.165	31.859	3.820	0.067	0.260	3.88
15H-5	136.925	28.212	3.383	0.077	0.767	9.96
16H-5	145.175	33.189	3.979	0.075	0.597	7.96

Table T3. Lithology conversions, Site U1385.

Lithology as originally described (still present on visual core descriptions, in smear slide descriptions, and in database)	Lithology as used in text and on summary figures
Major lithologies	
Clayey nannofossil ooze	Nannofossil clay (dark)
Muddy nannofossil ooze	Nannofossil mud (dark)
Nannofossil ooze with clay	Nannofossil clay (light)
Nannofossil ooze with mud	Nannofossil mud (light)
Minor lithologies	
Nannofossil ooze	Muddy nannofossil ooze
Silty nannofossil ooze	Nannofossil silt
Nannofossil sandy silt	Sandy silt with nannofossils
Nannofossil mud	Mud with nannofossils
Mud with biogenic grains	Mud with biogenic grains

Table T4. Abundances of revised lithologies, Hole U1385A.

Section	Mud/silt/sand with biogenics or nannofossils (%)	Nannofossil clay/mud (%)	Clayey or silty nannofossil ooze (%)
1		100	
2		90	10
3	80	20	
4	90	10	
5		100	
6		100	
7		100	
8		85	15
9		90	10
10		100	
11		100	
12		100	
13		100	
14		100	
15		100	
16		100	
17		100	

Table T5. Distribution of potential deformational features, Site U1385.

Hole, core, section, interval (cm)	Depth Top (mbsf)	Depth Bottom (mbsf)	Depth Top (mcd)	Depth Bottom (mcd)	Feature
339-					
U1385E-4H-2, 53–73	22.04	22.24	26.15	26.35	Microfault
U1385A-5H-1, 0–50	30.00	30.05	33.47	33.97	Possible contorted strata
U1385B-4H-4, 71–81	30.31	30.41	34.16	34.26	Possible contorted strata
U1385D-4H-4, 76–80	31.16	31.20	34.15	34.19	Possible contorted strata
U1385B-5H-1, 80–88	35.40	35.48	39.18	39.26	Microfault
U1385D-5H-1, 113–128	36.53	36.68	39.54	39.69	Contorted strata
U1385B-5H-3, 21–30	37.81	37.90	41.59	41.68	Microfault
U1385D-5H-4, 60–70	40.51	40.61	43.52	43.62	Contorted strata
U1385B-7H-5, 51–82	60.11	60.42	66.64	66.95	Contorted strata
U1385B-7H-6, 68–83	61.78	61.93	68.31	68.46	Contorted strata
U1385D-9H-1, 0–16	70.40	70.56	73.51	73.67	Contorted strata
U1385A-10H-2, 40–134	79.40	80.34	87.74	88.68	Microfault
U1385A-10H-3, 100–132	81.51	81.83	89.85	90.17	Microfault
U1385A-10H-4, 58–59	82.62	82.62	90.96	90.97	Microfault
U1385A-11H-2, 62–76	86.12	86.26	95.00	95.14	Microfault
U1385A-12H-1, 98–148	97.48	97.98	105.74	106.24	Microfault
U1385B-11H-5, 38–75	98.06	98.43	108.99	109.36	Contorted strata
U1385E-12H-4, 132–136	97.82	97.86	109.67	109.71	Microfault
U1385E-12H-5, 0–19	98.00	98.19	109.85	110.04	Microfault

Table T6. XRD data, Site U1385.

Hole, core, section, interval (cm)	Depth (mbsf)	Total intensity (counts)	Quartz (counts)	Calcite (counts)	K-feldspar (counts)	Plagioclase (counts)	Dolomite (counts)	Chlorite (counts)	Kaolinite (counts)	Illite (counts)	Smectite (counts)	Hornblende (counts)	Augite (counts)	Pyrite (counts)	Aragonite (counts)
339-															
U1385B-1H-2, 140–150	2.90	44,341	19,879	16,855	429	861	1,343	602	1,364	2,647	361	NA	NA	NA	NA
U1385A-3H-2, 60–61	13.10	52,091	20,015	17,419	617	1,025	2,283	NA	2,679	7,317	419	159	NA	158	NA
U1385B-3H-5, 140–150	23.00	41,626	18,499	14,358	570	1,005	1,132	573	1,349	3,002	459	NA	679	NA	NA
U1385B-4H-5, 140–150	32.50	46,207	19,762	18,775	406	771	1,350	NA	1,302	2,787	383	127	544	NA	NA
U1385B-5H-5, 140–150	42.00	48,424	15,347	26,152	733	500	1,005	457	1,081	2,642	354	31	NA	122	NA
U1385B-6H-5, 140–150	51.50	47,908	14,563	27,572	268	923	619	367	796	2,298	325	61	NA	116	NA
U1385B-7H-5, 140–150	61.00	53,476	23,436	16,719	653	1,339	1,961	925	1,822	5,160	538	202	554	167	NA
U1385B-8H-5, 140–150	70.50	59,250	20,800	22,183	1,113	1,777	1,819	1,096	2,092	7,584	573	83	NA	130	NA
U1385B-9H-5, 140–150	80.04	59,626	33,310	12,729	1,244	1,703	1,647	997	1,631	4,896	375	423	540	131	NA
U1385B-10H-6, 145–150	91.15	61,119	21,685	17,482	812	1,800	4,111	1,600	3,176	8,948	642	160	703	NA	NA
U1385B-11H-5, 145–155	99.17	53,590	19,309	21,243	575	1,093	1,812	1,035	1,689	5,756	566	221	NA	291	NA
U1385B-12H-6, 141–146	109.95	68,946	19,548	21,451	2,497	3,121	2,833	5,174	3,985	9,598	739	NA	NA	NA	NA
U1385B-13H-6, 116–122	119.29	46,503	20,634	19,707	308	801	713	536	1,008	2,152	458	NA	NA	186	NA
U1385B-14H-6, 145–150	129.14	54,521	19,356	18,485	799	1,257	2,842	1,394	2,370	6,664	651	145	558	NA	NA
U1385B-15H-5, 129–134	136.90	49,507	20,278	16,570	401	1,478	1,902	1,201	2,125	4,490	466	102	494	NA	NA
U1385B-16H-5, 145–150	145.15	54,485	22,638	20,406	474	854	1,373	1,131	1,831	4,458	710	159	451	NA	NA

NA = no peak detected.

Table T7. Biostratigraphic datums, Site U1385.

Event	Reference	Age (Ma)	Hole U1385A depth (mbsf)			Hole U1385B depth (mbsf)			Hole U1385D depth (mbsf)			Hole U1385E depth (mbsf)		
			Top	Bottom	Mean	Top	Bottom	Mean	Top	Bottom	Mean	Top	Bottom	Mean
LrO *Emiliania huxleyi* >4 µm	Flores et al., 2010	0.01	2.40	3.07	2.74	0.00	6.14	3.07	0.00	6.95	3.48			
FO *Emiliania huxleyi*	Raffi et al., 2006	0.26	25.90	26.55	26.23	25.44	35.12	30.28	26.28	36.04	31.16			
LO *Pseudoemiliania lacunosa*	Raffi et al., 2006	0.46	49.40	49.48	49.44	53.85	63.65	58.75	51.92	61.42	56.67			
Stilostomella extinction	Kawagata et al., 2005	0.70–0.58	77.83	87.78	82.81	72.68	82.12	77.40	80.37	89.87	85.12			
LO *Reticulofenestra asanoi*	Raffi et al., 2006	0.90	95.40	96.05	95.73	92.07	101.74	96.91	89.87	99.29	94.58			
FO *Reticulofenestra asanoi*	Raffi et al., 2006	1.07	115.70	116.12	115.91	110.19	120.57	115.38	118.76	127.80	123.28			
T paracme *Neogloboquadrina pachyderma* (sin)	Lourens et al., 2004	1.21	116.12	124.67	120.39	120.57	129.90	125.23	118.76	127.80	123.28	111.43	119.13	115.28
LO large *Gephyrocapsa* >5.5 µm	Raffi et al., 2006	1.24	128.99	129.96	129.48	120.57	129.90	125.24	127.80	137.09	132.45			
LO *Helicosphaera sellii*	Raffi et al., 2006	1.25	131.31	131.96	131.64	120.57	129.90	125.24	127.80	137.09	132.45			
B paracme *Neogloboquadrina pachyderma* (sin)	Lourens et al., 2004	1.37							137.09	147.00	142.05	138.59	147.20	142.86

LrO = last regular occurrence, FO = first occurrence, LO = last occurrence, T = top, B = bottom. sin = sinistral, dex = dextral.

Table T8. Abundance of nannofossils, Site U1385. (Continued on next page.).

Core, section	Depth (mbsf)	Preservation	Abundance	*Braarudosphaera bigelowii*	*Calcidiscus leptoporus* (<5 µm)	*Calcidiscus leptoporus* (>8 µm)	*Calcidiscus leptoporus* (5–8 µm)	*Calciosolenia* spp.	*Ceratolithus cristatus*	*Coccolithus pelagicus* spp. *azorinus*	*Coccolithus pelagicus* spp. *braarudii*	*Coccolithus pelagicus* ssp. *pelagicus*	*Emiliania huxleyi* (<4 µm)	*Emiliania huxleyi* (>4 µm)	*Florisphaera profunda*	*Florisphaera profunda* var. *elongata*	*Gephyrocapsa caribbeanica*	medium *Gephyrocapsa* group	*Gephyrocapsa oceanica* (>5 µm)	*Gephyrocapsa oceanica* (<5 µm)	*Gephyrocapsa omega*	small *Gephyrocapsa* spp. (<3 µm)	large *Gephyrocapsa* large (>5.5 µm)
339-U1385A-																							
1H-CC	1.44	G	VA		F	F	C			F	F	F	F		C		R	A	C	C		D	
2H-CC	11.35	G	VA		F	F				C	F	F	F	F	F	R		A	C	F		D	
3H-CC	20.92	G	VA		F	R	F		R	R	F	F	R		C			D	C	C		C	
4H-CC	30.71	G	VA		C	F	C			R	R	R					C	F	F	F		D	
5H-CC	39.97	G	VA		F		F			C	F	F			F		D	F		C		D	
6H-CC	49.48	G	VA		F		F	R		R					C		D	C				D	
7H-CC	58.77	G	VA		F		F								C		D	F				D	
8H-CC	68.64	G	VA		C		C			F	F	F			C		R			R		D	
9H-CC	77.83	G	VA		F		C			R	R	R			F		P	F			R	D	
10H-CC	87.78	G	VA		F		F				R	F			C		F			R	R	D	
11H-CC	96.83	G	VA		F		F								F		F			F	R	D	
12H-CC	106.34	G	VA		F		F					R			F		F			R		D	
13H-CC	116.12	M	VA				F					F			C		F					D	
14H-CC	124.67	G	VA	R			F					R			C		R					D	R
15H-CC	133.88	G	VA		F		F			F	F				R		F					D	C
16H-CC	143.80	G	VA				F			F	F				F		F			F		D	C
17H-CC	151.63	G	VA				F			R	F				F		F			F		D	F
339-U1385B-																							
1H-CC	6.14	G	VA		F		F			R	F	F	A	C	C			C	F	R		A	
2H-CC	16.01	G	VA		F		F			F	F	F	C		F			D	R	R		D	
3H-CC	25.44	G	VA		F		C			F	F	F	F	P	F			C	F	F		D	
4H-CC	35.12	G	VA		F		R				F	F	P		C		C	A	F	F		D	
5H-CC	44.78	G	VA		R	R	F				F	F			C		D	A	F	R			
6H-CC	53.85	G	VA		F		R				F	R			C		D	C				D	
7H-CC	63.65	G	VA		R		C					F			C		D	A	F	F		D	
8H-CC	72.68	G	VA		C		F				F	F			F		R	F	R	R	F	D	
9H-CC	82.13	G	VA		R		P			P	F	F			C		R	C			P	D	
10H-CC	92.07	G	VA		F		F					F			C		R	F		R		D	
11H-CC	101.74	G	A		F		F								C		P					D	
12H-CC	110.19	G	VA		F		F					F			F				P			D	
13H-CC	120.57	G	VA		F		F					R			F							D	
14H-CC	129.90	G	VA							F	F	F			F							D	C
15H-CC	137.76	G	A			F	F			F					F			F				D	C
16H-6	146.30	G	VA			F	F				F	F			F			F		F		D	C
339-U1385D-																							
1H-CC	6.95	M	VA			F	F	F				F	F	R	F			D				D	
2H-CC	16.83	G	VA		F		F				R		F	C	F			A	F			D	
3H-CC	26.28	M	VA		F		C			F	F	F	F	P	F			C				D	
4H-CC	36.04	G	VA		R		R				C	F			C		D	D				D	
5H-CC	42.70	G	VA		F		F				R	R			C		D	C				D	
6H-CC	51.92	G	VA		F	R	F				C				C			A	D			D	
7H-CC	61.42	G	VA		F		F			R	F	F			C			A				D	
8H-CC	70.84	G	VA		F		F				F	F			C		F	C				D	
9H-CC	80.37	G	VA		F		F					R			C			R	C	R		D	
10H-CC	89.87	G	VA		F	R	F					F			C							D	
11H-CC	99.29	G	VA		F	R	F				F	F			C					C		D	
12H-CC	108.84	G	VA		F		F					R			C							D	
13H-CC	118.76	G	VA		F		F								F							D	
14H-CC	127.80	G	VA		F		F			P	R	F			C							D	
15H-CC	137.09	G	VA		F		F					F			C			C				D	A
16H-CC	147.00	G	VA		F	R	F				R	R			F			C	R			D	C

Preservation: G = good, M = moderate. Abundance: D = dominant, VA = very abundant, A = abundant, C = common, F = few, R = rare, P = present. See **"Biostratigraphy"** in the "Methods" chapter (Expedition 339 Scientists, 2013) for abundance and preservation definitions.

Table T8 (continued).

Core, section	Depth (mbsf)	Preservation	Abundance	*Helicosphaera acuta*	*Helicosphaera carteri*	*Helicosphaera hyalina*	*Helicosphaera inversa*	*Helicosphaera sellii*	*Oolithotus* spp.	*Pontosphaera* spp.	*Pseudoemiliania lacunosa*	*Reticulofenestra asanoi* (>6 µm)	*Reticulofenestra asanoi* (<6 µm)	*Rhabdosphaera* spp.	*Scyphosphaera apsteinii*	*Syracosphaera* spp.	*Thoracosphaera* spp.	*Umbilicosphaera sibogae*	Reworking
339-U1385A-																			
1H-CC	1.44	G	VA		C				R	F				R	F			C	F
2H-CC	11.35	G	VA		C				R	R								F	C
3H-CC	20.92	G	VA		C				F	F				R		C		C	F
4H-CC	30.71	G	VA		C		R		R	R				R		F		F	C
5H-CC	39.97	G	VA		C				R	R				F		C		F	F
6H-CC	49.48	G	VA		F		R				P			P			R		R
7H-CC	58.77	G	VA	R							F					R		R	F
8H-CC	68.64	G	VA		C					R	A								C
9H-CC	77.83	G	VA							R	C			R		F		R	F
10H-CC	87.78	G	VA		F					F	F			F		F			F
11H-CC	96.83	G	VA		F					F	F	C	F	F		F	R		F
12H-CC	106.34	G	VA		F					R	C	A							F
13H-CC	116.12	M	VA		F			R		R	C		F	R		F		R	C
14H-CC	124.67	G	VA	R				R		F	F		F	F		F		R	F
15H-CC	133.88	G	VA					R		C	F		F						C
16H-CC	143.80	G	VA	R	F			R		F	F		F	F		F			C
17H-CC	151.63	G	VA	R	C			R	R		F					F		R	F
339-U1385B-																			
1H-CC	6.14	G	VA		C				R					R		F		R	C
2H-CC	16.01	G	VA		C				R	F						C			F
3H-CC	25.44	G	VA						R					R	R	F			F
4H-CC	35.12	G	VA			P										R			F
5H-CC	44.78	G	VA		R					R				R	C				C
6H-CC	53.85	G	VA		F						P							F	F
7H-CC	63.65	G	VA		C				F		C					F		R	F
8H-CC	72.68	G	VA		C						C					F		F	F
9H-CC	82.13	G	VA		C					P	C					R			C
10H-CC	92.07	G	VA		F					F		R	R	R		F			C
11H-CC	101.74	G	A		C						A	A	C			R			F
12H-CC	110.19	G	VA		C					F	A	C	C			F			F
13H-CC	120.57	G	VA		F					R	R		C	F		F		F	R
14H-CC	129.90	G	VA					R	F		C		C	R		R		R	C
15H-CC	137.76	G	A					F	F	F	C		C	F		F		F	F
16H-6	146.30	G	VA		F			F		F	C		C	F		F		F	F
339-U1385D-																			
1H-CC	6.95	M	VA		F					R						F			C
2H-CC	16.83	G	VA		F				R	R				R		F			C
3H-CC	26.28	M	VA		F				R					R		R			F
4H-CC	36.04	G	VA		C				R	P				F		C		R	F
5H-CC	42.70	G	VA		F					R	P			F		C		F	F
6H-CC	51.92	G	VA		C		F			R	P			R		F		R	F
7H-CC	61.42	G	VA		C						F			R		F		R	F
8H-CC	70.84	G	VA		C					R	C			R		F		R	F
9H-CC	80.37	G	VA		F					F	C		F			R			F
10H-CC	89.87	G	VA		F					R	C	R	R	R		R		R	F
11H-CC	99.29	G	VA		F					F	C	C	A			F			F
12H-CC	108.84	G	VA		F					C	C	C	C			R			F
13H-CC	118.76	G	VA		F					R	A	F	C	R					F
14H-CC	127.80	G	VA		F					R	F	A	D	F					C
15H-CC	137.09	G	VA		F			F		R	F		C			F			F
16H-CC	147.00	G	VA	P				F		F	F		C			F			C

Table T9. Abundance of planktonic foraminifers, Site U1385. (Continued on next page.)

Core, section	Depth (mbsf) Top	Depth (mbsf) Bottom	Pteropod abundance	Planktonic foraminifer abundance	Planktonic foraminifer preservation	*Beella digitata*	*Globigerina bulloides*	*Globigerina calida*	*Globigerina falconensis*	*Globigerinella siphonifera*	*Globigerinita glutinata*	*Globigerinoides conglobatus*	*Globigerinoides ruber* (pink)	*Globigerinoides ruber* (white)	*Globigerinoides sacculifer*	*Globigerinoides trilobus*	*Globorotalia crassaformis* s.l. (dex)	*Globorotalia crassaformis* s.l. (sin)	*Globorotalia hirsuta* (dex)	*Globorotalia hirsuta* (sin)	*Globorotalia inflata*	*Globorotalia scitula* (dex)	*Globorotalia scitula* (sin)	*Globorotalia truncatulinoides* (dex)	*Globorotalia truncatulinoides* (sin)	*Globoturborotalita rubescens*	*Globoturborotalita tenella*	*Neogloboquadrina atlantica* (dex)	*Neogloboquadrina atlantica* (sin)	*Neogloboquadrina dutertrei*	*Neogloboquadrina pachyderma* (dex)	*Neogloboquadrina pachyderma* (sin)	*Orbulina universa*	*Pulleniatina obliquiloculata*	*Sphaeroidinella dehiscens*	*Turborotalita humilis*	*Turborotalita iota*	*Turborotalita quinqueloba*
339-U1385A-																																						
1H-CC	1.39	1.44	B	D	G		A	P	F	F	P	P	R	A		P		R		R	A	P		R	F					P	F	P	F			P		P
2H-CC	11.30	11.35	B	D	M		A	P	A	F			R	F				P		R	A	R		P	F	P				P	P		R	P			P
3H-CC	20.87	20.92	B	D	M		A			P	R	P	F	A	P	R		P	R	B	A	R	P	P	F	P					A		F		P			
4H-CC	30.66	30.71	B	D	G		A	P	A	P				P							F			R		P	P				F		F					P
5H-CC	39.92	39.97	B	D	G		A		F					P					P		R	P		R		P	P			F	R		R		P			F
6H-CC	49.43	49.48	B	D	M	P	F			P				F							A	R	P	A	P						D		F					P
7H-CC	58.71	58.77	B	D	M		F				P		P	P	B			P			F	P		P							D	P	R					
8H-CC	68.58	68.64	B	D	M	P	D			P	P		R	F			B	P			R	P		P	P						D	P	R		P			P
9H-CC	77.78	77.83	B	D	M		A			P	P			P				R			F	R	P	R	R					P	A	R	F					P
10H-CC	87.73	87.78	B	D	G		A			P	P			P				P			F	R	P	R	R						F	R	A					R
11H-CC	96.78	96.83	B	D	G		F	P		P	P			P			R				A	P	P	P							D	F	F					R
12H- 4	102.68	102.70	B	D	G		F			R	P			R				P			F	P		R	P						A	R	R					
12H-CC	106.29	106.34	B	D	G		A	P	R	P	P			R							A	R	P	F	F						A	F	F					R
13H-CC	116.07	116.12	B	D	G		F	P		P	P							R			F	R		F							A	A	F					R
14H-CC	124.62	124.67	B	D	G		A	P		R	P			P				R			F	R		F							D		R					
15H-CC	133.83	133.88	B	D	G		F			P	P			P				F			A	R		F							D	P	F					
16H-CC	143.75	143.80	B	D	G		F			P	P			R				R			F	P	P	R				R			D		F					P
17H-CC	151.58	151.63	B	D	M		A			P	P			F				F			A	P		P				P			F		F					R
339-U1385B-																																						
1H-CC	6.09	6.14	B	D	G		D			P	P			P							F	F		P	P						D	F	P					R
2H-CC	15.96	16.01	B	D	G		A	P		P	P	P		P							A	P		F							F		F					R
3H-CC	25.39	25.44	B	D	G		F	P		P	P			R			P		P		F		P	P		P	P					A	F					P
4H-CC	35.07	35.12	B	D	M		D		P	P				P			P				F	R		P	P						A	P	R				P	P
5H-CC	44.73	44.78	B	D	G		A			P	P			R				P			F	F		P	P					P	A	P	A			P	P	P
6H-CC	53.80	53.85	B	D	G		F		F																P	P					D	R	R			P	R	R
7H-CC	63.60	63.65	B	D	G		A		P	P				R				R			A				R						F	P	R					P
8H-CC	72.63	72.68	B	D	G		A	P		P	P			P			P	P			A	P		R	P						A							
9H-CC	82.08	82.13	B	D	M		F		R		P											P									F	D	F					R
10H-CC	92.02	92.07	B	D	G		P			P	P			P							R	P		R	P						A	A	R					
11H-CC	101.69	101.74	B	D	G		A			P	P			F							F	R		F	R						F	R	P	A				P
12H-CC	110.16	110.19	B	D	G		F			P	P			R				P			R	R		R							F	R	P	P				
13H-CC	120.52	120.57	B	D	G		A			R	P			R	P			R			R			R							A	R	R	P				
14H-CC	129.85	129.90	B	D	G		F			R				R			P	P			F	P		R	P						A	P	R					
15H-CC	137.71	137.76	B	D	G		A	P		P				F				P			F	P		P				R			F		R					P
16H- 6	146.13	146.30	B	D	G		A			P	P	P		R							A	P		R				P			R		R	P				P
339-U1385D-																																						
1H-CC	6.9	6.95	B	D	G		A			P	P			P							F	F		P	R						A	R	R					P
2H-CC	16.78	16.83	B	D	G		A		P	R		P		P			P				F	P		R	R						R		R					P

Table T9 (continued).

Core, section	Depth (mbsf) Top	Depth (mbsf) Bottom	Pteropod abundance	Planktonic foraminifer abundance	Planktonic foraminifer preservation	*Beella digitata*	*Globigerina bulloides*	*Globigerina calida*	*Globigerina falconensis*	*Globigerinella siphonifera*	*Globigerinita glutinata*	*Globigerinoides conglobatus*	*Globigerinoides ruber* (pink)	*Globigerinoides ruber* (white)	*Globigerinoides sacculifer*	*Globigerinoides trilobus*	*Globorotalia crassaformis* s.l. (dex)	*Globorotalia crassaformis* s.l. (sin)	*Globorotalia hirsuta* (dex)	*Globorotalia hirsuta* (sin)	*Globorotalia inflata*	*Globorotalia scitula* (dex)	*Globorotalia scitula* (sin)	*Globorotalia truncatulinoides* (dex)	*Globorotalia truncatulinoides* (sin)	*Globoturborotalita rubescens*	*Globoturborotalita tenella*	*Neogloboquadrina atlantica* (dex)	*Neogloboquadrina atlantica* (sin)	*Neogloboquadrina dutertrei*	*Neogloboquadrina pachyderma* (dex)	*Neogloboquadrina pachyderma* (sin)	*Orbulina universa*	*Pulleniatina obliquiloculata*	*Sphaeroidinella dehiscens*	*Turborotalita humilis*	*Turborotalita iota*	*Turborotalita quinqueloba*
3H-CC	26.23	26.28	B	D	G		A		P	P				P			P				F	P		R	R						R		R				P
4H-CC	35.99	36.04	B	D	G		A		P	P				P			P				A	P		R	R						R		R				P
5H-CC	42.65	42.7	B	D	G		D			P	P	P	F	A							A	P		R	P						A		P				P
6H-CC	51.87	51.92	B	D	G		A				P			A		P	P				A	P		R		P					A		F	P			P
7H-CC	61.37	61.42	B	D	G	P	A			R	P			F			P		P		F	R		R							A		F				R
8H-CC	70.81	70.84	B	D	G		A			P				F		P					F	P		P							F	R	R				R
9H-CC	80.32	80.37	B	D	G		F			R	P			P			P	R			F	P		P							R	R	F				
10H-CC	89.83	89.87	B	D	G		A			R	P			P			P				F	P		P							R	R	R				P
11H-CC	99.26	99.29	B	D	G		A		P	P				R			P				F	P		R								R	R				P
12H-CC	108.79	108.84	B	D	G		D			R		P		R							R			P							R	P	R				P
13H-CC	118.71	118.76	B	D	G		A	P		R				R							A	P		P							A	P	P				P
14H-CC	127.75	127.8	B	D	G		R	P		P				F				P		P	F	P		R							A		P	F			
15H-CC	137.04	137.09	B	D	G		F	P		R				R							F	P		P				P			A	P	P				
16H-CC	146.95	147	B	D	G		F			P		P		P							F	F		P				R			A	R	R				R
339-U1385E-																																						
13H-CC	111.38	111.43	B	D	G		A		P	F	P			A			P	P	P		F	P	P	P		P					A	R	P				
14H- 8	119.11	119.13	B	D	G		A			F				F			P	P			F	P	P	R	P						F		R	P			
15H-CC	128.55	128.60	B	D	G		A		P	F	P			A			P	P			F			P	P						A		P	P			P
16H-CC	138.55	138.59	B	D	G		A		P	R		P		A				P			F	P			P			P			R		R				
17H-CC	147.15	147.20	B	D	G		A			P	P	P		R							A	P		P				P			A	R	F				P

Abundance: D = dominant, A = abundant, C = common, F = few, P = present, R = rare, B = barren. Preservation: G = good, M = moderate. sin = sinistral, dex = dextral. See **"Biostratigraphy"** in the "Methods" chapter (Expedition 339 Scientists, 2013) for abundance and preservation definitions.

Table T10. Abundance of benthic foraminifers, Hole U1385A. (Continued on next two pages.)

Core, section	Depth (mbsf) Top	Depth (mbsf) Bottom	Preservation	Abundance	*?Adelosina* spp.	Agglutinated indet.	*Amphicoryna* spp.	*Anomalinoides* spp.	*Biloculinella* spp.	*Bolivina/Brizalina* spp.	*Brizalina alata*	*Brizalina* cf. *difformis*	*Brizalina dilatata* s.l.	*Brizalina earlandi*	*Brizalina quadrilatera*	*Bulimina aculeata*	*Bulimina alazanensis*	*Bulimina elongata*	*Bulimina striata* gr.	*Bulimina* spp.	*Cassidulina laevigata/teretis*	*Cassidulinoides* spp.	*Chilostomella oolina*	*Chrysalogonium calomorphum*	*Cibicides lobatulus*	*Cibicides/Cibicidoides* spp.	*Cibicidoides wuellerstorfi*	*Dentalina* spp.	*Eggerella bradyi*	Elphidid taxa	*Epistominella exigua*	*Fissurina alveolata*	*Fissurina* cf. *radiata*	*Fissurina* cf. *staphylleana*	*Fissurina* spp.	*Frondicularia sagittula*	*Fursenkoina complanata*	*Fursenkoina* spp.	*?Cavelinopsis* spp.	*Glandulina* spp.	*Globobulimina affinis*	*Globobulimina* spp.	*Globocassidulina subglobosa*	*Gyroidinoides soldanii*	*Gyroidinoides* spp.	*?Hanzawaia* spp.	*Hanzawaia* spp.	*Haynesina* spp.	*Heterolepa* spp.
339-U1385A-																																																	
1H-CC	1.39	1.44	G	R	A				P				F	P					P		P					F	R				P	R				R				R			R		P		P		
2H-CC	11.3	11.35	G	R								P				A			R				R			P	P				R									F			P						
3H-CC	20.87	20.92	G	P		P							F	P			R		R	P	F		P			R					P													P					
4H-CC	30.66	30.71	G	R										P		R	P		A		R				P						P			P	P					P		A			P				
5H-CC	39.92	39.97	G	R					R							P	R		P		R					R	R				R						R			R				R		P			
6H-CC	49.43	49.48	G	R	P										P		R		P		A		R			R					F									R		F	R						
7H-CC	58.71	58.77	G	F					P	F	P		P			P					A				P	R					A				P			P		R			R	R		P			
8H-CC	68.58	68.64	G	R											R			R							P	A	R				A				P					A		R	R						
9H-CC	77.78	77.83	G	R	P		P			R		P		F	R	P			P		F	P			R	F	R				F		P					F		R		R	R						
10H-CC	87.73	87.78	G	R									P		P		R				R					A	R				R							F		R			P						
11H-CC	96.78	96.83	G	R	P								P				R				R					F	R		P		R						F			P			P						
12H-CC	106.29	106.34	G	F									P	R					A												F					R	F			F			P						
13H-CC	116.07	116.12	G	R									R	P					R							R					F						F			R			R						
14H-CC	124.62	124.67	G	R							R		P				P									R	P		P		R						R	P			P		R					P	
15H-CC	133.83	133.88	G	R				P		P	P									R					P	P	R	F			P						R				P	R							
16H-CC	143.75	143.8	G	P						P			P						R	P				P		P	R	R		P	R									P	R							
17H-CC	151.54	151.59	G	R									R					P			P					R	R				R				R								P					P	

Preservation: G = good. Abundance: A = abundant, F = few, P = present, R = rare. See **"Biostratigraphy"** in the "Methods" chapter (Expedition 339 Scientists, 2013) for abundance and preservation definitions.

Table T10 (continued). (Continued on next page.)

Core, section	Depth (mbsf) Top	Depth (mbsf) Bottom	Preservation	Abundance	*Hoeglundina elegans*	Hyaline indet.	*Hyalinonetrion gracillimum*	*Hyperammina* spp.	*Karreriella bradyi*	*Lagena hispidula*	*Lagena* spp.	*Laticarinina pauperata*	*Martinottiella communis*	*Martinottiella* spp.	*Melonis barleeanus*	*Melonis pompilioides*	*Melonis* spp.	Miliolid indet.	*Myllostomella fijiensis*	Nodosariidae indet.	*Nonionella turgida*	Nonionidae indet.	*Oolina* spp.	*Oridorsalis umbonatus*	*Parafissurina* spp.	*Pleurostomella alternans*	*Porosononion* sp.	*Praeglobobulimina ovata*	*Proxifrons inaequalis*	*Pullenia bulloides*	*Pullenia quinqueloba*	*Pyrgo* spp.	*?Pyrulina angusta*	*Quinqueloculina* spp.	*Rhizammina* spp.	*Rosalina* spp.	*Rotalia* spp.	*Saracenaria* spp.	*Sigmoilopsis schlumbergeri*	*Siphonodosaria hispidula*	*Siphonodosaria ketienziensis*	*Siphonodosaria lepidula*	*Siphonodosaria* sp. 1	*Siphouvigerina ampullacea*	*Sphaeroidina bulloides*	*Spiroloculina excavata*	*Spiroloculina* cf. *tenuiseptata*	*Spiroloculina* spp.	*Spirophtalmidium* cf. *actuimargo*
339-U1385A-																																																
1H-CC	1.39	1.44	G	R	R											R				P			P	P							F		P											F			R
2H-CC	11.3	11.35	G	R	A	R									P	R								P	P			R		P		R		A				R								
3H-CC	20.87	20.92	G	P	P													R		P				P						P		R			R			F								
4H-CC	30.66	30.71	G	R			P				R					P	P	P						P																							
5H-CC	39.92	39.97	G	R	P										F	R				P				P						R				R		P		F								
6H-CC	49.43	49.48	G	R											P	P				P				P									R						P					R			
7H-CC	58.71	58.77	G	F		P				P					P	R								P						P		P	P					P					R		P	
8H-CC	68.58	68.64	G	R	P		P				R				R	A						R		P						P		R		P				R								
9H-CC	77.78	77.83	G	R							P		R			F					P	R		P						R		P	R			P	R					F		P		
10H-CC	87.73	87.78	G	R	R				R						R					R				P								F	P		P			P								
11H-CC	96.78	96.83	G	R	R			P									P			P				P		P							P	P					R		R			R	P		
12H-CC	106.29	106.34	G	F	R				P		P					R				R				P		P			P	P	P	P	P								F					
13H-CC	116.07	116.12	G	R			P												P	P		P		P		R			P			P	P					R	R	R	A					
14H-CC	124.62	124.67	G	R	P							P				P	P		R	R												R		P						R	A						
15H-CC	133.83	133.88	G	R					P				P				P	P	R	P							P											R			P	A	P		F			
16H-CC	143.75	143.8	G	P					P								P		A	R							P													P	F	R					
17H-CC	151.54	151.59	G	R	P		P					P		P			P		A	R		P				P			P		P									P	F	R					

Table T10 (continued).

Core, section	Depth (mbsf) Top	Depth (mbsf) Bottom	Preservation	Abundance	*Spiroplectammina* spp.	*Stainforthia* spp.	Stillostomellidae indet.	*Stilostomella* spp.	*Textularia pseudogramen*	*Textularia* spp.	*Trifarina angulosa*	*Trifarina bradyi*	*Triloculinella obliquinodus*	*Uvigerina mediterranea*	*Uvigerina peregrina*	*Uvigerina* spp.	*Vaginulinopsis* spp.
339-U1385A-																	
1H-CC	1.39	1.44	G	R													
2H-CC	11.3	11.35	G	R													
3H-CC	20.87	20.92	G	P													
4H-CC	30.66	30.71	G	R											R		
5H-CC	39.92	39.97	G	R										P	P	R	
6H-CC	49.43	49.48	G	R								P			R		
7H-CC	58.71	58.77	G	F													
8H-CC	68.58	68.64	G	R												P	
9H-CC	77.78	77.83	G	R							P						P
10H-CC	87.73	87.78	G	R											F	R	
11H-CC	96.78	96.83	G	R						P					P	P	
12H-CC	106.29	106.34	G	F	P		P	P					P	P	A		
13H-CC	116.07	116.12	G	R					P					P	P		
14H-CC	124.62	124.67	G	R													
15H-CC	133.83	133.88	G	R			P	P							A		
16H-CC	143.75	143.8	G	P				P									
17H-CC	151.54	151.59	G	R				P									

Table T11. Abundance of ostracods, Site U1385.

Core, section	Depth (mbsf) Top	Depth (mbsf) Bottom	Preservation	Abundance	*Ambocythere* sp.	*Argilloecia acuminata*	*Argilloecia robinwhatleyi*	*Australoecia posteroacuta*	*Bairdoppilata vitrix*	*Bradleya dictyon*	*Bythoceratina scaberrima*	*Cytherella robusta*	*Cytheropteron alatum*	*Cytheropteron carolinae*	*Cytheropteron syntomoalatum*	*Cytheropteron* sp. A	*Cytheropteron* sp. B	*Echinocythereis echinata*	*Hennyhowella asperrima*	*Krithe* spp.	*Legitimocythere acanthoderma*	*Loxoconchidea minima*	*Poseidonamicus major*	*Propontocypris trigonella*	*Pseudocythere caudata*
339-U1385A-																									
1H-CC	1.39	1.44	M	R												2				7					
2H-CC	11.30	11.35	M	R																5					
3H-CC	20.87	20.92	G	R																		1			
4H-CC	30.66	30.71		B																					
5H-CC	39.92	39.97	P	R																2					
6H-CC	49.43	49.48		B																					
7H-CC	58.71	58.77	M	R		1														2					
8H-CC	68.58	68.64	G	R															1	5		2			1
9H-CC	77.78	77.83		B																					
10H-CC	87.73	87.78	G	R	1						1						1			4					
11H-CC	96.78	96.83	M	C						1					1		1		2	10					
13H-CC	116.07	116.12		B																					
14H-CC	124.62	124.67	G	R								2							1	2					
15H-CC	133.83	133.88	M	R		1		1																	
16H-CC	143.75	143.80	M	R																1					
17H-CC	151.58	151.63		B																					
339-U1385B-																									
1H-CC	6.09	6.14	G	R														1		15					
2H-CC	15.96	16.01	G	R		1							1							7			1		
3H-CC	25.39	25.44	G	R										2					2	9		2			
4H-CC	35.07	35.12	G	R																20					
5H-CC	44.73	44.78	M	R														1		15					
6H-CC	53.8	53.85	P	B																					
7H-CC	63.6	63.65	P	R																1					
8H-CC	72.63	72.68	M	R					1											8					
9H-CC	82.08	82.13		B																					
10H-CC	92.02	92.07	M	R																10					
11H-CC	101.69	101.74	M	R			1	1												5	1				
12H-CC	110.16	110.19	M	R																4					
13H-CC	120.52	120.57	M	R																2					
14H-CC	129.85	129.9	M	R															2	11					
15H-CC	137.71	137.76	G	R		1													1	1					
16H-CC	146.13	146.3	G	R		3		2							1				3	8					

Preservation: G = good, M = moderate, P = poor. Abundance: C = common, R = rare, B = barren. See "Biostratigraphy" in the "Methods" chapter (Expedition 339 Scientists, 2013) for abundance and preservation definitions.

Table T12. Abundance of pollen and spores, Hole U1385A.

Core, section	Depth (mbsf) Top	Depth (mbsf) Bottom	Preservation	Abundance	Exotic counted	*Alnus*	*Anthemis* type	*Artemisia*	*Asphodelus*	*Aster* type	*Betula*	Brassicaceae	*Calluna*	*Carpinus*	*Cedrus*	Chenopodiaceae	*Cistus*	*Corylus*	Cupressaceae	*Ephedra distachya* type	*Ephedra fragilis* type	Ericaceae	*Euphorbia*	*Fraxinus excelsior* type	*Hedera helix*	*Isoetes*	Monolete psilate	*Olea*	Phillyrea	*Pinus*	*Plantago*	Plumbaginaceae	Poaceae	*Quercus* deciduous type	*Quercus* evergreen type	Ranunculaceae	*Taraxacum*	*Taxus*	Trilete ornamented	Trilete psilate	Unidentifiables	Valerianaceae
339-U1385A-																																										
1H-CC	1.39	1.44	G	A	101	R		C								C				R		R	R	R		C	F	R	F	A			C	C	C		A	R		F	F	
2H-CC	11.30	11.35	M	A	75					F	F						F		F	F		C							A			F		F		F				F	
3H-CC	29.87	20.92	G	C	146										R						F	F				F			F				R	R		F			R	F	
5H-CC	36.56	36.61	M	A	100			F	F	F											F					F			C				F							F	
6H-CC	49.43	49.48	M	A	190			F		R		R				R			R	F		R						R	F	F		R	F			C				F	
10H-CC	87.73	87.78	M	A	108			C		F	R	R				C				F	F	C			R	C		R	A	F		C	C	F	R	C				C	
11H-CC	96.78	96.83	M	A	109	R		F		F		F		R		R		R	R			F				F		R	A			F	F	F		C			R	C	R
13H-CC	116.27	116.32	M	A	112		R	F		F		R				R				C	R	F				F			A		R	F		R		C				F	
16H-CC	143.75	143.80	P	A	104			F		F		F									F	F				F	F	R	A	F		F	C	F		C		C		A	

Preservation: G = good, M = moderate, P = poor. Abundance: A = abundant, C = common, F = few, R = rare. See **"Biostratigraphy"** in the "Methods" chapter (Expedition 339 Scientists, 2013) for abundance and preservation definitions.

Table T13. FlexIt tool core orientation data, Site U1385.

Core	Orientation angle (°)	Orientation standard deviation (°)
339-U1385A-		
4H	132	0.7
5H	250	0.8
6H	238	0.6
7H	352	0.4
8H	58	0.5
9H	353	0.8
10H	8	1.0
11H	259	0.3
12H	171	0.3
13H	315	0.4
14H	280	0.1
15H	60	21.4
16H	25	0.4
17H	187	1.2
339-U1385B-		
4H	172	1.98
5H	83	0.50
6H	107	0.37
7H	243	1.78
8H	290	0.92
9H	146	1.05
10H	208	0.21
11H	38	0.29
12H	316	0.43
13H	178	0.16
14H	127	0.24
15H	297	0.23
16H	8	0.82
339-U1385D-		
4H	72	0.7
5H	171	0.3
6H	235	0.5
7H	273	0.1
8H	117	0.4
9H	327	0.4
10H	23	0.2
11H	183	0.9
12H	278	0.3
13H	305	0.3
14H	350	0.4
15H	138	0.4
16H	325	0.5
339-U1385E-		
5H	86	0.4
6H	194	0.6
7H	302	0.6
8H	324	0.7
9H	291	0.9
10H	58	0.5
11H	90	0.8
12H	83	0.4
13H	180	0.3
14H	324	0.4
15H	11	0.4
16H	109	0.2
17H	309	0.3

Table T14. Disturbed intervals, Site U1385. (Continued on next two pages.)

Core, section, interval (cm)	Drilling disturbance	
	Intensity	Comment
339-U1385A-		
1H-1, 0–6	Moderate	Slightly soupy mudline
1H-1, 106–107	Void	Crack
1H-1, 111–113	Void	Crack
2H-1, 0–18	Moderate	Moderately soupy core top
2H-6, 139–144	High	IW tube sample
2H-6, 144–150	Void	MBIO
3H-1, 0–120	High	Soupy core top
3H-6, 140–150	High	IW tube sample
4H-1, 0–46	High	Soupy core top
4H-6, 140–144	High	IW tube sample
4H-6, 144–150	Void	MBIO
5H-1, 0–60	High	Disturbed core top
5H-6, 141–150	High	IW tube sample
6H-1, 0–47	Moderate	Disturbed core top
6H-6, 140–150	High	IW tube sample
7H-1, 0–9	High	Disturbed core top
7H-6, 112–122	High	IW tube sample
8H-1, 0–2	Moderate	Disturbed core top
8H-6, 140–145	High	IW tube sample
8H-6, 145–150	Void	MBIO
9H-1, 0–7	Moderate	Disturbed core top
9H-6, 144–154	High	IW tube sample
10H-1, 0–1	Moderate	Disturbed core top
10H-6, 148–153	High	IW tube sample
10H-6, 153–158	Void	MBIO
11H-1, 0–35	High	Disturbed core top
11H-6, 148–153	High	IW tube sample
12H-1, 0–20	High	Disturbed core top
12H-6, 117–120	High	IW tube sample
12H-6, 120–125	Void	MBIO
13H-1, 0–6	High	Disturbed core top
13H-6, 145–153	High	IW tube sample
13H-7, 58–65	High	Void
14H-1, 0–5	High	Disturbed core top
14H-5, 148–153	High	WR
15H-1, 0–24	Moderate	Disturbed core top
15H-5, 150–155	High	IW tube sample
16H-1, 0–73	High	Disturbed core top
16H-5, 146–151	High	WR
17H-1, 0–26	High	Disturbed core top
17H-4, 150–155	High	IW tube sample
339-U1385B-		
1H-1, 0–3	High	Soupy mudline
1H-1, 94–150	High	Soupy
1H-2, 0–7	Moderate	Soupy
1H-2, 60–150	High	Flow-in
1H-3, 0–112	High	Flow-in
2H-1, 0–17	Moderate	Disturbed core top
2H-1, 17–70	Moderate	Flow-in
2H-1, 141–150	High	IW tube sample
2H-2, 143–150	High	IW tube sample
2H-3, 143–150	High	IW tube sample
2H-4, 143–150	High	IW tube sample
2H-5, 139–150	High	IW tube sample
2H-6, 145–150	Void	WR
2H-7, 63–74	High	IW tube sample
3H-1, 0–42	High	Disturbed core top
3H-1, 140–150	High	IW tube sample
3H-2, 142–150	High	IW tube sample
3H-3, 142–150	High	IW tube sample
3H-4, 142–150	High	IW tube sample
3H-5, 141–150	High	IW tube sample
3H-6, 145–150	Void	WR
4H-1, 0–39	High	Disturbed core top
4H-1, 139–150	High	IW tube sample
4H-2, 141–150	High	IW tube sample
4H-3, 141–150	High	IW tube sample
4H-4, 142–150	High	IW tube sample

Table T14 (continued). (Continued on next page.)

Core, section, interval (cm)	Drilling disturbance	
	Intensity	Comment
4H-5, 141–150	High	IW tube sample
4H-6, 145–150	Void	WR
5H-1, 0–35	High	Disturbed core top
5H-1, 141–150	High	IW tube sample
5H-2, 141–150	High	IW tube sample
5H-3, 141–150	High	IW tube sample
5H-4, 141–150	High	IW tube sample
5H-5, 141–150	High	IW tube sample
5H-6, 145–150	Void	WR
6H-1, 0–1	Moderate	Disturbed core top
6H-1, 142–150	High	IW tube sample
6H-2, 142–150	High	IW tube sample
6H-3, 140–150	High	IW tube sample
6H-4, 141–151	High	IW tube sample
6H-5, 141–150	High	IW tube sample
7H-1, 0–19	High	Disturbed core top
7H-1, 141–150	High	IW tube sample
7H-2, 141–150	High	IW tube sample
7H-3, 141–150	High	IW tube sample
7H-4, 141–150	High	IW tube sample
7H-5, 146–152	High	IW tube sample
7H-6, 145–150	Void	WR
8H-1, 0–27	High	Disturbed core top
8H-1, 141–150	High	IW tube sample
8H-2, 141–150	High	IW tube sample
8H-3, 141–150	High	IW tube sample
8H-4, 144–150	High	IW tube sample
8H-5, 141–152	High	IW tube sample
8H-6, 105–111	Void	WR
9H-1, 0–9	High	Disturbed core top
9H-1, 141–150	High	IW tube sample
9H-2, 144–152	High	IW tube sample
9H-3, 141–154	High	IW tube sample
9H-4, 146–154	High	IW tube sample
9H-5, 145–153	High	IW tube sample
9H-6, 100–106	Void	WR
10H-1, 0–5	Moderate	Disturbed core top
10H-1, 141–150	High	IW tube sample
10H-2, 142–151	High	IW tube sample
10H-3, 143–152	High	IW tube sample
10H-4, 142–151	High	IW tube sample
10H-5, 146–155	High	IW tube sample
10H-6, 148–154	Void	WR
11H-1, 0–1	Moderate	Disturbed core top
11H-1, 144–151	High	IW tube sample
11H-2, 145–151	High	IW tube sample
11H-3, 150–154	High	IW tube sample
11H-4, 148–154	High	IW tube sample
11H-5, 34–77	High	Flow-in
11H-5, 148–155	High	IW tube sample
11H-6, 150–155	Void	WR
12H-1, 0–7	Moderate	Disturbed core top
12H-1, 139–150	High	IW tube sample
12H-2, 140–150	High	IW tube sample
12H-3, 30–32	Void	Void
12H-3, 145–152	High	IW tube sample
12H-4, 141–150	High	IW tube sample
12H-5, 142–150	High	IW tube sample
12H-6, 141–150	Void	WR
13H-1, 0–5	Moderate	Disturbed core top
13H-1, 141–150	High	IW tube sample
13H-2, 143–150	High	IW tube sample
13H-3, 143–151	High	IW tube sample
13H-4, 142–150	High	IW tube sample
13H-5, 147–153	High	IW tube sample
13H-6, 115–122	Void	WR
13H-7, 52–72	Moderate	Disturbed
14H-1, 0–11	Mild	Disturbed core top
14H-1, 141–150	High	IW tube sample
14H-2, 145–151	High	IW tube sample

Table T14 (continued).

Core, section, interval (cm)	Drilling disturbance	
	Intensity	Comment
14H-3, 145–151	High	IW tube sample
14H-4, 145–153	High	IW tube sample
14H-5, 148–153	High	IW tube sample
14H-6, 146–152	Void	WR
14H-7, 49–51	Void	Void
15H-1, 0–13	Moderate	Disturbed core top
15H-1, 140–150	High	IW tube sample
15H-2, 147–152	High	IW tube sample
15H-3, 147–152	High	IW tube sample
15H-4, 146–152	High	IW tube sample
15H-5, 130–135	Void	WR
16H-1, 0–7	Mild	Disturbed core top
16H-1, 144–151	High	IW tube sample
16H-2, 146–152	High	IW tube sample
16H-3, 148–155	High	IW tube sample
16H-4, 147–153	High	IW tube sample
16H-5, 149–154	Void	WR
16H-6, 83–93	High	Disturbed
16H-7, 49–51	Void	Void
339-U1385C-		
1H-1, 0–38	High	Disturbed core top
1H-1, 124–130	Void	Void
1H-2, 101–104	Void	Void
339-U1385D-		
1H-1, 0–1	Moderate	Slightly soupy mudline
2H-1, 0–1	Moderate	Disturbed core top
3H-1, 0–26	High	Disturbed core top
4H-1, 0–39	High	Disturbed core top
5H-1, 0–65	High	Disturbed core top
6H-1, 0–50	Moderate	Disturbed core top
6H-6, 61–62	Void	Crack
6H-6, 112–114	Void	Crack
7H-1, 0–25	Mild	Disturbed core top
8H-1, 0–8	High	Disturbed core top
9H-1, 0–15	Mild	Disturbed core top
10H-1, 0–25	Mild	Disturbed core top
11H-1, 0–15	Mild	Disturbed core top
12H-1, 0–8	Mild	Disturbed core top
13H-1, 0–1	Mild	Disturbed core top
14H-1, 0–5	Moderate	Disturbed core top
15H-1, 0–15	Moderate	Disturbed core top
16H-1, 0–28	Moderate	Disturbed core top
16H-3, 26–27	Void	Crack
339-U1385E-		
1H-1, 0–1	Moderate	Slightly soupy mudline
2H-1, 0–152	High	Flow-in
2H-2, 0–2	Moderate	Flow-in
2H-2, 148–151	Void	Void
2H-3, 44–45	Void	Crack
3H-1, 0–126	High	Disturbed core top
4H-1, 0–52	High	Disturbed core top
5H-1, 0–1	Moderate	Disturbed core top
6H-1, 0–7	Moderate	Disturbed core top
7H-1, 0–12	Moderate	Disturbed core top
8H-1, 0–25	Moderate	Disturbed core top
9H-1, 0–20	Moderate	Disturbed core top
10H-1, 0–25	Moderate	Disturbed core top
11H-1, 0–11	Mild	Disturbed core top
12H-1, 0–5	Mild	Disturbed core top
12H-7, 39–53	Moderate	Disturbed
13H-1, 0–1	Mild	Disturbed core top
14H-1, 0–40	Moderate	Disturbed core top
14H-2, 0–35	High	Disturbed
15H-1, 0–1	Mild	Disturbed core top
16H-1, 0–4	Moderate	Disturbed core top
17H-1, 0–18	Moderate	Disturbed core top

IW = interstitial water, MBIO = microbiology sample, WR = whole-round sample.

Table T15. NRM inclination, declination, and intensity data after 20 mT peak field AF demagnetization, Hole U1385A.

Core, section, interval (cm)	Depth (mbsf)	Inclination (°)	Declination (°)	FlexIt-corrected declination (°)	Intensity (A/m)
339-U1385A-					
1H-1	0.00				
1H-1, 5	0.05				
1H-1, 10	0.10				
1H-1, 15	0.15	56.9	93.2		0.010134
1H-1, 20	0.20	49.7	96.8		0.012295
1H-1, 25	0.25	52.1	98		0.014349
1H-1, 30	0.30	54.5	96.2		0.015921
1H-1, 35	0.35	53.3	92.3		0.015587
1H-1, 40	0.40	52.1	92.6		0.014752
1H-1, 45	0.45	56.5	92.4		0.015547
1H-1, 50	0.50	63.7	85.9		0.016321
1H-1, 55	0.55	61.1	77.6		0.018341
1H-1, 60	0.60	56.2	80.6		0.020623
1H-1, 65	0.65	55.1	78.9		0.018907
1H-1, 70	0.70	54.7	75.9		0.018063
1H-1, 75	0.75	55.5	78.5		0.017526
1H-1, 80	0.80	58.8	77		0.014217
1H-1, 85	0.85	62	74		0.012534
1H-1, 90	0.90	59.8	76.2		0.011826
1H-1, 95	0.95	52.7	80.1		0.011761
1H-1, 100	1.00	48.7	94.7		0.009848
1H-1, 105	1.05	42.2	212.5		0.007726
1H-1, 110	1.10				
1H-1, 115	1.15				
1H-1, 120	1.20				
2H-1	1.50				
2H-1, 5	1.55				
2H-1, 10	1.60				
2H-1, 15	1.65				
2H-1, 20	1.70	74.8	41.1		0.015763
2H-1, 25	1.75	75.5	59.2		0.025556
2H-1, 30	1.80	74.3	35.2		0.028653
2H-1, 35	1.85	69.4	18.4		0.034162
2H-1, 40	1.90	73.3	11.9		0.035801
2H-1, 45	1.95	72.6	15.7		0.033581
2H-1, 50	2.00	73.6	24.9		0.031852
2H-1, 55	2.05	73.4	33.7		0.028976
2H-1, 60	2.10	69.1	32.5		0.027091
2H-1, 65	2.15	67.7	26.1		0.023742
2H-1, 70	2.20	67.8	33.8		0.020042
2H-1, 75	2.25	66.1	45.6		0.016644
2H-1, 80	2.30	61.9	51.4		0.015028
2H-1, 85	2.35	63	47.8		0.015756
2H-1, 90	2.40	59.7	48.6		0.017084
2H-1, 95	2.45	58.5	49.3		0.017807
2H-1, 100	2.50	56.7	46.7		0.018582
2H-1, 105	2.55	54.5	46.7		0.018419
2H-1, 110	2.60	53.6	45.5		0.017568
2H-1, 115	2.65	53.2	42.4		0.017914
2H-1, 120	2.70	54.3	38.2		0.017867
2H-1, 125	2.75	53.9	40.2		0.017094
2H-1, 130	2.80	54.8	56.4		0.014234
2H-1, 135	2.85	56.4	55.8		0.013528
2H-1, 140	2.90				
2H-1, 145	2.95				
2H-1, 150	3.00				
2H-2	3.00				
2H-2, 5	3.05				
2H-2, 10	3.10				
2H-2, 15	3.15	56.1	36.9		0.01086

Blank cells indicate depth levels where data were either not available (i.e., FlexIt-corrected declination data for nonoriented cores) or removed because of disturbance, voids, or measurement edge effects. Only a portion of this table appears here. The complete table is available in **ASCII.**

Table T16. NRM inclination, declination, and intensity data after 20-mT peak field AF demagnetization, Hole U1385B.

Core, section, interval (cm)	Depth (mbsf)	Inclination (°)	Declination (°)	FlexIt-corrected declination (°)	Intensity (A/m)
339-U1385B-					
1H-1	0.00				
1H-1, 5	0.05				
1H-1, 10	0.10				
1H-1, 15	0.15	41.9	32.3		0.014059
1H-1, 20	0.20	16.6	346.2		0.019165
1H-1, 25	0.25	21.3	47.1		0.014141
1H-1, 30	0.30	48.3	29.5		0.011026
1H-1, 35	0.35	49.2	22.9		0.011593
1H-1, 40	0.40	47.9	20.2		0.012697
1H-1, 45	0.45	53.4	15.9		0.012711
1H-1, 50	0.50	58.8	37.7		0.011572
1H-1, 55	0.55	43.9	22.4		0.014599
1H-1, 60	0.60	45.5	16.5		0.015004
1H-1, 65	0.65	48.5	19.6		0.011734
1H-1, 70	0.70	51.9	12		0.009119
1H-1, 75	0.75	59.1	11.3		0.009609
1H-1, 80	0.80	63.2	3.9		0.012359
1H-1, 85	0.85	84.6	1.3		0.012898
1H-1, 90	0.90	67.9	63.7		0.010466
1H-1, 95	0.95				
1H-1, 100	1.00				
1H-1, 105	1.05				
1H-1, 110	1.10				
1H-1, 115	1.15				
1H-1, 120	1.20				
1H-1, 125	1.25				
1H-1, 130	1.30				
1H-1, 135	1.35				
1H-1, 140	1.40				
1H-1, 145	1.45				
1H-1, 150	1.50				
1H-2	1.50				
1H-2, 5	1.55				
1H-2, 10	1.60				
1H-2, 15	1.65	54.3	183.3		0.016054
1H-2, 20	1.70	49	169.6		0.017555
1H-2, 25	1.75	49.6	160.3		0.018024
1H-2, 30	1.80	48	172.6		0.016033
1H-2, 35	1.85	49.7	175		0.015479
1H-2, 40	1.90	52.3	165		0.017468
1H-2, 45	1.95	57.6	166.3		0.017707
1H-2, 50	2.00	57.1	174.3		0.01762
1H-2, 55	2.05	54.4	175.2		0.017673
1H-2, 60	2.10				
1H-2, 65	2.15				
1H-2, 70	2.20				
1H-2, 75	2.25				
1H-2, 80	2.30				
1H-2, 85	2.35				
1H-2, 90	2.40				
1H-2, 95	2.45				
1H-2, 100	2.50				
1H-2, 105	2.55				
1H-2, 110	2.60				
1H-2, 115	2.65				
1H-2, 120	2.70				
1H-2, 125	2.75				

Blank cells indicate depth levels where data were either not available (i.e., FlexIt-corrected declination data for nonoriented cores) or removed because of disturbance, voids, or measurement edge effects. Only a portion of this table appears here. The complete table is available in **ASCII.**

Table T17. NRM inclination, declination, and intensity data after 20-mT peak field AF demagnetization, Hole U1385C.

Core, section, interval (cm)	Depth (mbsf)	Inclination (°)	Declination (°)	FlexIt-corrected declination (°)	Intensity (A/m)
339-U1385C-					
1H-1	0.00				
1H-1, 5	0.05				
1H-1, 10	0.10				
1H-1, 15	0.15				
1H-1, 20	0.20				
1H-1, 25	0.25				
1H-1, 30	0.30				
1H-1, 35	0.35				
1H-1, 40	0.40	87.9	322.3		0.069494
1H-1, 45	0.45	83.8	34.8		0.075562
1H-1, 50	0.50	83.4	22.8		0.060633
1H-1, 55	0.55	83.1	25.3		0.044906
1H-1, 60	0.60	82.4	11.4		0.036784
1H-1, 65	0.65	80.8	344.4		0.030167
1H-1, 70	0.70	75.7	336.4		0.023769
1H-1, 75	0.75	69.7	340.9		0.020107
1H-1, 80	0.80	66.6	342.4		0.017843
1H-1, 85	0.85	68.2	346.2		0.016097
1H-1, 90	0.90	63.9	349.9		0.016349
1H-1, 95	0.95	62.3	346.2		0.01631
1H-1, 100	1.00	62	353.9		0.015958
1H-1, 105	1.05	60.5	353		0.016341
1H-1, 110	1.10	59.7	344.3		0.016947
1H-1, 115	1.15	61.1	340.4		0.015866
1H-1, 120	1.20	58.8	342.7		0.013919
1H-1, 125	1.25				
1H-1, 130	1.30				
1H-1, 135	1.35	58.6	295.9		0.012629
1H-1, 140	1.40				
1H-1, 145	1.45				
1H-1, 150	1.50				
1H-2	1.50				
1H-2, 5	1.55				
1H-2, 10	1.60				
1H-2, 15	1.65	45.6	331.7		0.020107
1H-2, 20	1.70	46.3	333.4		0.019184
1H-2, 25	1.75	50.3	329.8		0.015801
1H-2, 30	1.80	54.3	322.9		0.013859
1H-2, 35	1.85	53.2	316.7		0.01341
1H-2, 40	1.90	47.8	314		0.013432
1H-2, 45	1.95	49.1	315.8		0.012435
1H-2, 50	2.00	55.7	308.6		0.01088
1H-2, 55	2.05	50.7	317.6		0.013192
1H-2, 60	2.10	51.4	318.6		0.01378
1H-2, 65	2.15	51.8	320.7		0.013575
1H-2, 70	2.20	49.4	317.7		0.01453
1H-2, 75	2.25	49.7	317.9		0.01553
1H-2, 80	2.30	50.4	318.3		0.016807
1H-2, 85	2.35	51.7	321.6		0.017202
1H-2, 90	2.40	48.4	324.4		0.017796
1H-2, 95	2.45	46.1	322.4		0.01679
1H-2, 100	2.50	52.9	317.7		0.012389
1H-2, 105	2.55	62.4	319.8		0.008409
1H-2, 110	2.60	48.8	322.8		0.012416
1H-2, 115	2.65	48.2	326.8		0.013187
1H-2, 120	2.70	48.2	325.5		0.012492
1H-2, 125	2.75	47.8	325.7		0.01181

Blank cells indicate depth levels where data were either not available (i.e., FlexIt-corrected declination data for nonoriented cores) or removed because of disturbance, voids, or measurement edge effects. Only a portion of this table appears here. The complete table is available in **ASCII.**

Table T18. NRM inclination, declination, and intensity data after 20-mT peak field AF demagnetization, Hole U1385D.

Core, section, interval (cm)	Depth (mbsf)	Inclination (°)	Declination (°)	FlexIt-corrected declination (°)	Intensity (A/m)
339-U1385D-					
1H-1	0.00				
1H-1, 5	0.05				
1H-1, 10	0.10				
1H-1, 15	0.15	66	158.6		0.009051
1H-1, 20	0.20	59.1	160.7		0.010522
1H-1, 25	0.25	55.1	156.6		0.012497
1H-1, 30	0.30	59.9	158.2		0.014673
1H-1, 35	0.35	65.4	160		0.01608
1H-1, 40	0.40	67.1	157.3		0.015818
1H-1, 45	0.45	65.4	146.9		0.015783
1H-1, 50	0.50	63.6	142.3		0.017001
1H-1, 55	0.55	62.3	145.5		0.019999
1H-1, 60	0.60	69.8	164.2		0.020681
1H-1, 65	0.65	76.8	184.3		0.019114
1H-1, 70	0.70	69.7	164.4		0.019632
1H-1, 75	0.75	62.7	146.3		0.020656
1H-1, 80	0.80	61.4	139.3		0.020862
1H-1, 85	0.85	63.3	136.7		0.020848
1H-1, 90	0.90	63.7	132.3		0.019488
1H-1, 95	0.95	63.3	127.1		0.017637
1H-1, 100	1.00	60.9	123.8		0.017789
1H-1, 105	1.05	55.3	127.2		0.019152
1H-1, 110	1.10	53	126.4		0.018706
1H-1, 115	1.15	53.9	124.2		0.015045
1H-1, 120	1.20	56.3	132.5		0.012917
1H-1, 125	1.25	58	143.8		0.012402
1H-1, 130	1.30	59.6	131.3		0.012034
1H-1, 135	1.35	59.9	125.6		0.011155
1H-1, 140	1.40				
1H-1, 145	1.45				
1H-1, 150	1.50				
1H-2	1.50				
1H-2, 5	1.55				
1H-2, 10	1.60				
1H-2, 15	1.65	57.1	123.8		0.018843
1H-2, 20	1.70	63.5	125.5		0.017719
1H-2, 25	1.75	62.3	131.9		0.017966
1H-2, 30	1.80	58.2	136.1		0.019869
1H-2, 35	1.85	58.5	131.1		0.020747
1H-2, 40	1.90	59.7	125.1		0.020304
1H-2, 45	1.95	59.9	124.8		0.02018
1H-2, 50	2.00	60.4	121.7		0.01914
1H-2, 55	2.05	61	119.6		0.017038
1H-2, 60	2.10	63.7	124.7		0.01513
1H-2, 65	2.15	61.9	118.1		0.015512
1H-2, 70	2.20	61.2	117.5		0.015879
1H-2, 75	2.25	57.5	115		0.016284
1H-2, 80	2.30	51.6	117.7		0.019418
1H-2, 85	2.35	52.6	117.4		0.019639
1H-2, 90	2.40	54.7	116		0.018284
1H-2, 95	2.45	51.9	115.5		0.01857
1H-2, 100	2.50	53.5	112.3		0.014437
1H-2, 105	2.55	57.2	113.1		0.011077
1H-2, 110	2.60	55.8	111.2		0.010037
1H-2, 115	2.65	53.7	112.7		0.011562
1H-2, 120	2.70	53.6	119.3		0.013723
1H-2, 125	2.75	58.6	126.8		0.013204

Blank cells indicate depth levels where data were either not available (i.e., FlexIt-corrected declination data for nonoriented cores) or removed because of disturbance, voids, or measurement edge effects. Only a portion of this table appears here. The complete table is available in **ASCII.**

Table T19. NRM inclination, declination, and intensity data after 20-mT peak field AF demagnetization, Hole U1385E.

Core, section, interval (cm)	Depth (mbsf)	Inclination (°)	Declination (°)	FlexIt-corrected declination (°)	Intensity (A/m)
339-U1385E-					
1H-1	0.00				
1H-1, 5	0.05				
1H-1, 10	0.10				
1H-1, 15	0.15	11.2	274.9		0.045423
1H-1, 20	0.20	66.9	328.2		0.014742
1H-1, 25	0.25	63.6	68.9		0.013949
1H-1, 30	0.30	44.5	55.8		0.018126
1H-1, 35	0.35	47	51.1		0.019345
1H-1, 40	0.40	50.4	46.7		0.019333
1H-1, 45	0.45	50.7	46.8		0.019671
1H-1, 50	0.50	49.2	44.8		0.020063
1H-1, 55	0.55	49.9	44.8		0.020575
1H-1, 60	0.60	55.1	52.2		0.018287
1H-1, 65	0.65	53.3	54.2		0.018619
1H-1, 70	0.70	52.2	51.4		0.019242
1H-1, 75	0.75	51.9	57.8		0.017628
1H-1, 80	0.80	47.7	59.2		0.017576
1H-1, 85	0.85				
1H-1, 90	0.90				
1H-1, 95	0.95				
2H-1	1.00				
2H-1, 5	1.05				
2H-1, 10	1.10				
2H-1, 15	1.15				
2H-1, 20	1.20				
2H-1, 25	1.25				
2H-1, 30	1.30				
2H-1, 35	1.35				
2H-1, 40	1.40				
2H-1, 45	1.45				
2H-1, 50	1.50				
2H-1, 55	1.55				
2H-1, 60	1.60				
2H-1, 65	1.65				
2H-1, 70	1.70				
2H-1, 75	1.75				
2H-1, 80	1.80				
2H-1, 85	1.85				
2H-1, 90	1.90				
2H-1, 95	1.95				
2H-1, 100	2.00				
2H-1, 105	2.05				
2H-1, 110	2.10				
2H-1, 115	2.15				
2H-1, 120	2.20				
2H-1, 125	2.25				
2H-1, 130	2.30				
2H-1, 135	2.35				
2H-1, 140	2.40				
2H-1, 145	2.45				
2H-1, 150	2.50				
2H-2	2.51				
2H-2, 5	2.56				
2H-2, 10	2.61				
2H-2, 15	2.66	74.5	346.8		0.009382
2H-2, 20	2.71	76.8	346.9		0.009358
2H-2, 25	2.76	77.3	341		0.009854
2H-2, 30	2.81	74	335		0.010306
2H-2, 35	2.86	72.9	338.9		0.0106

Blank cells indicate depth levels where data were either not available (i.e., FlexIt-corrected declination data for nonoriented cores) or removed because of disturbance, voids, or measurement edge effects. Only a portion of this table appears here. The complete table is available in **ASCII.**

Table T20. Polarity boundaries, Site U1385.

Polarity boundary	Age (Ma)	Hole U1385A			Hole U1385B			Hole U1385D			Hole U1385E		
		Core, section, interval (cm)	Depth (mbsf)	Depth (mcd)	Core, section, interval (cm)	Depth (mbsf)	Depth (mcd)	Core, section, interval (cm)	Depth (mbsf)	Depth (mcd)	Core, section, interval (cm)	Depth (mbsf)	Depth (mcd)
		339-U1385A-			339-U1385B-			339-U1385D-			339-U1385E-		
Brunhes/Matuyama	0.781	11H-5, ~80	**93.8**	102.68	11H-1, ~20	91.8	102.73	11H-6, ~36	**97.3**	102.89	12H-1, ~0	92.0	103.85
T Jaramillo	0.988	13H-1, ~80	106.8	115.48	12H-1, ~10	**101.2**	113.08	12H-6, ~82	107.3	113.92	13H-1, ~0	**101.5**	113.92
B Jaramillo	1.072	14H-2, ~68	**117.7**	126.92	13H-2, ~130	113.4	126.36	13H-6, ~30	116.3	125.71	14H-1, ~20	111.2	124.95
T Cobb Mountain	1.173	15H-4, ~143	131.0	140.90	14H-6, ~133	**129.0**	141.61	14H-7, ~44	127.4	138.58	16H-2, ~70	130.8	143.02
B Cobb Mountain	1.185	15H-5, ~129	132.4	142.30	15H-2, ~105	**132.1**	144.68	15H-2, ~139	130.3	141.89	16H-3, ~69	132.3	144.52

Bold = relatively well defined boundaries. T = top, B = bottom.

Table T21. Headspace sample hydrocarbon concentrations, Hole U1385A.

Core, section, interval (cm)	Concentration (ppmv)		
	Methane	Ethane	Ethene
339-U1385A-			
1H-1, 116–121	6.75	—	—
2H-7, 0–5	4.49	—	—
3H-7, 0–5	2.88	—	—
4H-7, 0–5	3.05	—	—
5H-7, 0–5	3.70	—	—
6H-7, 0–5	107.47	—	—
7H-7, 0–5	11,600.39	—	—
8H-7, 0–5	29,710.00	0.76	—
9H-7, 0–5	60,850.40	1.56	—
10H-7, 0–5	68,269.83	1.63	—
11H-6, 0–5	87,447.83	2.46	—
12H-7, 0–5	79,673.24	2.14	1.05
13H-7, 0–5	53,994.54	1.66	0.45
14H-6, 0–5	68,375.44	2.13	0.69
15H-6, 0–5	43,811.24	1.42	0.00
16H-6, 0–5	64,125.15	2.07	1.23
17H-5, 0–5	56,190.83	1.87	0.75

— = no data.

Table T22. Interstitial water major and trace elements, Hole U1385B.

Core, section, interval (cm)	Depth (mbsf)	Salinity (psu)	pH ISE	Alkalinity (meq/L) TITRA_AUTO	NH_4^+ (μM) SPEC	SO_4^{2-} (mM) IC	Cl^- (mM)		Ca (mM)		Mg (mM)		K (mM)	
							IC	Titration	IC	393.366 nm ICPAES	IC	279.533 nm ICPAES	IC	769.897 nm ICPAES
339-U1385B-														
1H-3,145–155	4.5		7.76	9.081	957.3	16.9	478	554	7.5	7.0	44.6	46.4	10.6	11.5
2H-6, 145–155	15.1		7.59	9.449	1272.7	18.5	522	562	5.9	6.0	45.8	46.7	11.4	11.5
3H-6, 145–155	24.6		7.72	9.176	1338.8	16.9	532	547	5.7	6.3	46.4	51.7	11.5	12.0
4H-6, 145–155	34.1		7.64	9.587	1453.9	16.1	502	554	4.8	4.9	44.3	47.7	10.5	10.9
5H-6, 145–155	43.6		7.82	11.335	2215.0	8.1	509	548	3.0	3.1	38.7	40.0	10.2	10.3
6H-6, 115–125	52.8		7.79	13.028	2789.1	0.0	591	551	2.7	2.1	37.8	34.1	10.6	10.0
7H-6, 145–150	62.6		7.48	13.473	3281.9	0.0	534	561	3.2	3.4	32.7	36.2	9.3	10.1
8H-6, 106–110	71.7		7.72	12.002	3516.6	0.0	533	549	3.4	3.7	31.9	35.5	9.2	10.2
9H-6, 96–100	81.1		7.79	12.735	3872.4	0.0	586	538	3.8	4.3	34.1	38.8	10.0	10.4
10H-6, 145–150	91.2	3.3	7.90	14.208	4004.8	0.0	575	544	4.4	3.8	32.8	27.0	9.3	8.1
11H-6, 147–152	100.8	3.4	7.90	16.835	4235.3	0.0	515	555	3.8	4.2	28.4	32.4	8.9	9.7
12H-6, 141–146	110.0	3.3	7.91	19.216	4495.1	0.0	607	554	4.4	4.3	32.6	32.9	10.9	10.2
13H-6, 116–121	119.3	3.3	7.70	11.353	4265.0			558		4.8		30.5		9.3
14H-6, 145–150	129.1	3.2	7.91	19.995	4482.9	0.0	559	553	5.1	4.0	30.5	26.3	8.9	8.0
15H-5, 129–134	136.9	3.3	7.77	29.910	4619.1	0.0	568	559	5.3	4.2	30.0	26.9	8.7	8.4
16H-5, 145–150	145.2	3.3	7.83	25.501	4820.2	0.0	615	560	5.6	4.5	33.9	29.1	10.3	9.1

TITRA_AUTO = automatic titration, SPEC = spectrometer, IC = ion chromatograph, ICPAES = inductively coupled plasma–atomic emission spectrometer, ISE = ion-selective electrode.

Core, section, interval (cm)	Depth (mbsf)	Na (mM)		B (μM)	Ba (μM)	Fe (μM)	Li (μM)	Mn (μM)	Si (μM)	Sr (μM)
		IC	589.592 nm ICPAES	249.677 nm ICPAES	493.409 nm ICPAES	239.563 nm ICPAES	670.78 nm ICPAES	259.372 nm ICPAES	251.611 nm ICPAES	407.771 nm ICPAES
339-U1385B-										
1H-3,145–155	4.5	428.7	479.0	415.8	46.7	118.1	48.4	18.5	356.3	122.1
2H-6, 145–155	15.1	455.5	491.9	441.5	46.8	90.9	53.1	16.7	291.5	122.5
3H-6, 145–155	24.6	462.6	461.5	358.4	46.8	60.1	46.6	13.7	298.4	110.7
4H-6, 145–155	34.1	443.2	479.2	371.3	46.9	34.8	45.7	13.8	277.5	114.7
5H-6, 145–155	43.6	453.6	479.3	349.4	47.4	29.6	45.1	12.4	342.7	114.0
6H-6, 115–125	52.8	503.8	481.5	326.5	81.4	23.7	41.6	12.2	241.6	114.8
7H-6, 145–150	62.6	460.1	484.5	331.1	120.6	26.3	47.4	12.4	343.9	133.4
8H-6, 106–110	71.7	461.9	472.3	328.7	137.0	22.4	52.5	12.5	346.7	140.4
9H-6, 96–100	81.1	497.7	453.6	359.1	159.4	17.6	66.0	12.5	362.9	162.7
10H-6, 145–150	91.2	487.8	487.7	273.9	132.2	16.4	60.6	12.3	372.6	145.9
11H-6, 147–152	100.8	450.0	488.6	253.0	139.4	16.5	71.8	12.6	462.9	153.0
12H-6, 141–146	110.0	527.1	487.9	254.6	140.9	15.7	83.2	12.7	417.5	162.4
13H-6, 116–121	119.3		488.5	254.3	132.9	17.9	74.8	15.2	385.0	154.9
14H-6, 145–150	129.1	475.5	504.2	245.2	137.8	17.0	76.0	13.6	296.8	155.5
15H-5, 129–134	136.9	470.1	517.8	245.2	141.5	16.3	83.3	13.7	348.0	161.7
16H-5, 145–150	145.2	529.9	508.6	283.4	162.8	16.3	96.9	13.9	358.2	181.5

Table T23. Interstitial water oxygen and hydrogen isotopes, Hole U1385B.

Core, section, interval (cm)	Depth (mbsf)	$\delta^{18}O$ (‰, VSMOW)	δD (‰, VSMOW)
339-U1385B-			
Mudline	0.00	0.01	1.03
1H-1, 145–155	1.45	–0.07	0.30
1H-2, 140–150	2.95	0.00	1.33
1H-3, 145–155	4.50	0.11	1.58
2H-1, 140–150	7.55	0.41	1.43
2H-2, 140–150	9.05	0.18	1.72
2H-3, 140–150	10.55	0.29	1.81
2H-4, 140–150	12.05	0.05	1.42
2H-5, 140–150	13.50	0.10	1.13
2H-6, 145–155	15.10	0.01	1.75
3H-1, 140–150	17.10	0.34	1.54
3H-2, 140–150	18.60	0.26	1.42
3H-3, 140–150	20.10	0.27	2.50
3H-4, 140–150	21.55	0.16	1.46
3H-5, 140–150	23.05	0.36	2.07
3H-6, 145–155	24.60	0.00	3.08
4H-1, 140–150	26.60	0.35	2.85
4H-2, 140–150	28.10	0.27	2.50
4H-6, 145–155	34.10	0.13	2.14
5H-6, 145–155	43.60	0.00	1.83
6H-6, 145–155	53.10	0.22	3.14
7H-6, 145–155	62.60	–0.12	3.62
8H-6, 145–155	72.10	0.09	2.57
9H-6, 145–155	81.60	–0.01	1.90
10H-6, 145–155	91.10	0.00	1.90
11H-6, 145–155	100.60	–0.21	1.30
12H-6, 145–155	110.10	–0.11	1.75
13H-6, 145–155	119.60	0.09	2.60
14H-6, 145–150	130.60	–0.11	1.67
15H-5, 129–134	136.91	0.07	2.55
16H-5, 145–150	145.20	0.10	1.92

VSMOW = Vienna standard mean ocean water.

Table T24. Results from APCT-3 temperature profiles, Site U1385.

Core	Minimum temperature (°C)	Average temperature at mudline (°C)	Depth DSF (m)	In situ temperature (°C)
339-U1385A-				
4H	3.34	3.37	30.0	5.06*
7H	3.45	3.69	58.5	5.83
10H	3.45	3.80	87.0	7.05*
13H	3.37	3.56	115.5	8.02
339-U1385B-				
4H	3.48	3.59	34.6	4.78
7H	3.52	3.65	63.1	5.77
10H	3.56	3.67	91.6	7.11
13H	3.49	3.55	120.1	7.95*
339-U1385D-				
4H	3.40	3.64	35.4	4.89
7H	3.49	3.71	60.9	5.47
10H	3.22	3.30	89.4	6.91
13H	3.23	3.48	117.9	7.91
Average:	3.42	3.58		

* = unreliable measurement because of short measurement time and/or poor coupling with the formation. In situ temperatures were determined using TP-Fit software by Martin Heesemann. Thermal resistance was calculated from thermal conductivity data (see **"Physical properties"**) corrected for in situ conditions (see **"Downhole measurements"** section in the "Methods" chapter [Expedition 339 Scientists, 2013]).

Table T25. Meters composite depth scale, Site U1385.

Core	Top depth (mbsf)	Top depth (mcd)	Offset (m)
339-U1385A-			
1H	0.00	0.08	0.08
2H	1.50	0.44	–1.06
3H	11.00	10.77	–0.23
4H	20.50	22.13	1.63
5H	30.00	33.47	3.47
6H	39.50	44.53	5.03
7H	49.00	55.91	6.91
8H	58.50	65.81	7.31
9H	68.00	75.72	7.72
10H	77.50	85.84	8.34
11H	87.00	95.88	8.88
12H	96.50	104.76	8.26
13H	106.00	114.68	8.68
14H	115.50	124.72	9.22
15H	125.00	134.90	9.90
16H	134.50	143.67	9.17
17H	144.00	153.17	9.17
339-U1385B-			
1H	0.00	0.08	0.08
2H	6.10	7.69	1.59
3H	15.60	17.70	2.10
4H	25.10	28.95	3.85
5H	34.60	38.38	3.78
6H	44.10	48.64	4.54
7H	53.60	60.13	6.53
8H	63.10	70.10	7.00
9H	72.60	81.73	9.13
10H	82.10	92.09	9.99
11H	91.60	102.53	10.93
12H	101.10	112.98	11.88
13H	110.60	123.56	12.96
14H	120.10	132.71	12.61
15H	129.60	142.18	12.58
16H	137.70	152.27	14.57

Core	Top depth (mbsf)	Top depth (mcd)	Offset (m)
339-U1385C-			
1H	0.00	0.76	0.76
339-U1385D-			
1H	0.00	0.00	0.00
2H	6.90	8.43	1.53
3H	16.40	19.40	3.00
4H	25.90	28.88	2.98
5H	35.40	38.41	3.01
6H	41.90	44.82	2.92
7H	51.40	54.04	2.64
8H	60.90	63.73	2.83
9H	70.40	73.51	3.11
10H	79.90	83.72	3.82
11H	89.40	94.99	5.59
12H	98.90	105.52	6.62
13H	108.40	117.81	9.41
14H	117.90	129.08	11.18
15H	127.40	138.99	11.59
16H	136.90	153.05	16.15
339-U1385E-			
1H	0.00	0.00	0.00
2H	1.00	2.97	1.97
3H	10.50	14.78	4.28
4H	20.00	24.11	4.11
5H	29.50	35.34	5.84
6H	39.00	45.83	6.83
7H	48.50	55.43	6.93
8H	58.00	66.03	8.03
9H	64.50	73.79	9.29
10H	74.00	83.84	9.84
11H	82.50	93.42	10.92
12H	92.00	103.85	11.85
13H	101.50	113.92	12.42
14H	111.00	124.75	13.75
15H	120.50	132.17	11.67
16H	128.60	140.82	12.22
17H	138.10	154.15	16.05

Table T26. Primary splice tie points for Site U1385.

Hole, core, section interval (cm)	Depth (mbsf)	Depth (mcd)		Hole, core, section, interval (cm)	Depth (mbsf)	Depth (mcd)
339-				339-		
U1385D-1H-2, 131.89	2.82	2.82	Tie to	U1385A-2H-2, 88.1	3.88	2.82
U1385A-2H-6, 40.18	9.40	8.34	Tie to	U1385B-2H-1, 65	6.75	8.34
U1385B-2H-5, 23.09	12.33	13.92	Tie to	U1385A-3H-3, 14.8	14.15	13.92
U1385A-3H-6, 125.76	19.76	19.53	Tie to	U1385E-3H-4, 24.5	15.25	19.53
U1385E-3H-5, 91.72	17.42	21.70	Tie to	U1385D-3H-2, 79.9	18.70	21.70
U1385D-3H-5, 121.43	23.61	26.61	Tie to	U1385E-4H-2, 100.5	22.50	26.61
U1385E-4H-6, 61.31	28.11	32.22	Tie to	U1385D-4H-3, 33.8	29.24	32.22
U1385D-4H-6, 129.48	34.69	37.67	Tie to	U1385E-5H-2, 83	31.83	37.67
U1385E-5H-7, 42.11	38.92	44.76	Tie to	U1385B-5H-5, 40.6	41.01	44.79
U1385B-5H-5, 143.09	42.03	45.81	Tie to	U1385A-6H-1, 127.5	40.78	45.81
U1385A-6H-4, 83.93	44.84	49.87	Tie to	U1385B-6H-1, 122.5	45.33	49.87
U1385B-6H-5, 147.52	51.58	56.12	Tie to	U1385D-7H-2, 57.6	53.48	56.12
U1385D-7H-5, 88.96	58.29	60.93	Tie to	U1385E-7H-4, 100	54.00	60.93
U1385E-7H-6, 63.76	56.64	63.57	Tie to	U1385B-7H-3, 43.7	57.04	63.57
U1385B-7H-5, 70.4	60.30	66.83	Tie to	U1385D-8H-3, 9.7	64.00	66.83
U1385D-8H-5, 142.28	68.32	71.15	Tie to	U1385B-8H-1, 105	64.15	71.15
U1385B-8H-3, 145.7	67.56	74.56	Tie to	U1385D-9H-1, 105	71.45	74.56
U1385D-9H-4, 118.51	76.09	79.20	Tie to	U1385A-9H-3, 48.4	71.48	79.20
U1385A-9H-6, 55	76.06	83.78	Tie to	U1385B-9H-2, 55.2	74.65	83.78
U1385B-9H-3, 125.64	76.86	85.99	Tie to	U1385A-10H-1, 15	77.65	85.99
U1385A-10H-6, 128.57	86.36	94.70	Tie to	U1385E-11H-1, 127.5	83.78	94.70
U1385E-11H-2, 119.58	85.20	96.12	Tie to	U1385D-11H-1, 112.5	90.53	96.12
U1385D-11H-7, 32.94	98.73	104.32	Tie to	U1385B-11H-2, 29.1	93.39	104.32
U1385B-11H-2, 71.56	93.82	104.75	Tie to	U1385E-12H-1, 90	92.90	104.75
U1385E-12H-4, 120.47	97.70	109.55	Tie to	U1385D-12H-3, 102.9	102.93	109.55
U1385D-12H-6, 149.88	107.90	114.52	Tie to	U1385E-13H-1, 60	102.10	114.52
U1385E-13H-6, 65.69	109.66	122.08	Tie to	U1385D-13H-3, 124.2	112.67	122.08
U1385D-13H-5, 77.93	115.30	124.71	Tie to	U1385B-13H-1, 115	111.75	124.71
U1385B-13H-5, 51.45	117.15	130.11	Tie to	U1385D-14H-1, 102.5	118.93	130.11
U1385D-14H-6, 56.81	125.97	137.15	Tie to	U1385B-14H-3, 144.3	124.54	137.15
U1385B-14H-6, 35.92	127.96	140.57	Tie to	U1385D-15H-2, 6.8	128.98	140.57
U1385D-15H-6, 46.45	135.48	147.07	Tie to	U1385A-16H-3, 40	137.90	147.07
U1385A-16H-6, 107.18	143.13	152.30	Tie to	U1385B-16H-1, 2.5	137.73	152.30
U1385B-16H-4, 44.66	142.65	157.22	Tie to	U1385E-17H-3, 8.5	141.17	157.22

Table T27. Secondary (AB) splice tie points, Site U1385.

Hole, core, section, interval (cm)	Depth (mbsf)	Depth (mcd)		Hole, core, section, interval (cm)	Depth (mbsf)	Depth (mcd)
339-				339-		
U1385A-1H-1, 75	0.75	0.83	Append to	U1385A-2H-1, 39	1.89	0.83
U1385A-2H-7, 30	10.80	9.74	Tie to	U1385B-2H-2, 55	8.15	9.74
U1385B-2H-7, 58	15.68	17.27	Tie to	U1385A-3H-5, 50	17.50	17.27
U1385A-3H-7, 59	20.59	20.35	Tie to	U1385B-3H-2, 116	18.26	20.36
U1385B-3H-6, 93	24.03	26.13	Tie to	U1385A-4H-3, 100	24.50	26.13
U1385A-4H-7, 81	30.31	31.94	Tie to	U1385B-4H-2, 149	28.09	31.94
U1385B-4H-4, 90	30.50	34.35	Tie to	U1385A-5H-1, 88	30.88	34.35
U1385A-5H-6, 124	38.74	42.21	Tie to	U1385B-5H-3, 83	38.43	42.21
U1385B-5H-6, 122	43.32	47.10	Tie to	U1385A-6H-2, 107	42.07	47.10
U1385A-6H-5, 119	46.69	51.72	Tie to	U1385B-6H-3, 8	47.18	51.72
U1385B-6H-6, 31	51.91	56.45	Tie to	U1385A-7H-1, 54	49.54	56.45
U1385A-7H-7, 15	57.87	64.78	Tie to	U1385B-7H-4, 15	58.25	64.78
U1385B-7H-6, 139	62.49	69.02	Tie to	U1385A-8H-3, 21	61.71	69.02
U1385A-8H-6, 60	66.63	73.94	Tie to	U1385B-8H-3, 84	66.94	73.94
U1385B-8H-6, 24	70.84	77.84	Tie to	U1385A-9H-2, 62	70.12	77.84
U1385A-9H-5, 132	75.33	83.05	Tie to	U1385B-9H-1, 132	73.92	83.05
U1385B-9H-4, 42	77.52	86.65	Tie to	U1385A-10H-1, 81	78.31	86.65
U1385A-10H-7, 24	86.83	95.17	Tie to	U1385B-10H-3, 8	85.18	95.17
U1385B-10H-5, 29	88.39	98.38	Tie to	U1385A-11H-2, 100	89.50	98.38
U1385A-11H-6, 125	95.76	104.64	Tie to	U1385B-11H-2, 61	93.71	104.64
U1385B-11H-6, 35	99.58	110.51	Tie to	U1385A-12H-4, 113	102.25	110.51
U1385A-12H-7, 21	105.66	113.92	Tie to	U1385B-12H-1, 94	102.04	113.92
U1385B-12H-6, 40	108.87	120.75	Tie to	U1385A-13H-5, 7	112.07	120.75
U1385A-13H-7, 32	115.32	124.00	Tie to	U1385B-13H-1, 44	111.04	124.00
U1385B-13H-4, 45	115.58	128.54	Tie to	U1385A-14H-3, 75	119.32	128.54
U1385A-14H-6, 100	124.17	133.39	Tie to	U1385B-14H-1, 69	120.79	133.39
U1385B-14H-4, 78	125.38	137.98	Tie to	U1385A-15H-3, 4	128.08	137.98
U1385A-15H-6, 26	132.93	142.83	Tie to	U1385B-15H-1, 65	130.25	142.83
U1385B-15H-5, 50	136.02	148.60	Tie to	U1385A-16H-4, 40	139.43	148.60
U1385A-16H-6, 139	143.45	152.62	Tie to	U1385B-16H-1, 35	138.05	152.62

Table T28. Secondary (DE) splice tie points, Site U1385.

Hole, core, section, interval (cm)	Depth (mbsf)	Depth (mcd)		Hole, core, section, interval (cm)	Depth (mbsf)	Depth (mcd)
339-				339-		
U1385D-1H-3, 109	4.09	4.09	Tie to	U1385E-2H-1, 112	2.12	4.09
U1385E-2H-6, 42	8.92	10.89	Tie to	U1385D-2H-2, 96	9.36	10.89
U1385D-2H-7, 47	16.37	17.90	Tie to	U1385E-3H-3, 12	13.62	17.90
U1385E-3H-6, 84	18.84	23.12	Tie to	U1385D-3H-3, 72	20.12	23.12
U1385D-3H-5, 60	23.00	26.00	Tie to	U1385E-4H-2, 39	21.89	26.00
U1385E-4H-6, 75	28.25	32.36	Tie to	U1385D-4H-3, 48	29.38	32.36
U1385D-4H-6, 67	34.07	37.05	Tie to	U1385E-5H-2, 21	31.21	37.05
U1385E-5H-6, 77	37.77	43.61	Tie to	U1385D-5H-4, 70	40.60	43.61
U1385D-5H-5, 93	42.33	45.34	Append to	U1385E-6H-1, 0	39.00	45.83
U1385E-6H-6, 113	47.63	54.46	Tie to	U1385D-7H-1, 42	51.82	54.46
U1385D-7H-5, 145	58.85	61.49	Tie to	U1385E-7H-5, 6	54.56	61.49
U1385E-7H-7, 29	57.79	64.72	Tie to	U1385D-8H-1, 99	61.89	64.72
U1385D-8H-7, 59	70.49	73.32	Append to	U1385D-9H-1, 0	70.40	73.51
U1385D-9H-6, 53	78.43	81.54	Tie to	U1385E-9H-6, 42	72.25	81.54
U1385E-9H-7, 108	74.37	83.66	Append to	U1385D-10H-1, 0	79.90	83.72
U1385D-10H-7, 62	89.52	93.34	Append to	U1385E-11H-1, 0	82.50	93.42
U1385E-11H-7, 37	91.37	102.29	Tie to	U1385D-11H-5, 130	96.70	102.29
U1385D-11H-7, 39	98.79	104.38	Tie to	U1385E-12H-1, 53	92.53	104.38
U1385E-12H-6, 60	100.10	111.95	Tie to	U1385D-12H-5, 43	105.33	111.95
U1385D-12H-6, 119	107.59	114.21	Tie to	U1385E-13H-1, 29	101.79	114.21
U1385E-13H-7, 43	110.93	123.35	Tie to	U1385D-13H-4, 96	113.94	123.35
U1385D-13H-6, 103	117.08	126.49	Tie to	U1385E-14H-2, 134	112.74	126.49
U1385E-14H-7, 99	118.07	131.82	Tie to	U1385D-14H-2, 124	120.64	131.82
U1385D-14H-7, 29	127.19	138.37	Tie to	U1385E-15H-5, 20	126.70	138.37
U1385E-15H-5, 115	127.65	139.32	Tie to	U1385D-15H-1, 33	127.73	139.32
U1385D-15H-6, 81	135.83	147.42	Tie to	U1385E-16H-5, 60	135.20	147.42
U1385E-16H-7, 59	138.26	150.48	Append to	U1385D-16H-1, 0	136.90	153.05
U1385D-16H-3, 114	141.05	157.20	Tie to	U1385E-17H-3, 6	141.15	157.20

Table T29. Excluded magnetic susceptibility data, Site U1385.

Core, section, interval (cm)	Core, section, interval (cm)	Core, section, interval (cm)	Core, section, interval (cm)	Core, section, interval (cm)
339-U1385A-	5H-3, 0	8H-1, 0	12H-1, 8	12H-7, 2
1H-1, 0	5H-3, 150	8H-1, 150	12H-1, 10	12H-7, 60
1H-1, 120	5H-4, 2	8H-2, 0	12H-1, 13	13H-1, 0
2H-1, 0	5H-4, 150	8H-2, 150	12H-1, 15	13H-1, 150
2H-1, 148	5H-5, 1	8H-3, 0	12H-1, 18	13H-2, 2
2H-2, 1	5H-5, 151	8H-3, 8	12H-1, 20	13H-2, 150
2H-2, 148	5H-6, 2	8H-3, 156	12H-1, 23	13H-3, 1
2H-3, 0	5H-6, 150	8H-4, 1	12H-1, 25	13H-3, 76
2H-3, 148	5H-7, 1	8H-4, 153	12H-1, 28	13H-3, 119
2H-4, 0.32	5H-7, 68	8H-5, 1	12H-1, 30	13H-3, 151
2H-4, 148	6H-1, 0	8H-5, 4	12H-1, 33	13H-4, 2
2H-5, 0	6H-1, 3	8H-5, 156	12H-1, 35	13H-4, 152
2H-5, 148	6H-1, 5	8H-6, 0	12H-1, 38	13H-5, 2
2H-6, 0	6H-1, 8	8H-6, 10	12H-1, 40	13H-5, 94
2H-6, 143	6H-1, 10	8H-6, 145	12H-1, 43	13H-5, 152
2H-7, 1	6H-1, 13	8H-7, 2	12H-1, 45	13H-6, 1
2H-7, 68	6H-1, 15	8H-7, 69	12H-1, 48	13H-6, 19
2H-7, 71	6H-1, 18	9H-1, 0	12H-1, 50	13H-6, 121
3H-1, 0	6H-1, 20	9H-1, 150	12H-1, 53	13H-6, 151
3H-1, 148	6H-1, 23	9H-2, 1	12H-1, 55	13H-7, 1
3H-2, 1	6H-1, 25	9H-2, 4	12H-1, 58	13H-7, 58
3H-2, 151	6H-1, 28	9H-2, 6	12H-1, 60	13H-7, 61
3H-3, 2	6H-1, 30	9H-2, 9	12H-1, 63	13H-7, 63
3H-3, 147	6H-1, 33	9H-2, 159	12H-1, 65	14H-1, 0
3H-4, 1	6H-1, 35	9H-3, 1	12H-1, 68	14H-1, 3
3H-4, 148	6H-1, 38	9H-3, 151	12H-1, 70	14H-1, 5
3H-5, 1	6H-1, 40	9H-4, 0	12H-1, 73	14H-1, 25
3H-5, 148	6H-1, 43	9H-4, 150	12H-1, 75	14H-1, 28
3H-6, 1	6H-1, 45	9H-5, 1	12H-1, 78	14H-1, 150
3H-6, 151	6H-1, 150	9H-5, 151	12H-1, 80	14H-2, 1
3H-7, 3	6H-2, 2	9H-6, 0	12H-1, 83	14H-2, 16
3H-7, 63	6H-2, 150	9H-6, 143	12H-1, 85	14H-2, 153
4H-1, 0	6H-3, 0.19	9H-6, 153	12H-1, 88	14H-3, 1
4H-1, 3	6H-3, 145	9H-7, 2	12H-1, 90	14H-3, 154
4H-1, 5	6H-3, 148	9H-7, 54	12H-1, 92.5	14H-4, 2
4H-1, 8	6H-3, 150	10H-1, 0	12H-1, 95	14H-4, 152
4H-1, 10	6H-4, 1	10H-1, 148	12H-1, 98	14H-5, 2
4H-1, 13	6H-4, 151	10H-2, 0	12H-1, 100	14H-5, 147
4H-1, 15	6H-5, 0	10H-2, 150	12H-1, 103	14H-6, 1
4H-1, 18	6H-5, 150	10H-3, 0	12H-1, 105	14H-6, 123
4H-1, 20	6H-6, 2	10H-3, 153	12H-1, 108	15H-1, 0
4H-1, 23	6H-6, 112	10H-4, 0	12H-1, 110	15H-1, 3
4H-1, 25	6H-6, 144	10H-4, 153	12H-1, 113	15H-1, 5
4H-1, 28	6H-7, 2	10H-5, 0	12H-1, 115	15H-1, 8
4H-1, 30	6H-7, 62	10H-5, 155	12H-1, 118	15H-1, 150
4H-1, 33	7H-1, 0	10H-6, 1	12H-1, 120	15H-2, 0
4H-1, 35	7H-1, 3	10H-6, 154	12H-1, 123	15H-2, 153
4H-1, 38	7H-1, 5	10H-7, 0	12H-1, 125	15H-3, 1
4H-1, 40	7H-1, 8	10H-7, 63	12H-1, 128	15H-3, 151
4H-1, 43	7H-1, 10	11H-1, 0	12H-1, 130	15H-4, 1
4H-1, 150	7H-1, 148	11H-1, 150	12H-1, 133	15H-4, 153
4H-2, 2	7H-2, 1	11H-2, 0	12H-1, 135	15H-5, 2
4H-2, 149	7H-2, 148	11H-2, 20	12H-1, 138	15H-5, 154
4H-3, 1	7H-3, 1	11H-2, 155	12H-1, 140	15H-6, 0
4H-3, 151	7H-3, 91	11H-3, 2	12H-1, 143	15H-6, 95
4H-4, 2	7H-3, 101	11H-3, 154	12H-1, 145	16H-1, 0
4H-4, 149	7H-3, 149	11H-4, 2	12H-1, 148	16H-1, 3
4H-5, 2	7H-4, 1	11H-4, 152	12H-2, 0	16H-1, 5
4H-5, 152	7H-4, 16	11H-5, 2	12H-2, 155	16H-1, 8
4H-6, 2	7H-4, 149	11H-5, 154	12H-3, 2	16H-1, 10
4H-6, 145	7H-5, 0	11H-6, 0	12H-3, 157	16H-1, 13
4H-7, 2	7H-5, 150	11H-6, 155	12H-4, 2	16H-1, 15
4H-7, 87	7H-6, 2	11H-7, 1	12H-4, 157	16H-1, 18
5H-1, 0	7H-6, 7	11H-7, 58	12H-5, 2	16H-1, 20
5H-1, 150	7H-6, 127	12H-1, 0	12H-5, 154	16H-1, 23
5H-2, 2	7H-7, 1	12H-1, 3	12H-6, 0	16H-1, 25
5H-2, 147	7H-7, 53	12H-1, 5	12H-6, 120	16H-1, 28

Only a portion of this table appears here. The complete table is available in **ASCII.**